SANDIA REPORT

SAND2015-0206
Unlimited Release
Printed September, 2014

Toward Multi-scale Modeling and Simulation of Conduction in Heterogeneous Materials

Jeremy B. Lechman, Corbett C. Battaile, Dan S. Bolintineanu, Marcia A. Cooper, William W. Erikson, Stephen M. Foiles, Jeffrey Kay, Leslie M. Phinney, Edward S. Piekos, Paul E. Specht, Ryan R. Wixom, Cole D. Yarrington

Prepared by
Sandia National Laboratories
Albuquerque, New Mexico 87185 and Livermore, California 94550

Sandia National Laboratories is a multi-program laboratory managed and operated by Sandia Corporation, a wholly owned subsidiary of Lockheed Martin Corporation, for the U.S. Department of Energy's National Nuclear Security Administration under contract DE-AC04-94AL85000.

Sandia National Laboratories

Issued by Sandia National Laboratories, operated for the United States Department of Energy by Sandia Corporation.

Available to DOE and DOE contractors from
U.S. Department of Energy
Office of Scientific and Technical Information
P.O. Box 62
Oak Ridge, TN 37831

Telephone: (865) 576-8401
Facsimile: (865) 576-5728
E-Mail: reports@adonis.osti.gov
Online ordering: http://www.osti.gov/bridge

Available to the public from
U.S. Department of Commerce
National Technical Information Service
5285 Port Royal Rd
Springfield, VA 22161

Telephone: (800) 553-6847
Facsimile: (703) 605-6900
E-Mail: orders@ntis.fedworld.gov
Online ordering: http://www.ntis.gov/help/ordermethods.asp?loc=7-4-0#online

SAND2015-0206
Unlimited Release
Printed September, 2014

Toward Multi-scale Modeling and Simulation of Conduction in Heterogeneous Materials

Jeremy B. Lechman, Corbett C. Battaile, Dan S. Bolintineanu, Marcia A. Cooper, William W. Erikson, Stephen M. Foiles, Jeffrey Kay, Leslie M. Phinney, Edward S. Piekos, Paul E. Specht, Ryan R. Wixom, Cole D. Yarrington

Sandia National Laboratories
P.O. Box 5800
Albuquerque, New Mexico 87185-MS0836

Abstract

This report summarizes a project in which the authors sought to develop and deploy: (i) experimental techniques to elucidate the complex, multiscale nature of thermal transport in particle-based materials; and (ii) modeling approaches to address current challenges in predicting performace variability of materials (e.g., identifying and characterizing physical-chemical processes and their couplings across multiple length and time scales, modeling information transfer between scales, and statically and dynamically resolving material structure and its evolution during manufacturing and device performance). Experimentally, several capabilities were sucessfully advanced. As discussed in Chapter 2 a flash diffusivity capability for measuring homogeneous thermal conductivity of pyrotechnic powders (and beyond) was advanced; leading to enhanced characterization of pyrotechnic materials and properties impacting component development. Chapter 4 describes sucess for the first time, although preliminary, in resolving thermal fields at speeds and spatial scales relevant to energetic components. Chapter 7 summarizes the first ever (as far as the authors know) application of TDTR to actual pyrotechnic materials. This is the first attempt to actually characterize these materials at the interfacial scale. On the modeling side, new capabilities in image processing of experimental microstructures and direct numerical simulation on complicated

structures were advanced (see Chapters 3 and 5). In addition, modeling work described in Chapter 8 led to improved prediction of interface thermal conductance from first principles calculations. Toward the second point, for a model system of packed particles, significant headway was made in implementing numerical algorithms and collecting data to justify the approach in terms of highlighting the phenomena at play and pointing the way forward in developing and informing the kind of modeling approach oringinally envisioned (see Chapter 6). In both cases much more remains to be accomplished.

Acknowledgment

The authors acknowledge the support of Jeffrey Kay, Alec Tappan, Robert Knepper, and Michael Marquez for their efforts in preparing the aluminum coated ammonium perchlorate samples and Colin Landon, Thomas Beechem, Justin Serrano, and Patrick Hopkins for assistance with and discussion about the TDTR experiments. We also thank Leonardo Silbert for suppying the jammed particle packs used in that part of this work and for insightful discussions. Finally, a big thanks to Rekha Rao and Frank van Swol for reviewing the manuscript.

Contents

1 Introduction **19**

2 Measuring Bulk, Homogenized Thermal Conductivity of Pressed Pellets via Flash Diffusivity **23**

Thermal Diffusivity Calculations 24

Parker Model 24

Uncertainty Analysis 26

Cowan Model 29

Uncertainty Analysis 33

Specific Heat Calculations 33

Uncertainty Analysis 34

Material Properties 34

Experimental Arrangement 35

Experimental Results 35

Thermal Diffusivity 35

Effect of Density on Thermal Diffusivity 36

Effect of Temperature on Thermal Diffusivity 36

Specific Heat 41

Effect of Density on Specific Heat 41

Effect of Temperature on Specific Heat 41

Comparison to a Specific Heat Found with Mass Averaging 43

Comparison to the Proteus® Software 44

3 Exploring Property Variation via Numerical Simulations on Synthetic Microstructures 53

Diffusion in Fractal "Particles" 53

Fractal Percolation Clusters: Transient Response. 55

2-D Square Lattice of Boxes with Bridges. 56

Conduction in Materials with Random Materials Structure 59

2-D Array of Disks with Randomly Oriented Non-Isotropic Thermal Conductivity. 59

3-D Random Grain Structure in Cube. 60

Creating Computer Models of Sub-Particle Microstructures 61

4 Probing the Inhomogeniety of the Thermal Field in Pressed Pellets via Infrared Camera 75

Experimental Setup 75

Additive manufacturing samples 77

Modeling of AM Samples 78

Homogeneous samples 80

Powder samples 81

Summary 82

5 Computational Thermal Analysis of Pressed Pellets Based on FIB-SEM Data 85

Introduction 85

Methods 86

Image segmentation 87

Generating a finite element mesh from segmented voxel data 89

Thermal analysis 90

Results 91

Conclusions 95

6 Computational Thermal Analysis in Numerically Simulated Particle Packs 99

Random Walk in Jammed Particle Packs 99

Methods 101

Results 104

Random, jammed particle packs 104

Mean first passage times 104

Comparison to simple cubic lattice 108

Summary 108

Further Model Development 109

7 Time Domain Thermoreflectance (TDTR) Thermal Conductivity and Interface Conductance Measurements 117

8 Thermal Boundary Conductance Modeling 127

DFT Calculations 127

Aluminum 128

Silicon 128

Titanium 130

Potassium perchlorate 130

Ammonium perchlorate 131

Diffuse Mismatch Model Calculations 133

Aluminum - Silicon 135

Aluminum - Potassium Perchlorate 137

Titanium - Potassium Perchlorate 139

9 Summary and Conclusions 141

References 143

Appendix

A **151**

B **159**

List of Figures

1.1 Heat flux through a pack of bi-disperse particles. 21

2.1 Raw data from a Ventron TKP-IP pellet. 26

2.2 Double exponential fit to the Ventron TKP-IP pellet raw data. 27

2.3 Parker model fit to the Ventron TKP-IP pellet raw data using 10 terms. 28

2.4 Variation of the thermal diffusivity as a changes for various r values [19]. 30

2.5 Plot of the natural logarithm of the normalized voltage. 31

2.6 Cowan model fit to the raw data for a shot on a Ventron TKP-IP pellet using 10 terms. 32

2.7 Thermal diffusivity as a function of density for the Ventron TKP-IP. 37

2.8 Fraction of TKP-IP transformed as a function of temperature 39

2.9 Thermal diffusivity as a function of temperature for Ventron TKP-IP. 40

2.10 Specific heat as a function of density for the Ventron TKP-IP. 42

2.11 Specific heat as a function of temperature for Ventron TKP-IP. 43

3.1 Models of Koch Cubes. (a) Type 1 surface fractal dimension = $log(13)/log(3)$ = 2.3347. Surface area increases by 13/9 times at each level. Volume increases at each level, asymptotically approaching value of $10/7xV_0$, where V_0 is original cube volume. (b) Type 2 surface fractal dimension = $log(32)/log(4)$ = 2.5. Surface area increases by factor of two at each level. Volume remains constant at each level. 54

3.2 Evolving temperature history in Koch Cube models (a thru e: Type 1 (level 4); f thru j: Type 2 (level 3)). Images from left to right are at times of $5x10^{-5}$, $5x10^{-4}$, $5x10^{-3}$, $5x10^{-2}$, and $5x10^{-1}$ sec, respectively. 62

3.3 Extent of reaction vs. time for various 3-D and fractal objects. 63

3.4 Connected and Isolated cluster finite element meshes. (a, b) Connected Mesh; (c, d) Isolated Mesh 64

3.5 Initial condition applied to surface of red faces in Figure 3.4. Distance is in terms of element thickness. 65

3.6 Temporal response of heated regions in the two meshes of Figure 3.4. The two numbers in the labels of each line are coordinate locations on the heated faces (i.e., the first one is 5 units over and 20 units up on the original 30x30 cube face). (a) connected mesh thermal response; (b) isolated mesh thermal response 65

3.7 2-D square lattice of boxes with bridges. Red is matrix (aluminum properties), blue is void space (air properties). (a) Overall Box Array; (b) Close-up of lower left corner with FE mesh. 66

3.8 Temperature histories (lines) for several different layers in randomized box array (layer 1 is nearest to the heated boundary). Red dots represent the analytic solution for aluminum properties. Green dots represent the analytic solution for a homogenized mixture of aluminum and air. 67

3.9 Deviation of temperature profiles from uniform temperature at various locations in random checker board system as function of time. The temperature at the center of each box in each layer is represented as a separate line. 68

3.10 Deviation of temperature field: (a thru f) from uniform temperature at different time planes; (g thru l) from thermal field given by effective conductivity. 69

3.11 Finite element mesh and grain orientation of 2-D disk array. (a) Finite Element Mesh of Disk Array; (b) Grain Orientation. 70

3.12 Steady-state temperature profile in Disk Array. (a) Temperature; (b) Temperature with Grain Orientation. 71

3.13 Heat flux pathways through disk array. In the left graph, X marks Disk 34. In the right graph, arrow indicates grain orientation of Disk 34. (a) Heat Flux Paths; (b) Detail of Disk 34. 72

3.14 Cube consisting of 162 grains each of which has a randomized orientation. (a) Mesh (162 Grains); (b) Mesh and Grain Orientation Vectors; (c) Grain Orientation Vectors 73

3.15 Finite element mesh and grain orientation of model polycrystal. (a) Steady State Temperature Profile; (b) Heat Flux Pathways. 73

3.16 74

4.1 Illustration of the ignitor and pellet alignment fixture for observation of thermal transport. 76

4.2 Photograph of IR camera for observation of ignitor and pellets arrangement. 77

4.3 Scale measurement of FOV for 4x microscope lens. 78

4.4 Photograph of aligned pellets and alignment process to accommodate narrow depth of field. 79

4.5 Spatial temperature histories at line-out within region of interest showing sample heating in time. 79

4.6 Spatial temperature histories at line-out within region of interest showing sample heating in time. 80

4.7 (a) mesh of checkerboard AM article atop heater plate. (b) temperature profiles at a simulated time of 10 min. 81

4.8 Details of temperature profile highlighting the region between the first and second row of holes. Left: at t=5 sec; Right: at t=30 sec. 82

4.9 Temperature snapshots between the first and second row of windows taken at 1 sec intervals from t=5 sec to t=30 sec. 83

4.10 Camera FOV and region of interest for data analysis showing ribbon heater location between top and bottom pressed pellet slab. 83

4.11 Spatial temperature histories at line-out within region of interest showing sample heating in time. 84

4.12 Camera FOV and region of interest for data analysis showing ribbon heater location between top and bottom pressed pellet slab. 84

5.1 The image segmentation process. The original image (a) is treated with a bilateral filter (b), followed by a two-value thresholding operation to isolate the $KClO_4$ (dark grey) phase (c). Small features are removed by erosion and dilation operations (d), and the process is repeated for the Ti (light grey) phase (e). The final image (f) shows the three segmented phases, where black, grey and white correspond to void space, Ti and $KClO_4$, respectively. See text for additional details. 88

5.2 Thermal conductivity (a) and temperature field (b) in the finite element model. 92

5.3 Sensitivity of computed effective conductivity to mesh size 92

5.4 Computed and experimental effective conductivity as a function of %TMD. See text for additional details. Panel (b) is simply an enlarged portion of the low k_{eff} region in panel (a). 94

5.5 Variations in other properties as a function of ϕ_{Ti}, the assumed volume fraction of Ti in the Ti-rich phase. Panel (a) shows the overall weight fractions of Ti and $KClO_4$ in the mixture, while panel (b) shows the effective conductivity of the Ti-rich phase according to equation 5.0.4 96

6.1 Jammed particle packs at low and high pressures. Particles are colored by their volume-averaged mean first passage time ($\bar{t}$). See text for more details . 102

6.2 Diffusion characteristics of random walkers in jammed particle packs. Inset in panel (a) shows plots of the exponent α, where MSD = $Dt^{\alpha(t)}/6$. 105

6.3 Characteristic times at which Fickian diffusion is recovered (a) and late-time value of the diffusion coefficient (b) as a function of pressure in jammed particle packs. 105

6.4 Mean first passage times. (a) Comparison of volume-averaged MFPTs computed from simulations and from the analytical expression of Cheviakov et al [14]. The main figure shows the comparison of the histograms, the inset shows the direct comparison of values for all particles, with a solid line corresponding to a slope of unity and zero intercept. (b) Relationship between t^*_{95}/t_m and MFPT for all pressures. Inset shows corresponding MSD* at $t = t^*_{95}$; see text for details. 107

6.5 Key scaling behaviors in simple cubic lattice particle arrangements as compared to jammed systems. 109

6.6 non-Fickian parameter $\beta(t)$ (MSD $\sim t^{\beta(t)}$) for various pressures. 111

6.7 Jump distributions for walkers in jammed particle pack prepared at $p = 0.0004$. (a) Early-time jump distributions where effect of sphere boundaries can be seen. Solid lines show Gaussian spread of walkers in homogeneous, isotropic materials with diffusion coefficient D_0, random walkers in particle pack spread relatively slower; (b) early-intermediate time showing development of "shoulder" in jump distribution; (c) late-intermediate time showing Gaussian inner region (dashed lined) and development of exponential tail (dotted line) in jump distributions; (d) Late-time jump distributions showing return to nearly Gaussian distribution of walkers (dashed line). 112

6.8 Non-Gaussian parameter for packs at various pressures: (a) normalized excess kurtosis; (b) maximum normalized excess kurtosis as a function of pressure. . 113

6.9 Jump distribution for $p = 0.00004$. 114

6.10 Compare data with model. This uses all four parameters following Chaudhuri et al. $l_1 = d$, $l_2 = r$, $\tau_1 =$, and $\tau_2 =$ 115

6.11 Compare model with model. (a) version 1 of model – all four parameters; (b) version 2 of the model – three parameters/Montoll-Wiess CTRW with Gaussian initial condition. 116

7.1 Schematic for the time domain thermoreflectance (TDTR) experiment. 118

7.2 Picture of the TDTR experiment in Building 897/Room 2424. 118

7.3 Microscope images of sample A: (a) prior to and (b) after aluminum coating deposition. 120

7.4 Microscope images of sample B: (a) prior to and (b) after aluminum coating deposition. 121

7.5 Ratio of the in-phase to out-of-phase TDTR signal for four scans on sample A showing the initial increase due to the pump pulse heating and subsequent decay. 122

7.6 Decrease in the ratio of the in-phase to the out-of-phase signal for TDTR for sample A from 500 ps to 4000 ps and the model fit for a thermal conductivity of 0.485 $\pm$ 0.024 W/mK and thermal conductance of 52 $\pm$ 17 mW/m^{2}K 123

8.1 Predicted phonon density of states for aluminum. 129

8.2 Predicted phonon density of states for silicon. 129

8.3 Predicted phonon density of states for titanium. 130

8.4 Predicted phonon density of states for potassium perchlorate. 131

8.5 Predicted partial phonon density of states for potassium perchlorate. 132

8.6 Comparison of computed and measured acoustic phonon dispersion for aluminum and silicon in the (100) direction. 135

8.7 Dispersion relations in the (100) direction for silicon and aluminum, with the transmission coefficient for an Al-Si interface between them. 136

8.8 Comparison of thermal boundary conductance computed in the current work to previous DMM computations and measured values. 137

8.9 Dispersion relations for aluminum and potassium perchlorate with the transmission coefficient for an Al-$KClO_4$ interface between them. The potassium perchlorate dispersion relation is truncated; It actually extends to nearly 32 THz. 138

8.10 Computed thermal boundary conductance for aluminum on potassium perchlorate. 138

8.11 Computed thermal boundary conductance for titanium on potassium perchlorate. 139

8.12 Computed thermal boundary conductance for titanium on potassium perchlorate. 140

List of Tables

2.1 Parameters of the TKP Pellets. 45

2.2 Change in the Thermal Diffusivity with the Number of Terms Used in the Cowan Model. 46

2.3 Average Thermal Diffusivity in mm^2/s for Each TKP and THKP Formulation. 46

2.4 Average Thermal Diffusivity in mm^2/s for the Ventron TKP-IP at Temperature. 47

2.5 Average Measured Specific Heat in J/gK of Each TKP and THKP Formulation Using the Pocographite Reference. 48

2.6 Average Measured Specific Heat in J/gK of Each TKP and THKP Formulation Using the Pyroceram® Reference. 49

2.7 Average Measured Specific Heat in J/gK of Ventron TKP-IP at Temperature Using the Pocographite Reference. 50

2.8 Average Measured Specific Heat in J/gK of Ventron TKP-IP at Temperature Using the Pyroceram® Reference. 50

2.9 Analytically Determined Specific Heat in J/gK of Each TKP and THKP Formulation Using Mass Averaging. 51

7.1 Table 1: Experimental Conditions for the sample A and sample B TDTR measurements 125

7.2 Table 2: AP Thermal Conductivity and Al/AP Thermal Boundary Conductance 126

8.1 Comparison of internal relaxation parameters for potassium perchlorate computed via DFT with previous measurements. 132

Chapter 1

Introduction

The complex response of disordered, inhomogeneous and heterogeneous materials to mechanical and thermodynamic loads results from microscopic dynamical/stochastic processes occurring over multiple length and time scales. As a first step toward increased complexity of material response, consider the difference between an homogeneous material and a disordered, inhomogeneous material. Inhomogeneity of the material structure can be viewed as a variability of local material properties. However, the randomness or disorder of the structure complicates the effect of the inhomogeneity; leading to variation of local properties across scales. This can be seen in random, inhomogeneous materials where at large lengths a Central Limit-like or ensemble averaging property leads to a single, effective bulk, homogenized material property different from the constituent homogeneous material [6, 89, 76]. On intermediate length scales properties can vary significantly between these two limits [67]. Property variation across scales due to structural disorder, in turn, can lead to significant variability in the performance of a device or component. Current challenges in predicting performace variability of materials include: (i) identifying and characterizing physical and/or chemical processes, and their couplings across multiple length and time scales; (ii) modeling information transfer between scales; (iii) statically and dynamically resolving material structure and its evolution during manufacturing and device performance. Overcoming these challenges to create engineered solutions requires multi-scale materials theory/modeling and experimental discovery and characterization.

Not surprisingly, actual materials of interest to Sandia are often far from ideal and homogeneous. Material inhomogeneity and heterogeneity arise due to the presence of defects, impurities, grain boundaries and interfaces, poly-crystallinity, multiple constituent materials and phases along with associated microstructure, etc. These present themselves on a hierarchy of scales. Hence, the resulting variability of properties and related dynamical transport processes across length and time scales creates significant challenges to predictive modeling and experimental characterization for applications such as material failure (ductile or brittle) and initiation and ignition of energetic materials and beyond.

In this project, we sought to develop and deploy: (i) experimental techniques to elucidate the complex, multiscale nature of thermal transport in particle-based materials; and (ii) modeling approaches to address the aforementioned challenges. This report summarizes the work involved in these efforts. Specifically, we began to explore energy transport in particle-based composite heterogeneous materials with a view toward multi-physics coupling

to mass transport and chemistry (i.e., hot-wire pyrotechnic applications). Key to predicting the performance of pyrotechnic devices is accurately determining the heat pulse to and its distribution in the powder, particularly near the bridgewire-powder interface. Our goal was to build on past sucesses validating homogenized, asymptotic models [24] by accounting for heat flow which departs from classical models based on the heat equation (i.e., Fouriers Law) due to inhomogeneity in the heat transport arising from particle-scale microstructure (see Figure 4.1). Evidence for this "anomalous diffusion can be found in experimental results [25]. Additionally, it was anecdotally known that particle size, size distribution and particle morphology matter in determining the bulk properties of the powders of interest, we aimed at quantifying this variability (see Chapters 2) and understanding the sub-particle material structure, particle morphology, and compostite microstructure connections as they relate to thermal transport in pressed powder pellets (see Chapters 3 and 5).

One key advance sought and challenge addressed was connecting the temporal response with the microstructural inhomogeneity and building nonlocal models which capture the effect of inhomogeneity consistent with the chosen scale resolution, Δt and Δx. While much remains to be done here, some progress was made toward this end in Chapter 6.

The experimental component of the proposed work had two main thrusts: (i) microstructure characterization; and (ii) transport measurements probing scale-dependent behavior. Particularly challenging is, in-stitu, real-time, simultaneous experimental resolution of microstructure and the relevant transport fields on a broad range of scales. For multiple scale systems, this requires not just the normal matching the field-of-view to resoution (or, sample period to sample frequency) ratio of the experimental measurement technique with the scale of the sytem/processes of interest, but also requires techniques with large field-of-view to resolution ratios or mulitple measurement techniques with overlapping resolutions to cover the range of relevant scales. We pursued development of experimental capabilities for discovering the range of compositions and preparations of pressed pyrotechnic powder pellets for which anomalous diffusion may be detectable – i.e., we wanted to find experimental techniques that matched the relevant length and time scales. Once this is achieved, then thermal transport in particle systems spanning the detectable range can be measured to provide validation data. These experiments were to highlight anomalous transport mechanisms in pyrotechnic powders and provide the groundwork for the incorporating microstructural effects into the scale-consistent models (see Chapter 4).

Moving beyond the question of anomalous thermal diffusion at the particle-microstructural scale we desired to investigate and extend models to capture material dependent thermal transport at the sub-grain scale where interfaces (contact resistances), grain boundaries, dislocation, impurities, and other crystal defects are relevant. There was a significant element of experimental discovery at this level (see Chapter 7). Particular focus was given to the role of interfaces (e.g., bridgewire-powder, oxidizer-metal) and atomistic models of contact resistance (see Chapter 8).

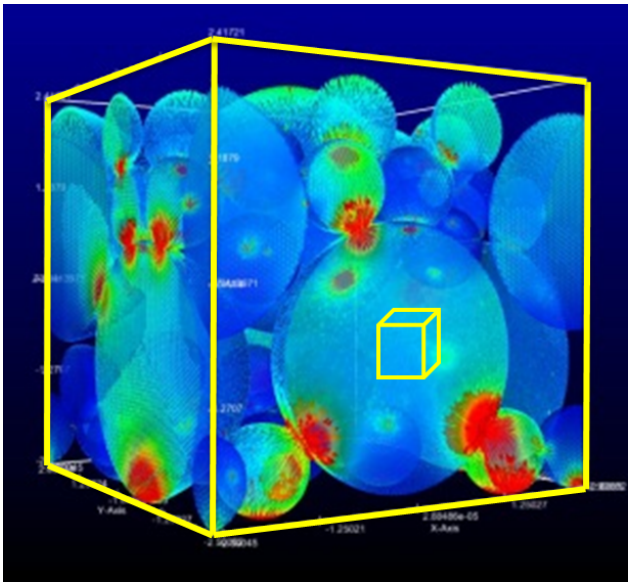

Figure 1.1. Heat flux through a pack of bi-disperse particles.

Chapter 2

Measuring Bulk, Homogenized Thermal Conductivity of Pressed Pellets via Flash Diffusivity

As a first step toward a "top-down" characterization of the variability of particulate-based energetic materials, this chapter details a fast, accurate method for assessing their macroscale thermal properties. A previous method for this purpose used much more material for each sample tested and was more difficult to perform; although it gave more detailed information on the internal thermal state of the sample [24]. The newly established capability is useful for quantifying the thermal conductivity and associated uncertainty in pressed powder pellets at the bulk or macro-scale. In particular it was found that there are significant differences (18%) in the thermal diffusivity of two similar powders. The main difference between the powders being the particle size distributions and noticeably different particle morphologies of one of the components (Ti) in the mix used to press the pellets. These differences can be attributed to the origins of the feedstock; differing manufacturing processes and environmental histories led to the aforementioned variability.

Specifically, the flash technique is used to measure the thermal diffusivity and specific heat of titanium potassium perchlorate (TKP) input powder (33wt% Ti - 67wt% KP) with Ventron supplied titanium particles, TKP input powder (33wt% Ti - 67wt% KP) with ATK supplied titanium particles, TKP output powder (41wt% Ti - 59wt% KP), and titanium subhydride potassium perchlorate (THKP) (33wt% $TiH_{1.65}$ - 67wt% KP) at at 25°C. The influence of density and temperature on the thermal diffusivity and specific heat of TKP with Ventron supplied titanium particles is investigated.

The flash method can be used to determine the thermal diffusivity and specific heat of a material following ASTM Standard E1461-13 [1]. The method involves exposing one side of a sample to a high intensity, short duration pulse of light. The temperature rise on the opposite side of the sample is measured with a thermocouple or infrared detector. The measured back surface response is used to determine the thermal diffusivity and, through comparisons to a known reference, the specific heat. A commercial Netzsch NanoFlash® LFA 447 machine was approved for thermal diffusivity and specific heat measurements on energetic materials in the Explosives Components Facility. The NanoFlash® machine comes with software for the execution of the experiment and analysis of the data. The numerics of the Proteus®

LFA analysis program [65] are not available for scrutiny. To provide more confidence in the measured results and corresponding uncertainties, a MATLAB® [57] program for analyzing the raw voltage data was developed.

The MATLAB® analysis program works on the assumption that the recorded back surface voltage is directly proportional to the temperature. Additionally, each individual flash, or shot, is assumed to be essentially identical given the same NanoFlash® machine parameters. The analysis code loads in the NanoFlash® data files and calculates the thermal diffusivity using either the Parker [69] or Cowan [18, 19] model. Data for a reference material can then be loaded for the determination of the material's specific heat. Below is a description of the thermal diffusivity and specific heat calculations along with the associated error approximations.

The thermal diffusivities and specific heats of the following materials are presented.

- Titanium potassium perchlorate (TKP)
  - TKP input powder (33wt% Ti - 67wt% KP) with Ventron titanium particles (Ventron TKP-IP)
    - At densities ranging from 2.0 to 2.3 g/cm^3 at 25 °C
    - At a density of 2.1 g/cm^3 and temperatures ranging from 25 to 250 °C
  - TKP input powder (33wt% Ti - 67wt% KP) with ATK titanium particles (ATK TKP-IP) at a density of 2.1 g/cm^3 at 25°C
  - TKP output powder (41wt% Ti - 59wt% KP) (TKP-OP) at a density of 2.5 g/cm^3 at 25°C
- Titanium subhydride potassium perchlorate (33wt% $TiH_{1.65}$ - 67wt% KP) (THKP) at a density of 2.3 g/cm^3 at 25 °C

The specific heats are reported using both pocographite and Pyroceram® as the reference material. Determining the specific heat with the flash technique is prone to errors. Its accuracy relies on identical experimental parameters (*i.e.* temperature, flash voltage, flash duration, filter, masks, and coatings) and thermal properties between the sample and reference.

Thermal Diffusivity Calculations

Parker Model

A simple adiabatic model for determining a material's thermal diffusivity was proposed by Parker *et al.* [69]. The Parker model assumes that the normalized voltage, V, can be

represented by the following equations.

$$V = 1 + 2\sum_{n=1}^{\infty}(-1)^n \exp(-n^2\omega) \tag{2.0.1}$$

$$\omega = \frac{\pi^2 \alpha t}{L} \tag{2.0.2}$$

Here, α is the thermal diffusivity, t is time, and L is the sample thickness. At the half rise time, $V_{0.5}$, $T = 0.5$ and ω is equal to 1.38785. The thermal diffusivity directly follows.

$$\alpha = \frac{1.38785 L^2}{\pi^2 t_{0.5}} \tag{2.0.3}$$

The MATLAB® code implements the Parker model by first determining the zero time of the voltage record. The NanoFlash® machine has an inherent delay between the start of voltage recording and the flash of the Xenon lamp. This delay is related to the parameters of the experiment and is extracted from the NanoFlash® data file. The voltage record before the zero time is fit to a linear polynomial in time. This linear fit is applied to the entire voltage record to compensate for possible sensor drift during the measurement. After this correction, the voltage record is normalized. Like all raw data, the recorded signal has inherent noise. This is is seen in the raw data obtained from a Ventron TKP-IP pressed pellet shown in Figure 2.1. To estimate the maximum voltage, the MATLAB® code smooths the raw data and locates the beginning of the voltage rise. The initiation of the rise was chosen as 5% of the maximum value for easy identification in signals with high noise. To avoid anomalies caused by bleed through of the flash, the first 1 ms after the zero time is excluded when locating the voltage rise. Flash bleed through can be an issue for porous samples.

After locating the rise point, the raw data after the rise point is fit to a double exponential equation. This fitting was done in MATLAB® with the default algorithm for the *fit* command [56], which is the Levenberg-Marquardt method [51, 55]. This is the algorithm used to determine the coefficients and associated error for all curve fitting in this program.

$$T = C_1 \exp(C_2 t) + C_3 \exp(C_4 t) \tag{2.0.4}$$

The double exponential function was chosen since it provides an excellent fit to the raw data as seen in Figure 2.2. The time and amplitude of the maximum value of this curve fit is then determined.

$$t_{max} = \frac{1}{C_4 - C_2} \ln\left(\frac{-C_1 C_2}{C_3 C_4}\right) \tag{2.0.5}$$

$$T_{max} = C_1 \exp(C_2 t_{max}) + C_3 \exp(C_4 t_{max}) \tag{2.0.6}$$

The raw data is normalized by T_{max} and fit to Equation 2.0.1 with the number of terms in the series specified by the user. From the value of ω obtained, α is calculated from Equation 2.0.3.

An example of the Parker model fit to the Ventron TKP-IP pellet using 10 terms is shown in Figure 2.3. The Parker model poorly matches the peak and late time voltages, due to the adiabatic nature of the model. Without incorporating heat losses, the late time voltages are bound to a single value and cannot decrease like the measured response.

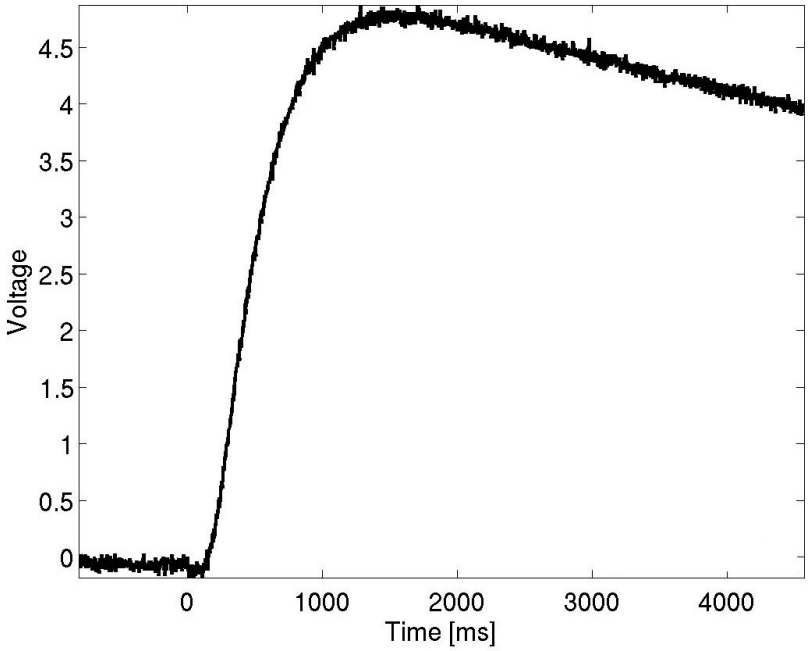

Figure 2.1. Raw data from a Ventron TKP-IP pellet.

Uncertainty Analysis

Since the raw data was normalized with an analytical fit, there is an inherent uncertainty in each of the coefficients. This uncertainty will propagate through the calculation effecting the certainty to which α is known. This error is determined through the use of the standard error equation for $Y = f(x_i)$ [5].

$$\delta Y = \sqrt{\sum_i \left(\frac{\partial Y}{\partial x_i} \delta x_i \right)^2} \tag{2.0.7}$$

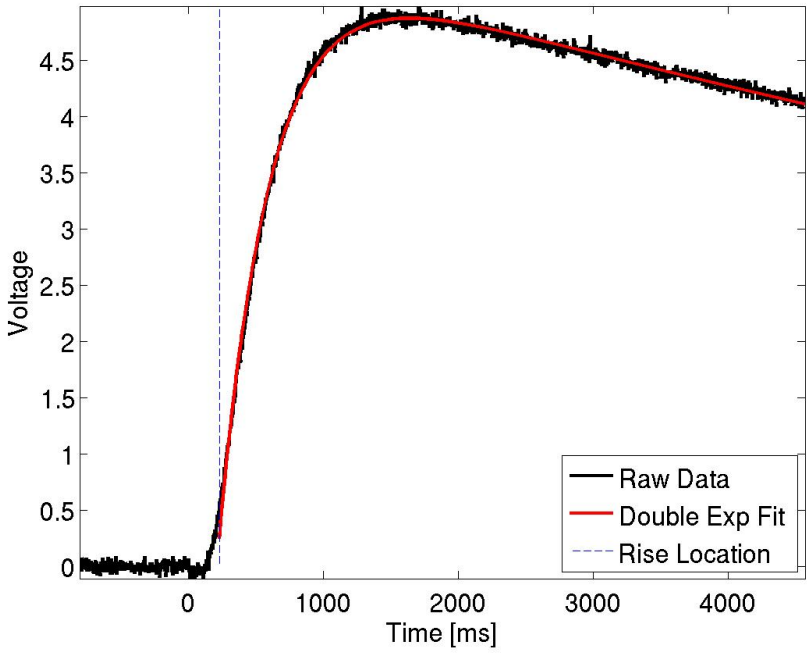

Figure 2.2. Double exponential fit to the Ventron TKP-IP pellet raw data.

Using the double exponential fit for the raw voltage (Equation 2.0.4), the following partial derivatives are determined for T_{max}.

$$\frac{\partial T_{max}}{\partial C_1} = \exp(C_2 t_{max}) \tag{2.0.8}$$

$$\frac{\partial T_{max}}{\partial C_2} = C_1 t_{max} \exp(C_2 t_{max}) \tag{2.0.9}$$

$$\frac{\partial T_{max}}{\partial C_3} = \exp(C_4 t_{max}) \tag{2.0.10}$$

$$\frac{\partial T_{max}}{\partial C_4} = C_3 t_{max} \exp(C_4 t_{max}) \tag{2.0.11}$$

$$\frac{\partial T_{max}}{\partial t_{max}} = C_1 C_2 \exp(C_2 t_{max}) + C_3 C_4 \exp(C_4 t_{max}) \tag{2.0.12}$$

$$\tag{2.0.13}$$

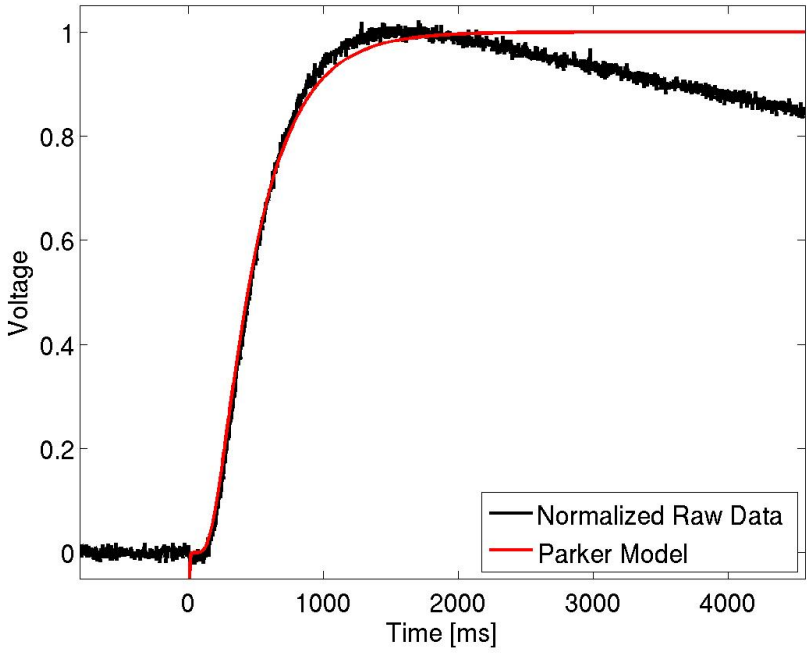

Figure 2.3. Parker model fit to the Ventron TKP-IP pellet raw data using 10 terms.

The uncertainties in C_1 through C_4 (*i.e.* δC_i) are obtained from the MATLAB® fit. The uncertainty in t_{max} is found using the partial derivatives of Equation 2.0.5.

$$\frac{\partial t_{max}}{\partial C_1} = \frac{1}{C_1(C_4 - C_2)} \tag{2.0.14}$$

$$\frac{\partial t_{max}}{\partial C_2} = \frac{1}{C_2(C_4 - C_2)} + \frac{1}{(C_4 - C_2)^2} \ln\left(\frac{-C_1 C_2}{C_3 C_4}\right) \tag{2.0.15}$$

$$\frac{\partial t_{max}}{\partial C_3} = \frac{-1}{C_3(C_4 - C_2)} \tag{2.0.16}$$

$$\frac{\partial t_{max}}{\partial C_4} = \frac{-1}{C_4(C_4 - C_2)} - \frac{1}{(C_4 - C_2)^2} \ln\left(\frac{-C_1 C_2}{C_3 C_4}\right) \tag{2.0.17}$$

$$\tag{2.0.18}$$

Using these partial derivatives and the uncertainties in each quantity, δT_{max} is calculated using Equation 2.0.7. The error in the normalized voltage, δV, as a percentage is the following.

$$\frac{\delta V}{V} = \frac{\delta T_{max}}{T_{max}} \tag{2.0.19}$$

The fit of the Parker model to the normalized voltage leads to an uncertainty in ω. Using the uncertainty in V and ω, a 3×3 matrix is developed of potential half rise times, $\delta t_{0.5}$. This

consists of every iteration using the upper, lower, and median values of ω and V. Half the difference between the maximum and minimum half rise time in the matrix is used to define the associated uncertainty, since it is a more conservative error estimation than the standard deviation. The uncertainty in α, $\delta\alpha$, is found using the partial derivatives of Equation 2.0.3 and the error associated with each quantity.

$$\frac{\partial \alpha}{\partial t_{0.5}} = \frac{-1.38785 L^2}{\pi^2 t_{0.5}^2} \tag{2.0.20}$$

$$\frac{\partial \alpha}{\partial L} = \frac{2.7757 L}{\pi^2 t_{0.5}} \tag{2.0.21}$$

$$\tag{2.0.22}$$

In these calculations, the uncertainties represent the standard deviation. The 95% confidence interval is obtained by multiplying the standard deviation by 1.96.

Cowan Model

The model proposed by Cowan [18, 19] to determine the thermal diffusivity with the flash technique accounts for radiation and convective losses at the sample surfaces. These loses lead to the decrease in voltage seen in the raw data of Figure 2.1 at later times. This correction makes the Cowan model more appropriate for determining the thermal diffusivity of most samples.

If the front of a sample is exposed to a high-intensity, short duration pulse of energy, the temperature response, $\Theta(0,t)$, at the back of the sample can be described with the following relation.

$$\frac{L c_p \rho \Theta(0,t)}{Q} = 2 \sum_{n=0}^{\infty} \frac{y_n^2}{D_n \exp\left(\frac{\alpha y_n^2 t}{L^2}\right)} \tag{2.0.23}$$

Here, L is the sample thickness, c_p is the specific heat, ρ is the density, Q is the total energy per unit area, and α is the thermal diffusivity. The terms y_n are the solution of the following equation over the interval $n\pi < y < (n+1)\pi$.

$$\cot y = \frac{y}{a} - \frac{b}{ay} \tag{2.0.24}$$

In this equation, the terms a and b relate to the energy lost at the irradiated, c_0, and back surfaces, c_L.

$$a = L(c_0 + c_L) = L c_0 (1 + r) \tag{2.0.25}$$

$$b = \frac{r a^2}{(1+r)^2} \tag{2.0.26}$$

$$r = \frac{c_L}{c_0} \tag{2.0.27}$$

The term D_n is then defined as the following.

$$D_n = y_n \sin(y_n)\left(1 + a - \frac{2b}{a} + \frac{y_n^2}{a} + \frac{b}{y_n^2} + \frac{b^2}{a y_n^2}\right) \tag{2.0.28}$$

This set of equations can be solved to a high degree of accuracy with a rough knowledge of r by taking two ratios of the temperature response at different times [19]. This results from the thermal diffusivity being relatively insensitive to r for a values below 5 as seen in Figure 2.4. Typically, the following ratios are chosen.

$$R_5 = \frac{\Theta(0, 5t_{0.5})}{\Theta(0, t_{0.5})} \tag{2.0.29}$$

$$R_{10} = \frac{\Theta(0, 10t_{0.5})}{\Theta(0, t_{0.5})} \tag{2.0.30}$$

$$\tag{2.0.31}$$

Since samples in the flash method usually have similar graphite coatings and masks on the irradiated and back surfaces, r is assumed to be unity. Variations in r (*i.e.* from 0 to 100) were found to alter the calculated thermal diffusivity in a Ventron TKP-IP pellet by less than 0.2%. Errors corresponding to uncertainties in the value of r are assumed to be included in the conservative error estimations described in Section 2.

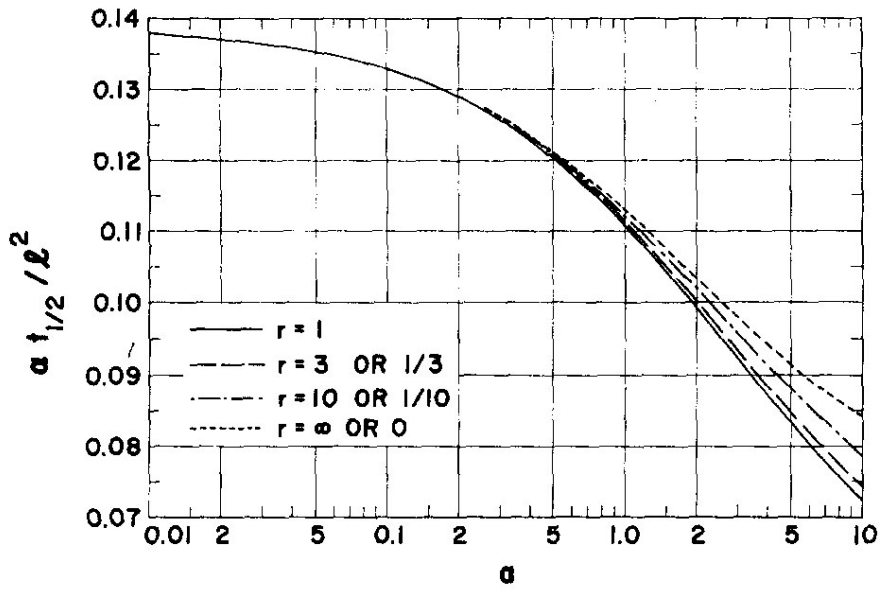

Figure 2.4. Variation of the thermal diffusivity as a changes for various r values [19]. For a values up to 5, the thermal diffusivity is relatively insensitive to changes in r.

Calculating the thermal diffusivity using the Cowan model begins with fitting the raw data to a double exponential function (Equation 2.0.4) and normalizing the curve by the

maximum voltage identical to that done for the Parker model (Section 2). This double exponential fit is used to find V at 1, 5, and 10 half times. The value determined at 1 half time is used to get a rough estimate of the thermal diffusivity using the Parker model (Equation 2.0.3). This rough approximation of α is used as an initial guess to expedite fitting the Cowan model to the data.

Cowan suggests that an adequate approximation of a can be determined by assuming the energy is deposited as a step function [18]. This effectively leads to analyzing the drop in normalized voltage due to heat loss. Taking the natural logarithm of the normalized voltage, V, for all time after the peak, a curve is generated that asymptotically approaches a straight line. This curve is shown in Figure 2.5. The second half of this curve is fit to a linear equation, $F(0,t)$. The value of this linear fit at t_{max} provides an estimation of a.

$$F(0,t_{max}) \cong 1 + \frac{a}{6} \tag{2.0.32}$$

This result is only valid if the first term in Equation 2.0.23 at t_{max}, $V_0(0,t_{max})$, differs from unity by around 0.08 [18] and is a very crude first approximation.

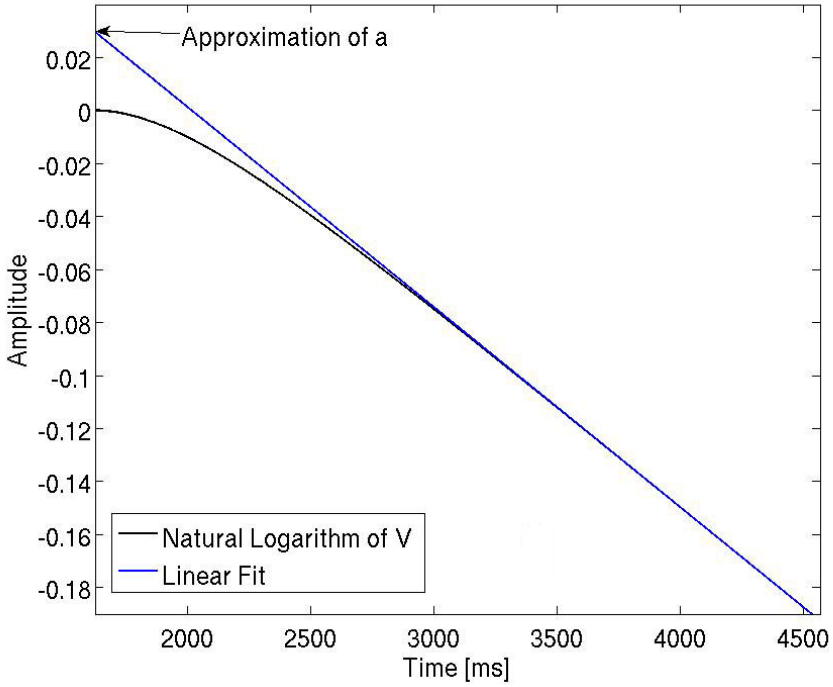

Figure 2.5. Plot of the natural logarithm of the normalized voltage, V. The second half of $ln(V)$ is fit to a linear polynomial, the value of which at t_{max} provides a rough approximation of a.

With this approximation of a, the values of y_n and D_n are found. Equation 2.0.23 is

then used to find the thermal diffusivity, α that matches the temperature ratios at R_5 and R_{10}. The α given by both ratios should match. However, given the crude nature in which a was approximated, this is not the case. The MATLAB® code iterates to obtain an α that satisfies both ratios. Figure 2.4 shows that, as a increases, α decreases. A refined α value is then defined as the average of the values obtained from R_5 and R_{10} and it is compared to the previous approximation. If the new value of α is lower than the previous one, a is increased. If the new value is higher, a is decreased. This new a value is then used to recalculate α. The process repeats until α converges to a desired tolerance. The MATLAB® code changes the a value by 1% for each iteration. There is no strong reason for this magnitude of change other than it seemed to give a convergence of α to within a tolerance of 0.1% in around 50 iterations. If the values doesn't converge to the desired tolerance after 60 iterations, the code resets to the initial approximation of a and iterates until the best agreement possible is reached. This is typically within 5% and is necessary for high-noise signals. A Cowan model fit with 10 terms to the Ventron TKP-IP pellet is shown in Figure 2.6. The Cowan model is seen to fit the raw data very well, providing a much better estimation of the thermal diffusivity than the Parker model.

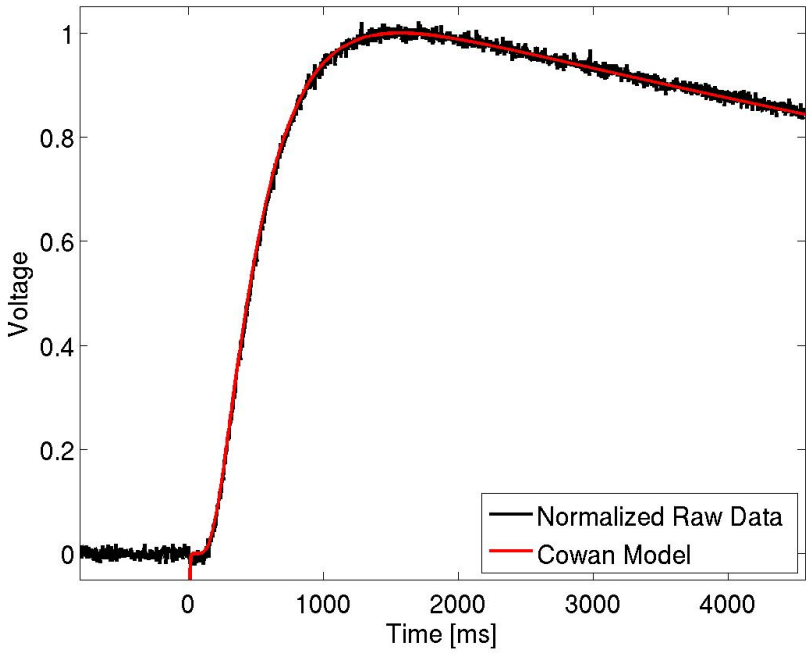

Figure 2.6. Cowan model fit to the raw data for a shot on a Ventron TKP-IP pellet using 10 terms. The Cowan model is seen to fit the experimental data much better than the Parker model due to its incorporation of heat losses.

Uncertainty Analysis

Since the raw data was normalized in the same method as the Parker model, the error in V_{max} is accounted for in the same way as in Section 2. This same procedure is extended to find the errors in V, at 1, 5 and 10 half times, which provide the errors in R_5 and R_{10}. Equation 2.0.23 also relies on the pellet thickness, which also has a measured error. Using the errors in R_5, R_{10}, and L, a 6×3 matrix is developed. The first 3×3 section corresponds to α calculated using $R_5 \pm \delta R_5$ and $L \pm \delta L$, while the second corresponds to that using $R_{10} \pm \delta R_{10}$ and $L \pm \delta L$ (*i.e.* all iterations of the maximum, minimum, and median values of each parameter). Once again, the error recorded in α is half the difference between the maximum and minimum values obtained in this 6×3 matrix.

Specific Heat Calculations

The specific heat of a sample can be determined with the flash method through comparison to a known reference sample. The heat applied to a sample can be expressed with the following.

$$Q = mc_p\Delta T \tag{2.0.33}$$

If the reference and sample undergo the same flash exposure and have the same absorption coefficient, the heat imparted to them can be set equal. The specific heat of the sample can then be related to the specific heat of the reference.

$$c_{p_{sample}} = \frac{m_{ref}}{m_{sample}} \frac{\Delta T_{ref}}{\Delta T_{sample}} c_{p_{ref}} \tag{2.0.34}$$

If the sample and reference have the same flash parameters (*i.e.* temperature, flash voltage, flash duration, filter, masks, and coatings), Equation 2.0.34 can be rewritten as the following.

$$c_{p_{sample}} = \frac{T_{adb_{ref}}}{T_{adb_{sample}}} \frac{A_{sample}}{A_{ref}} \frac{\rho_{ref}}{\rho_{sample}} \frac{L_{ref}}{L_{sample}} c_{p_{ref}} \tag{2.0.35}$$

Here, T_{adb} is the adiabatic temperature rise, which corresponds to the maximum temperature of the reference and sample assuming no heat losses. To ensure a proper comparison, this ratio is multiplied by the ratio of the electronic gain factors used in the measurement of each, A_{sample} and A_{ref}. If identical masks are used, the area of the sample and reference are the same and the mass term reduces to ρL.

To use Equation 2.0.35, the adiabatic temperature rise must be determined. This is done in the MATLAB® routine using both the Cowan and Parker models. For both the sample and the reference, the half rise time, $t_{0.5}$, and thermal diffusivity, α, are calculated using the Cowan model, since it accounts for heat loses. These half rise times are used to calculate the normalized voltage, $V_{C_{t_{0.5}}}$, from the double exponential fit. This normalized voltage, $V_{C_{t_{0.5}}}$, will be below the 0.5 expected under adiabatic conditions. The ratio of 0.5 to $V_{C_{t_{0.5}}}$ provides

an estimate of the fraction of heat dissipated in the first half of the rise. The fraction of heat lost in the first half of the rise is assumed to be identical to that lost in the second half of the rise. The recorded voltage at the half rise time is multiplied by this ratio and doubled to provide an estimate of the expected maximum voltage rise given adiabatic conditions, T_{adb}. From this approximation, c_p is calculated from Equation 2.0.35.

Uncertainty Analysis

The error associated with the adiabatic temperature rise follows from the error method used for finding the maximum voltage and half rise time outlined previously in Section 2. Errors in t_{max} is found with the Cowan model, as described in Section 2. The error in $V_{C_{t_{0.5}}}$ found with the exponential fit follows that for V_{max} outlined in Section 2. The error of c_p for the sample is then a simple application of the standard error equation for all variables in Equation 2.0.35.

It should be noted that specific heats found with the flash method are prone to errors and should be used with caution. Errors in the specific heat of the reference will inherently cause errors in the specific heat of the sample. Identical experimental parameters (*i.e.* temperature, flash voltage, flash duration, filter, masks, and coatings) and similar thermal properties between the sample and reference are also necessary. Care must be taken when using such data.

Material Properties

Various formulations of titanium and potassium perchlorate (KP) with differing hydride levels were measured using the flash technique.

- Titanium potassium perchlorate input powder (33wt% Ti - 67wt% KP) with Ventron Ti particles (Ventron TKP-IP)
- Titanium potassium perchlorate (33wt% Ti - 67wt% KP) with ATK Ti particles (ATK TKP-IP)
- Titanium potassium perchlorate output powder (41wt% Ti - 59wt% KP) (TKP-OP)
- Titanium subhydride potassium perchlorate (33wt% $TiH_{1.65} - 67wt\%$ KP) (THKP).

The various TKP and THKP formulations were pressed into pellets. The properties of which are given in Table 2.1. The uncertainty in the sample weights are taken as the uncertainty of the scale used. The uncertainty of the height are obtained from 4 independent measurements at different locations on the sample. The sample was made with a high precision die, so negligible error is assumed for the diameter. The uncertainty in the density was obtained

from the standard error equation (Equation 2.0.7). All uncertainties listed in this report represent the 95% confidence interval.

There are several points to make from Table 2.1. The Ventron TKP-IP was pressed into pellets with roughly 68, 71, 76, and 79% theoretical maximum density (TMD) in order to study the change in thermal properties of TKP with pellet density. The Ventron TKP-IP was chosen for this study since it was easier to handle once pressed than the ATK TKP-IP. The density range represents the highest TMD capable of the press and the lowest TMD thought to provide robust enough samples to measure. Two distinct pellet heights of the ATK TKP-IP were also pressed. This was done to ensure that all measurements were representative of the bulk material. The ATK TKP-IP was brittle once pressed. As a result, only a single 1 mm tall ATK TKP-IP pellet survived for testing.

Experimental Arrangement

The thermal diffusivity of each TKP and THKP pellet was measured at least 5 times at 25 °C. In addition, Ventron TKP-IP pellets IP-V-1-71-1 and IP-V-1-71-2 were measured at 50, 100, 150, 200, and 250 °C to understand the change in thermal diffusivity and specific heat with temperature. Measurements were stopped at 250 °C for two reasons: the crystallographic phase transition in KP at around 300 °C [41], and complications with adherence of the graphite coating at higher temperatures. The NanoFlash® machine allows for a 0.5 °C deviation from the specified temperature with a 0.1 °C accuracy of the reading. This is the source of the temperature error reported in the experimental results. The samples were coated with graphite ($\sim$ 5 microns) to ensure uniform and thorough absorption of the Xenon flash energy. The flash was run with 270 V for the 1 mm tall pellets and 292 V for the 3 mm tall pellets. The higher voltage for the 3 mm tall pellets was done to improve the signal-to-noise ratio. Every shot had no filter (NanoFlash® filter option 5). The temperature rise on the back side of each pellet was measured with a InSb IR sensor cooled with liquid nitrogen. In all tests, the flash duration ($\sim$ 250 μs - NanoFlash® pulse option "Medium" for the 1 mm tall pellets and $\sim$ 450 μs - NanoFlash® pulse option "Long" for the 3 mm tall pellets) is significantly less than the half rise time ($\sim$ 300 ms for 1 mm tall pellets and $\sim$ 5000 ms for 3 mm tall pellets), so no correction for the pulse duration is needed [2]. The NanoFlash® machine parameters are all listed in Table A.1.

Experimental Results

Thermal Diffusivity

All shots on the TKP and THKP pellets were analyzed using the Cowan model [18, 19], since it accounts for radiative and conductive heat losses. The Cowan model can be

implemented with any number of terms. Table 2.2 shows the computed thermal diffusivity for Ventron TKP-IP pellet IP-V-1-71-1 as the number of terms varies. Convergence occurs with only 3 terms. However, for the results presented here, 10 terms were used to ensure convergence in all cases.

The thermal diffusivity and accompanying error for each shot on the TKP and THKP pellets are presented in Table A.2. The average thermal diffusivity and accompanying error for each pellet at 25 °C along with the average thermal diffusivity for each TKP and THKP formulation (*i.e* the average of all pellets) are listed in Table 2.3. For most TKP and THKP formulations, the sample-to-sample variation is small ($< 5\%$). With such repeatability in the thermal diffusivity it is assumed that 1 mm is representative of the bulk material response. The exception is TKP-OP. Pellet OP-1-80-1 has a significantly lower thermal diffusivity than pellets OP-1-80-2 or OP-1-80-3. While the exact reason for this unknown, it could be tied to the lower density of pellet OP-1-80-1. Further studies on the change in thermal diffusivity with density need to be performed on TKP-OP to verify this hypothesis.

A comparison of the TKP-IP pellets at around 71% TMD shows a large difference between the Ventron and ATK formulations ($\sim 18\%$). This difference may be tied to the different particle morphologies of the Ti or unique powder compressibility causing alternate density gradients. Dependence of thermal diffusivity on thicknesses is also observed in ATK TKP-IP. The 1 mm tall ATK pellet has a $\sim$14% higher thermal diffusivity than the 3 mm tall pellets. The suggestion that the 1 mm pellet is not representative of the bulk material response is an unlikely explanation of this difference. A change in the density gradient of the pellet due to the increased thickness may be the more likely. Further studies are necessary to find the exact cause.

Effect of Density on Thermal Diffusivity

Table 2.3 shows an upward trend in thermal diffusivity with density in the Ventron TKP-IP at 25 °C. This trend is fit to a quadratic equation using the data from all four samples, and is shown in Figure 2.7. The data suggests that the thermal diffusivity remains relatively constant at lower densities before increasing dramatically. This trend could be tied to a critical connectivity between Ti particle, which could be investigated with stereological methods. Since the 2.0 g/cm^2 pellets proved to be sturdy, pellets at even lower densities could be pressed to further investigate the lower density regime.

Effect of Temperature on Thermal Diffusivity

Since the Ventron TKP-IP was measured at various temperatures, it is important to consider the effect of thermal expansion. With the coefficient of thermal expansion, CTE, the thickness and density of a material as a function of temperature can be described with the following.

$$t(T) = t_o(1 + (T - 25))CTE \tag{2.0.36}$$

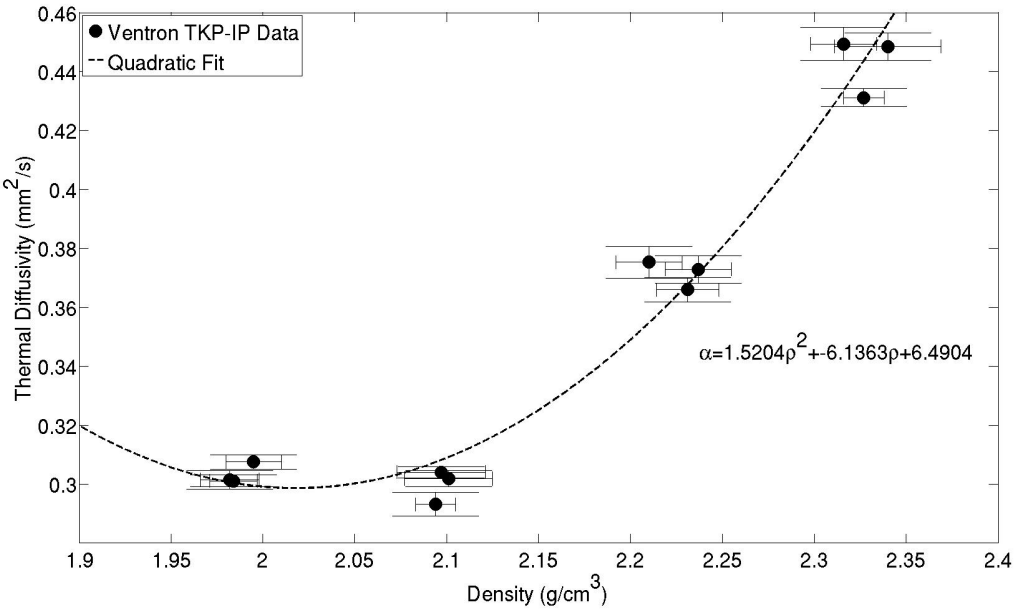

Figure 2.7. Thermal diffusivity as a function of density for the Ventron TKP-IP at 25 °C. The data shows an upward trend in thermal diffusivity with increasing density, which is fit to a quadratic equation.

$$\rho(T) = \frac{m}{V_o(1 + 3(T - 25)CTE)} \tag{2.0.37}$$

Here, t_o is the initial thickness, V_o is the initial volume, and T is the temperature measured in Celsius. Taking the CTE to be as high as $15 \times 10^{-6}\ C^{-1}$ leads to a negligible change (*i.e.* $< 0.7\%$) in the measured thermal diffusivity and specific heat of the Ventron TKP at 250 250 °C. For this reason, the effects of thermal expansion are considered to be included in the conservative error estimations reported.

The flash method relies on exposing one side of the sample to a high intensity short duration pulse of light. KP undergoes a crystallographic phase transition at roughly 300 °C [41]. It is important to consider the amount of KP that has transformed during the measurement to ensure the results are representative of nascent TKP. The amount of KP transformed can be estimated by modeling the sample's temperature distribution assuming all the laser energy is immediately and uniformly absorbed into a thin layer of the material [69].

$$T(x,t) = \frac{Q}{\rho c_p L}\left[1 + 2\sum_{n=1}^{\infty}\cos\left(\frac{n\pi x}{L}\right)\frac{\sin\left(\frac{n\pi g}{L}\right)}{\left(\frac{n\pi g}{L}\right)}\exp\left(\frac{-n^2\pi^2}{L^2}\alpha t\right)\right] + T_o \tag{2.0.38}$$

Here, Q is the radiant energy of the laser pulse in J/cm^2, ρ is the sample density in g/cm^3, c_p is the sample specific heat in J/gK, L is the sample thickness in cm, g is the absorption layer thickness in cm, α is the samples thermal diffusivity in cm^2/s, and T_o is the initial temperature of the sample.

As a rough approximation, all the energy is assumed to instantly and uniformly be absorbed into a 5 micron graphite layer. Ideally, a two phase model should be used, since the above equation assumes a homogeneous material. However, this simplification will suffice as a rough estimate. The NanoFlash® machine is reported to have a maximum energy deposition of 3 J/cm^2 [64]. Since the Ventron TKP was run with a 270 V flash and a duration of ~ 250 μs, the radiant laser energy is assumed to be just 2 J/cm^2. The sample density, thickness, and thermal diffusivity are all taken from the measured values. A mass average value is taken for the specific heat, which is discussed in Section 2. Using these values and 10 terms in the summation, the fraction of the sample having transformed KP at each temperature measured can be calculated and is plotted in Figure 2.8. It can be seen that even up to 290 °C less than 10% of the TKP-IP has transformed. These results are the same order of magnitude as previous estimates using a radiant heat flux boundary condition [16]. Based on both of these approximations, it is assumed that the amount of KP transformed in the measurements can be neglected and that the results are representative of nascent TKP.

The average thermal diffusivity for Ventron TKP-IP at each temperature measured is listed in Table 2.4. For both IP-V-1-71-1 and IP-V-1-71-2, the thermal diffusivities show a similar downward trend in thermal diffusivity with temperature. This trend is fit to a quadratic equation using the data from both samples, and is shown in Figure 2.9.

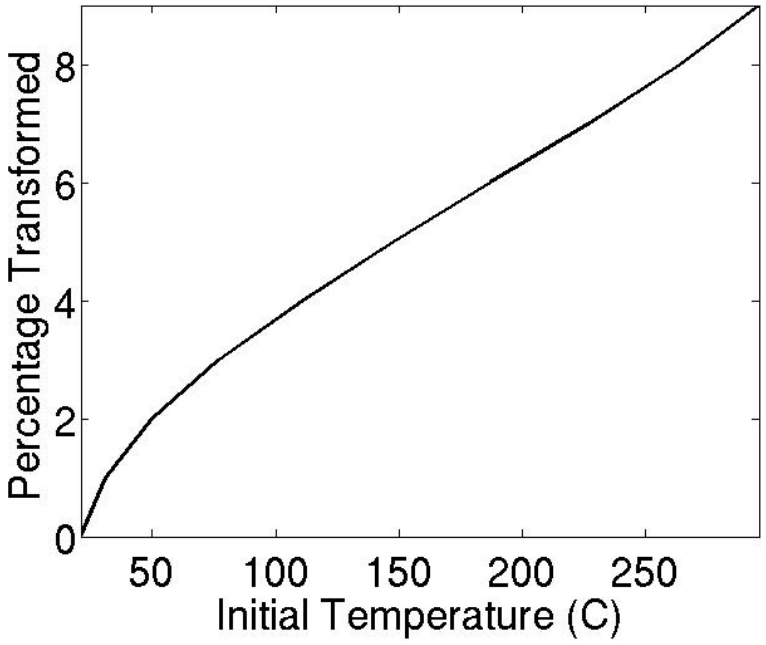

Figure 2.8. Fraction of TKP-IP transformed as a function of temperature. The results show that up to 290 ^{o}C less than 10% of the TKP-IP has transformed

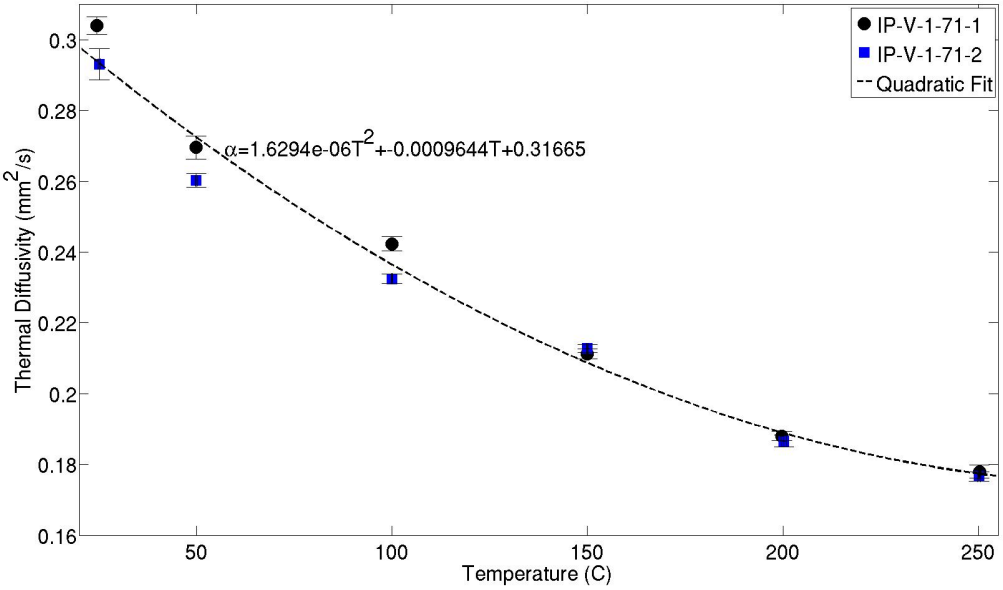

Figure 2.9. Thermal diffusivity as a function of temperature for both Ventron TKP-IP samples. The data shows a downward trend in thermal diffusivity with increasing temperature, which is fit to a quadratic equation.

Specific Heat

The specific heat of a sample can be found with the flash technique through comparisons to a reference material. The accuracy of this method relies on identical experimental parameters (*i.e.* temperature, flash voltage, flash duration, filter, masks, and coatings) and thermal properties between the sample and reference. ASTM Standard E1461-13 [1] also requires a short time lapse between the sample and reference measurements. Specific heats found using reference measurements with delays ranging from minutes to weeks of the sample gave essentially identical results (*i.e* the errors overlapped). This supports the reported repeatability in NanoFlash® Xenon flash[64]. As a result, no effort was made to have short delays between reference and sample measurement, with some being as much as weeks apart.

The NanoFlash® machine at Sandia has two reference materials: pocographite and Pyroceram®. While the TKP and THKP formulations have identical machine parameters to the reference materials, they do not have similar thermal properties. Care should be taken when using the specific heats reported here.

The specific heats measured for each shot on the TKP and THKP pellets using pocographite are given in Table A.3, while those using Pyroceram® are given in Table A.4. The average response at 25 °C for each TKP and THKP formulation using pocographite are listed in Table 2.5, while those found using Pyroceram® are in Table 2.6. To calculate the specific heat, each pellet was compared to the average of 5 shots on the reference materials at identical machine parameters and temperatures. There is an observed variability in specific heat with reference material. Specific heats found with pocographite have $\sim 15\%$ higher value when compared to those found with Pyroceram®. This result is related to the differing thermal properties of pocographite and Pyroceram®. This variability highlights the importance of similar parameters between the sample and reference. The differing thermal and physical properties between the reference and sample make measuring the specific heat of a sample to a high degree of accuracy difficult. These considerations must be kept in mind when using this data.

Effect of Density on Specific Heat

The change is specific heat as a function density at 25 °C for the Ventron TKP-IP pellets is presented graphically Figure 2.10. The data shows a shallow downward trend in specific heat with density that is fit to a linear equation. Since the specific heats found with pocographite are a consistent percentage off from those found with Pyroceram®, both exhibit shallow slopes.

Effect of Temperature on Specific Heat

The average specific heat of the Ventron TKP-IP at each temperature measured using the pocographite reference are listed in Table 2.7, while those found using Pyroceram® are in

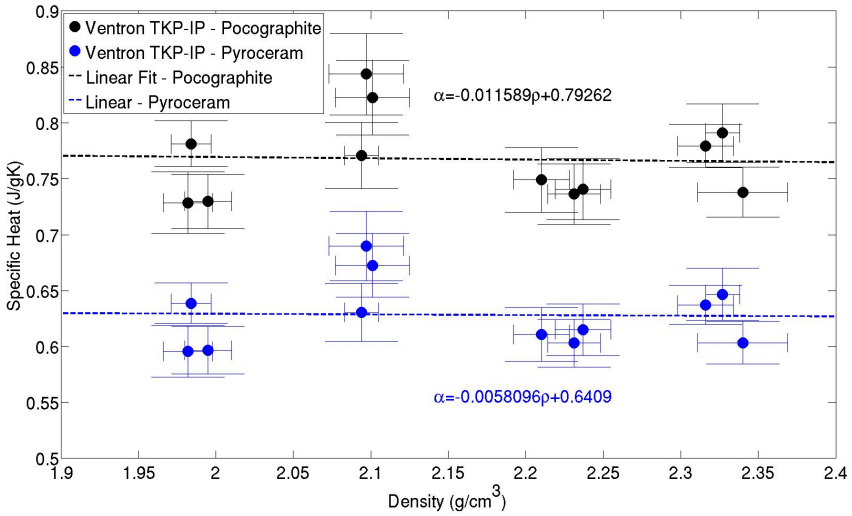

Figure 2.10. Specific heat as a function of density for the Ventron TKP-IP at 25 °C. The data shows a shallow downward trend in specific heat as density increases. The results also show a dependence on the reference material. The specific heat found with pocographite (black) is $\sim 15\%$ higher than that found with Pyroceram® (blue).

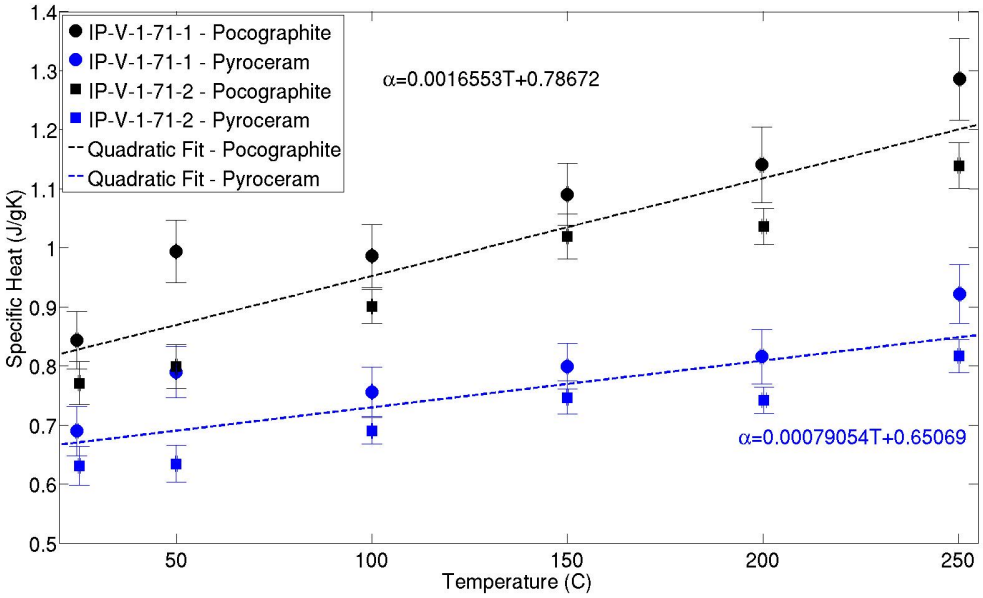

Figure 2.11. Specific Heat as a function of temperature for both Ventron TKP-IP samples. The data shows an upward trend in specific heat with increasing temperature, which is fit to a linear equation. The specific heat found with pocographite (black) is consistently higher than that found with Pyroceram® (blue).

Table 2.8. Once again, each pellet was compared to the average of 5 shots on the reference materials at identical machine parameters and temperatures. There is still the observed variability in specific heat with reference material. The change is specific heat as a function temperature for the Ventron TKP-IP pellets is presented graphically Figure 2.11. The data shows an upward trend in specific heat with temperature that is fit to a linear equation. Since the specific heats found with pocographite are a consistent percentage off from those found with Pyroceram®, similar slopes are seen in both linear fits.

Comparison to a Specific Heat Found with Mass Averaging

The specific heat measured at 25 °C with the flash technique can be compared to an analytical value determined through mass averaging of the constituents. The specific heat of each component can be found using JANAF tables [41]. Assuming a 0.5 °C temperature error in the tabular data, the specific heat of Potassium Perchlorate, Titanium, and Titanium Hydride at 25 °C are $c_{p_{KP}} = 0.7954 \pm 0.0054$ J/gK, $c_{p_{Ti}} = 0.5271 \pm 0.0002$ J/gK, and $c_{p_{TiH}} = 0.6030 \pm 0.0009$ J/gK, respectively. Using the compositions of each TKP and THKP formulation listed in Section 2, an analytical specific heat using mass averaging can be

determined. These values are given in Table 2.9. The values in Table 2.9 tend to lie between those calculated with the pocographite and Pyroceram® standards. The exception to this is TKP-OP, which is below this analytical value for both standards.

Comparison to the Proteus® Software

In order to verify the MATLAB® routine, it was desired to compare it to the Proteus® LFA analysis software [65] provided with the NanoFlash® machine. The thermal diffusivities found at 25 °C using the Cowan model with both the Proteus® software and MATLAB® code are presented in Table A.5. The two methods are within 5% for all cases and within 3% for most pellets. As a result, the MATLAB® code is considered to be an appropriate analysis method for determining thermal diffusivity.

The specific heats found with the Proteus® software and the MATLAB® code using the pocographite reference are presented in Table A.6, while those found using the Pyroceram® reference are presented in Table A.7. The two methods are within 5% for all 1 mm pellets with most being within 2% . The error in the 3 mm pellets is much larger due to the degree of signal conditioning that was required. The MATLAB® and Proteus® packages must have different methods for signal conditioning. Despite this difference, the results have overlapping errors and can be considered essentially the same values. As a result, the MATLAB® code is considered to be an appropriate analysis method for determining specific heat.

Table 2.1. Parameters of the TKP Pellets.

Pellet Label	Energetic Material	TMD (%)	Diameter (mm)	Weight (g)	Height (mm)	Density (g/cm^2)
IP-V-1-68-1	TKP-IP (Ventron)	68.0	12.725	0.257 ± 0.0005	1.013 ± 0.007	1.995 ± 0.015
IP-V-1-68-2	TKP-IP (Ventron)	67.6	12.725	0.252 ± 0.0005	0.999 ± 0.005	1.984 ± 0.013
IP-V-1-68-3	TKP-IP (Ventron)	67.5	12.725	0.252 ± 0.0005	1.000 ± 0.007	1.982 ± 0.016
IP-V-1-71-1	TKP-IP (Ventron)	71.4	12.725	0.272 ± 0.0005	1.020 ± 0.011	2.097 ± 0.024
IP-V-1-71-2	TKP-IP (Ventron)	71.3	12.725	0.271 ± 0.0005	1.018 ± 0.004	2.094 ± 0.011
IP-V-1-71-3	TKP-IP (Ventron)	71.4	12.725	0.269 ± 0.0005	1.007 ± 0.011	2.101 ± 0.024
IP-V-1-76-1	TKP-IP (Ventron)	75.3	12.725	0.290 ± 0.0005	1.032 ± 0.008	2.210 ± 0.018
IP-V-1-76-2	TKP-IP (Ventron)	76.2	12.725	0.293 ± 0.0005	1.030 ± 0.007	2.237 ± 0.018
IP-V-1-76-3	TKP-IP (Ventron)	76.0	12.725	0.293 ± 0.0005	1.033 ± 0.007	2.231 ± 0.017
IP-V-1-79-1	TKP-IP (Ventron)	79.3	12.725	0.349 ± 0.0005	1.179 ± 0.004	2.327 ± 0.011
IP-V-1-79-2	TKP-IP (Ventron)	78.9	12.725	0.341 ± 0.0005	1.158 ± 0.008	2.316 ± 0.018
IP-V-1-79-3	TKP-IP (Ventron)	79.7	12.725	0.344 ± 0.0005	1.156 ± 0.014	2.340 ± 0.029
IP-A-1-71-1	TKP-IP (ATK)	70.6	12.725	0.265 ± 0.0005	1.000 ± 0.009	2.084 ± 0.019
IP-A-3-71-1	TKP-IP (ATK)	71.0	12.725	0.852 ± 0.0005	3.195 ± 0.017	2.097 ± 0.011
IP-A-3-71-2	TKP-IP (ATK)	70.4	12.725	0.849 ± 0.0005	3.211 ± 0.006	2.079 ± 0.005
IP-A-3-71-3	TKP-IP (ATK)	71.1	12.725	0.852 ± 0.0005	3.190 ± 0.005	2.100 ± 0.004
OP-1-80-1	TKP-OP	79.5	12.725	0.322 ± 0.0005	1.034 ± 0.007	2.449 ± 0.019
OP-1-80-2	TKP-OP	81.0	12.725	0.326 ± 0.0005	1.028 ± 0.008	2.494 ± 0.021
OP-1-80-3	TKP-OP	80.6	12.725	0.325 ± 0.0005	1.030 ± 0.013	2.482 ± 0.033
THKP-1-80-1	THKP	80.8	12.725	0.303 ± 0.0005	1.038 ± 0.005	2.295 ± 0.013
THKP-1-80-2	THKP	80.0	12.725	0.303 ± 0.0005	1.047 ± 0.011	2.275 ± 0.025
THKP-1-80-3	THKP	80.4	12.725	0.306 ± 0.0005	1.053 ± 0.003	2.285 ± 0.010

Table 2.2. Change in the Thermal Diffusivity with the Number of Terms Used in the Cowan Model.

Number of Terms	2	3	4	5	10
α (mm^2/s)	0.3108	0.3050	0.3050	0.3050	0.3050

Table 2.3. Average Thermal Diffusivity in mm^2/s for Each TKP and THKP Formulation.

Pellet Label	Temperature (C)	Average Thermal Diffusivity	Formulation Thermal Diffusivity
IP-V-1-68-1	24.58 ± 0.26	0.3076 ± 0.0024	
IP-V-1-68-2	25.16 ± 0.43	0.3011 ± 0.0020	0.3034 ± 0.0056
IP-V-1-68-3	25.18 ± 0.36	0.3015 ± 0.0031	
IP-V-1-71-1	24.56 ± 0.28	0.3041 ± 0.0024	
IP-V-1-71-2	25.18 ± 0.36	0.2932 ± 0.0040	0.2997 ± 0.0082
IP-V-1-71-3	25.20 ± 0.64	0.3019 ± 0.0027	
IP-V-1-76-1	25.38 ± 0.19	0.3753 ± 0.0054	
IP-V-1-76-2	24.82 ± 0.88	0.3729 ± 0.0047	0.3714 ± 0.0082
IP-V-1-76-3	24.82 ± 0.69	0.3660 ± 0.0042	
IP-V-1-79-1	25.04 ± 0.57	0.4312 ± 0.0031	
IP-V-1-79-2	24.84 ± 0.80	0.4494 ± 0.0056	0.4430 ± 0.0142
IP-V-1-79-3	25.26 ± 0.28	0.4485 ± 0.0047	
IP-A-1-71-1	24.76 ± 0.35	0.2457 ± 0.0019	0.2457 ± 0.0019
IP-A-3-71-1	24.90 ± 0.30	0.2239 ± 0.0042	
IP-A-3-71-2	25.12 ± 0.36	0.2151 ± 0.0066	0.2155 ± 0.0139
IP-A-3-71-3	25.08 ± 1.30	0.2074 ± 0.0113	
OP-1-80-1	25.08 ± 0.48	0.3050 ± 0.0021	
OP-1-80-2	25.38 ± 0.39	0.3290 ± 0.0045	0.3236 ± 0.0209
OP-1-80-3	25.30 ± 0.41	0.3369 ± 0.0040	
THKP-1-80-1	24.88 ± 0.26	0.2964 ± 0.0040	
THKP-1-80-2	25.12 ± 1.37	0.3048 ± 0.0037	0.3057 ± 0.0131
THKP-1-80-3	25.14 ± 0.40	0.3159 ± 0.0025	

Table 2.4. Average Thermal Diffusivity in mm^2/s for the Ventron TKP-IP at Temperature.

Pellet Label	Temperature (C)	Average Thermal Diffusivity
IP-V-1-71-1	24.56 ± 0.28	0.3041 ± 0.0024
IP-V-1-71-1	49.92 ± 0.18	0.2696 ± 0.0033
IP-V-1-71-1	100.02 ± 0.18	0.2424 ± 0.0020
IP-V-1-71-1	150.02 ± 0.18	0.2112 ± 0.0014
IP-V-1-71-1	199.74 ± 0.42	0.1880 ± 0.0013
IP-V-1-71-1	250.24 ± 0.30	0.1780 ± 0.0018
IP-V-1-71-2	25.18 ± 0.36	0.2932 ± 0.0044
IP-V-1-71-2	49.96 ± 0.21	0.2603 ± 0.0020
IP-V-1-71-2	100.02 ± 0.19	0.2325 ± 0.0013
IP-V-1-71-2	150.02 ± 0.19	0.2128 ± 0.0011
IP-V-1-71-2	200.26 ± 0.51	0.1866 ± 0.0017
IP-V-1-71-2	250.14 ± 0.32	0.1766 ± 0.0013

Table 2.5. Average Measured Specific Heat in J/gK of Each TKP and THKP Formulation Using the Pocographite Reference.

Pellet Label	Temperature (C)	Average Specific Heat	Formulation Specific Heat
IP-V-1-68-1	24.58 ± 0.26	0.7297 ± 0.0243	
IP-V-1-68-2	25.16 ± 0.43	0.7813 ± 0.0205	0.7466 ± 0.0480
IP-V-1-68-3	25.18 ± 0.36	0.7287 ± 0.0276	
IP-V-1-71-1	24.56 ± 0.28	0.8436 ± 0.0364	
IP-V-1-71-2	25.18 ± 0.36	0.7710 ± 0.0297	0.8124 ± 0.0615
IP-V-1-71-3	25.20 ± 0.64	0.8225 ± 0.0334	
IP-V-1-76-1	25.38 ± 0.19	0.7491 ± 0.0290	
IP-V-1-76-2	24.82 ± 0.88	0.7407 ± 0.0271	0.7456 ± 0.0234
IP-V-1-76-3	24.82 ± 0.69	0.7363 ± 0.0269	
IP-V-1-79-1	25.04 ± 0.57	0.7909 ± 0.0262	
IP-V-1-79-2	24.84 ± 0.80	0.7793 ± 0.0194	0.7694 ± 0.0446
IP-V-1-79-3	25.26 ± 0.28	0.7380 ± 0.0223	
IP-A-1-71-1	24.76 ± 0.35	0.7388 ± 0.0302	0.7388 ± 0.02302
IP-A-3-71-1	24.90 ± 0.30	0.8804 ± 0.0787	
IP-A-3-71-2	25.12 ± 0.36	0.9948 ± 0.0883	0.9279 ± 0.1283
IP-A-3-71-3	25.08 ± 1.30	0.9086 ± 0.1390	
OP-1-80-1	25.08 ± 0.48	0.6530 ± 0.0177	
OP-1-80-2	25.38 ± 0.39	0.6445 ± 0.0235	0.6491 ± 0.0181
OP-1-80-3	25.30 ± 0.41	0.6498 ± 0.0268	
THKP-1-80-1	24.88 ± 0.26	0.7120 ± 0.0240	
THKP-1-80-2	25.12 ± 1.37	0.7274 ± 0.0322	0.7356 ± 0.0489
THKP-1-80-3	25.14 ± 0.40	0.7675 ± 0.0289	

Table 2.6. Average Measured Specific Heat in J/gK of Each TKP and THKP Formulation Using the Pyroceram® Reference.

Pellet Label	Temperature (c)	Average Specific Heat	Formulation Specific Heat
IP-V-1-68-1	24.58 ± 0.26	0.5967 ± 0.0211	
IP-V-1-68-2	25.16 ± 0.43	0.6388 ± 0.0183	0.6104 ± 0.0398
IP-V-1-68-3	25.18 ± 0.36	0.5958 ± 0.0229	
IP-V-1-71-1	24.56 ± 0.28	0.6898 ± 0.0310	
IP-V-1-71-2	25.18 ± 0.36	0.6304 ± 0.0259	0.6642 ± 0.0510
IP-V-1-71-3	25.20 ± 0.64	0.6725 ± 0.0285	
IP-V-1-76-1	25.38 ± 0.19	0.6108 ± 0.0239	
IP-V-1-76-2	24.82 ± 0.88	0.6150 ± 0.0232	0.6097 ± 0.0200
IP-V-1-76-3	25.26 ± 0.28	0.6031 ± 0.0216	
IP-V-1-79-1	25.04 ± 0.57	0.6467 ± 0.0232	
IP-V-1-79-2	24.84 ± 0.80	0.6372 ± 0.0174	0.6291 ± 0.0373
IP-V-1-79-3	25.26 ± 0.28	0.6035 ± 0.0191	
IP-A-1-71-1	24.76 ± 0.35	0.6041 ± 0.0258	0.6041 ± 0.0258
IP-A-3-71-1	24.90 ± 0.30	0.7496 ± 0.0676	
IP-A-3-71-2	25.12 ± 0.36	0.8470 ± 0.0758	0.7900 ± 0.1094
IP-A-3-71-3	25.08 ± 1.30	0.7736 ± 0.1185	
OP-1-80-1	25.08 ± 0.48	0.5339 ± 0.0157	
OP-1-80-2	25.38 ± 0.39	0.5270 ± 0.0203	0.5308 ± 0.0154
OP-1-80-3	25.30 ± 0.41	0.5313 ± 0.0227	
THKP-1-80-1	24.88 ± 0.26	0.5821 ± 0.0210	
THKP-1-80-2	25.12 ± 1.37	0.5948 ± 0.0274	0.6015 ± 0.0408
THKP-1-80-3	25.14 ± 0.40	0.6275 ± 0.0253	

Table 2.7. Average Measured Specific Heat in J/gK of Ventron TKP-IP at Temperature Using the Pocographite Reference.

Pellet Label	Temperature (C)	Average Specific Heat
IP-V-1-71-1	24.56 ± 0.28	0.8436 ± 0.0487
IP-V-1-71-1	49.92 ± 0.18	0.9941 ± 0.0530
IP-V-1-71-1	100.02 ± 0.18	0.9863 ± 0.0535
IP-V-1-71-1	150.02 ± 0.18	1.0908 ± 0.0524
IP-V-1-71-1	199.74 ± 0.42	1.1406 ± 0.0639
IP-V-1-71-1	250.24 ± 0.30	1.2858 ± 0.0695
IP-V-1-71-2	25.18 ± 0.36	0.7710 ± 0.0368
IP-V-1-71-2	49.96 ± 0.21	0.7987 ± 0.0370
IP-V-1-71-2	100.02 ± 0.19	0.9007 ± 0.0285
IP-V-1-71-2	150.02 ± 0.19	1.0192 ± 0.0384
IP-V-1-71-2	200.26 ± 0.51	1.0363 ± 0.0307
IP-V-1-71-2	250.14 ± 0.32	1.1394 ± 0.0388

Table 2.8. Average Measured Specific Heat in J/gK of Ventron TKP-IP at Temperature Using the Pyroceram® Reference.

Pellet Label	Temperature (C)	Average Specific Heat
IP-V-1-71-1	24.56 ± 0.28	0.6898 ± 0.0417
IP-V-1-71-1	49.92 ± 0.18	0.7900 ± 0.0433
IP-V-1-71-1	100.02 ± 0.18	0.7561 ± 0.0415
IP-V-1-71-1	150.02 ± 0.18	0.7994 ± 0.0386
IP-V-1-71-1	199.74 ± 0.42	0.8159 ± 0.0459
IP-V-1-71-1	250.24 ± 0.30	0.9219 ± 0.0499
IP-V-1-71-2	25.18 ± 0.36	0.2932 ± 0.0328
IP-V-1-71-2	49.96 ± 0.21	0.6344 ± 0.0309
IP-V-1-71-2	100.02 ± 0.19	0.6902 ± 0.0226
IP-V-1-71-2	150.02 ± 0.19	0.7466 ± 0.0284
IP-V-1-71-2	200.26 ± 0.51	0.7420 ± 0.0223
IP-V-1-71-2	250.14 ± 0.32	0.8170 ± 0.0280

Table 2.9. Analytically Determined Specific Heat in J/gK of Each TKP and THKP Formulation Using Mass Averaging.

Energetic Material	Percentage Ti	Percentage $TiH_{1.65}$	Percentage KP	Specific Heat
TKP-IP (Ventron)	33	0	67	0.7069 ± 0.0036
TKP-IP (ATK)	33	0	67	0.7069 ± 0.0036
TKP-OP	41	0	59	0.6854 ± 0.0032
THKP	0	33	67	0.7319 ± 0.0036

Chapter 3

Exploring Property Variation via Numerical Simulations on Synthetic Microstructures

In the previous chapter it was suggested that differences in the macroscale thermal properties of two pressed powder pellets are most likely attributable to constituent particle morphology and subsequent meso-structure of the pellets. In this chapter, we address the idea that the morphology/structure of an object matters for conduction. Connectivity of regions of high transport, anisotropic constituent material properties and cluster sizes and shapes can lead to interesting (even "anomalous") conduction phenomenology, both at steady state as well as in unsteady conditions. These phenomena are largely known, but are perhaps unappreciated in their relation to transport across particulate materials' meso-structures; i.e., the process of homogenization. We will present a series of finite element simulations which illustrate various phenomena including the that of so-called anomalous diffusion.

Diffusion in Fractal "Particles"

In this section, we briefly examine the effects of fractional (fractal) geometry on diffusion processes. Here we consider two particular fractal geometries: a Koch Cube of Type 1 (dimension 2.3347) and a Koch Cube of Type 2 (dimension 2.5). Models of these two geometries were constructed and meshed. Figure 3.1 shows the meshes and gives some characteristic information.

Simulations were performed in which the Koch Cubes were given an initial internal temperature of zero while on the outer surface a temperature of one was instantaneously imposed and maintained. Temperature profile snapshots at various points in time are shown in Figure 3.2. Note that the characteristic shape of the isotherms becomes smoother and simpler as time goes by. Early in time there is considerable roughness or structure associated with the large surface area due to the small blocks on or near the outer surface. Those fine structures quickly saturate, leaving coarser structures in the interior.

As a representation of the overall extent of energy transfer (or equivalently, the degree of

conversion/extent of reaction in a diffusion-limited process), the volume of material below a certain threshold temperature (here 0.5 was chosen) was monitored continuously. This might represent a diffusion-controlled reaction front or a level of energy transfer in a thermal process.

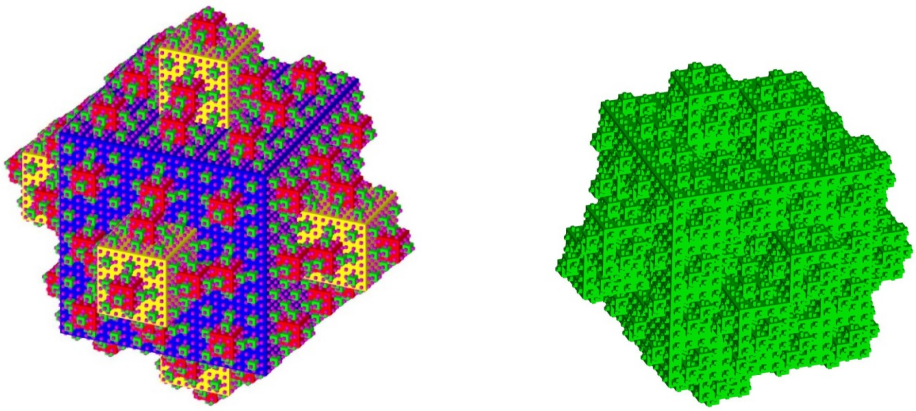

(a) Type 1 Koch Curve (shown at level 4) **(b)** Type 2 Koch Curve (shown at level 3)

Figure 3.1. Models of Koch Cubes. (a) Type 1 surface fractal dimension = $log(13)/log(3) = 2.3347$. Surface area increases by 13/9 times at each level. Volume increases at each level, asymptotically approaching value of $10/7xV_0$, where V_0 is original cube volume. (b) Type 2 surface fractal dimension = $log(32)/log(4) = 2.5$. Surface area increases by factor of two at each level. Volume remains constant at each level.

For comparison, models of other traditional three-dimensional objects (cubes, spheres, oblate and prolate spheroids) were also meshed and the same process repeated to capture the time history of the "extent of reaction" for each of the objects. Figure 3.3 shows the extent of reaction vs. time for the finite element representation of these objects as well as an analytic solution result for a sphere. While there are clearly mesh dependencies associated with the coarseness of the mesh (the extent of reaction was computed as a volumetric sum over the finite elements) the trends are clear. The traditional three-dimensional objects all follow a $t^{1/2}$ power law while the fractal objects follow $t^{1/3}$ for Koch Cube Type 1 and $t^{1/4}$ for Koch Cube Type 2 (note the dashed lines in Figure 3.3).

The trends follow expected behavior as described by Fournier and Boccara who state that this time dependency is proportional to time to the power of $\beta = (d - d_s)/2$ where d is the Euclidean embedding dimension of the object (i.e., $d = 3$ in all cases considered here) and d_s is the dimension of the surface ($d_s = 2$ for traditional objects, $d_s = 2.3347$ for Koch Cube Type 1, and $d_s = 2.5$ for Koch Cube Type 2). The time exponents β work out to be $\beta = \frac{1}{2}$ for cubes, spheres, and spheroids; $\beta = \frac{1}{4}$ for Koch Cubes of Type 2; and $\beta \approx 14$ for Koch Cubes of Type 1. The analytical solution for the temperature, T in a sphere of radius R having thermal diffusivity κ initially at zero temperature and with the surface suddenly

heated to $T = T_1$ is given by [12] as:

$$T = \frac{rT_1}{r} \sum_{n=0}^{\infty} \left\{ \text{erfc} \left[\frac{(2n+1)R - r}{3(\kappa t)^{1/2}} \right] - \text{erfc} \left[\frac{(2n+1)R + r}{2(\kappa t^{1/2}} \right] \right\} \tag{3.0.1}$$

From this equation, the temperature front propagation (i.e. r vs. time) for an arbitrary isotherm (say $T = \frac{1}{2}T_1$) can be determined. This can then be converted into an "extent of reaction", α, defined as the volume associated with $T > \frac{1}{2}T_1$ divided by the total volume, as a function of time. This analytic solution is also shown in Figure 3.3 and parallels the dashed $t^{\frac{1}{2}}$ line.

Hence, it can be seen that for complex structured "particles" (see for example Figure 5.1) the details of their morphology can contribute to the observed conduction phenomenology on this scale and potentially lead to a different homogenized response, here indicated by the value of the exponent β.

Fractal Percolation Clusters: Transient Response.

The goal of this set of simulations was to further demonstrate with finite element models the phenomena of anomalous diffusion which has been reported by Fournier and Boccara in laser-pulse heated clusters of copper spheres [25] and to motivate by illustration discussion of scale-dependent conduction phenomena and related variability.

Here we constructed a fractal network of connected cubes by building a 30x30x30 array of cubic sites (27,000 available sites) where sites were chosen at random until a total of 8400 were selected (31.11%, near the percolation threshold for a cubic lattice). This random process produced isolated cubes as well as connected clusters of cubes. The largest connected cluster was extracted and used for further analysis; it consisted of 2399 cubes and percolated in all three (x, y, z) directions. The cluster of cubes was meshed with finite elements, each cube with a 10x10x10 mesh for a total of 2,399,000 elements. Two versions of the mesh were built: a "connected mesh" in which all the elements identical, and an "isolated mesh" in which each individual cube was isolated from each other by being coated on three sides with a layer of another material (i.e., the 10x10x10 cubes were each constructed with a 9x9x9 center cube with the remainder one element wide). Figure 3.4 shows the two meshes; the 25 red patches were locations on the x=0 plane where boundary conditions would be applied.

Simulations were performed by giving all elements an initial temperature of T=0 except for the red faces which were given a 1000 K initial temperature (note the surface boundary condition temperature is effectively applied in the code as a linear profile or right-triangle-shaped pulse, 1 element deep as illustrated in Figure 3.5). All boundaries were treated as adiabatic and only thermal conduction was included (i.e., no convection or radiation). The baseline material was given properties of $\rho = 1000kg/m^3$, $\lambda = 100W/m - K$, $C = 1000J/kg - K$, $\kappa = 10^{-4}m^2/s$. For the isolated case the interface material was treated

as an insulator with properties of $\rho = 1000kg/m^3$, $\lambda = 5W/m - K$, $C = 1000J/kg - K$, $\kappa = 5x10^{-6}m^2/s$.

The object of this exercise was to observe anomalous diffusion in the vein of that observed by Fournier and Boccara. In their tests, the same locations which were initially heated, were subsequently monitored for temperature-time response. The same was done here; the temperatures of the initially heated regions (the red patches) were monitored over time. Figure 3.6 shows the time temperature response of the various locations, on a log-log scale. There are several noteworthy aspects of these figures.

First, the overall shape (almost flat profile from time of 10^{-9} sec to $\sim 10^{-6}$ sec followed by a drop-off at a rate proportional to time to the $\frac{1}{2}$ power) corresponds with the analytic solution for an initial linear profile (cf. Figure 3.5) on a semi-infinite domain (see [12] p. 54, eq. (5)). The time to reach the bend in the curve (at $\sim 10^{-6}$ sec in Figure 3.6) is related to the thickness of the applied initial right-triangle-pulse initial condition, with a thinner pulse width resulting in a shorter flat profile.

Second, beginning about $t = 5x10^{-3}$, there is a shift in temporal response from a $t^{\frac{1}{2}}$ dependency to another. At this point it is helpful to draw attention to the distinction between the various colored curves in the legend. The black curve is the average over all the temperatures monitored at the different locations. At some locations, the rate of the temperature drop is greater, at other locations lower than average; pointing to the variability of the thermal response due to the inhomogeneity of the structure. This behavior is associated with changes in the block structure of the domain, with an increase in area or "forks" resulting in a faster drop, and constrictions or partially blind paths resulting in a slowdown in the temperature drop. The time at which these variations begin corresponds with the thermal transit time across the first layer of cubes (10 elements thick) again leading to the $t^{1/2}$ decay typical for conduction in three dimensional objects with two dimensional surfaces. Note that that for some locations, the temperature history actually reverses direction temporarily and gets hotter. This is due to thermal pulses arriving from neighboring sources and driving the temperature higher.

Third, the simulations for the connected mesh eventually show a reversion to a $t^{\frac{1}{2}}$ response behavior beginning at about 10 to 20 s due to the finite size of the cluster. This completes the same kind of three-stage response as observed by Fournier and Boccara: a period of $t^{\frac{1}{2}}$ behavior associated with the conduction in the first layer of material, followed by a different slope associated with the spreading of heat from the first layer to other layers in a potentially tortuous path, followed by a repeat of the $t^{\frac{1}{2}}$ behavior associated with a homogenized or bulk response.

2-D Square Lattice of Boxes with Bridges.

This section is similar in many ways to the previous one, in that a randomized two-dimensional array is developed. However, in contrast to the previous section which had

isolated clusters and individual sites "floating in space," here all locations are connected. In this way, it was hoped that this structure, or a similar one, could be constructed experimental validation.

The geometry was a 50 x 50 array of "boxes" each of size 5 mm x 5 mm such that the overall dimension was 25 cm x 25 cm. Within certain, randomly chosen boxes a 4 mm x 4 mm hole was created, while the rest of the boxes remained intact. Overall, 872 of the 2500 boxes (34.9%) had a hole. Since there were "bridge" structures to ensure the clusters did not fall apart, even boxes with holes had some solid material. The overall fraction of solid was 77.7% with 22.3% air space. Figure 3.7 shows the geometry which was meshed with quad finite elements (10x10 per box).

Simulations of the thermal behavior of the randomized lattice were performed. The matrix material was given properties similar to aluminum ($\lambda = 200W/m-K$, $\rho = 2700kg/m^3$, $C = 900J/kg-K$, $\kappa = 8.2304x10^{-5}m^2/s$) while the holes were assumed to be air ($\lambda = 0.03W/m-K$, $\rho = 1kg/m^3$, $C = 1000J/kg-K$, $\kappa = 3x10^{-5}m^2/s$). Only conduction heat transfer was considered; convection and radiation were ignored. The initial temperature of the domain was set to zero and a constant temperature boundary condition of 80 was applied on the left side. The temperature of the center of each box (either air or aluminum) was monitored over time, such that for each x-direction layer, there were 50 values recorded. Figure 3.8 shows the temperature history of certain layers, including Layer 1 (nearest the heated surface) and Layer 50 (furthest from heated surface).

Also shown in Figure 3.8 are analytic solutions for the problem for a slab of length L and diffusivity κ, with initial temperature of zero and imposed boundary temperature of T_1 at $x = 0$ and adiabatic at $x = L$. This is given by Equation 3.0.2.

$$T = T_1 \left[1 - \frac{4}{\pi} \sum_{n=1}^{\infty} \frac{1}{2n-1} \sin\left(\frac{(2n-1)\pi x}{2L} \right) \exp\left(-\frac{(2n-1)^2 \pi^2}{4L^2} \kappa t \right) \right] \tag{3.0.2}$$

Note that the only physical property value that influences this equation is the thermal diffusivity κ. The two solutions labeled Analytic A and Analytic B are both solutions to Equation 3.0.2 but with one of two different values of the diffusivity, κ. Analytic A uses the aluminum diffusivity; while Analytic B uses a homogenized mixture value—that is in Analytic B the diffusivity was adjusted such that the solution at layer 50 (Figure 3.8(f)) matched. This happened with a diffusivity of 76.5 % of the original aluminum diffusivity.

The solution at Layer 1 (in the aluminum) agreed with the Analytic A solution at early times—until the thermal wave penetrated beyond the first layer.

Part of the goal of this study was to determine how many layers were required to get a full homogenized solution. Here by Layer 10 the solution is nearly homogenized, though it continues to improve the further from the heat source one looks. Variability on a mesoscale prior to homogenization can also be illustrated by taking the differences in temperature

between the case with holes (Figure 3.7) and a similar case without holes—pure aluminum, as in Figure 3.9.

In the layers nearest the heat source there are locations for which the case with holes exceeds the temperature of the pure aluminum case, but at other locations the opposite is true. These are caused by "constrictions" and "openings" in the heat flow paths around the holes. Away from the heated surface the "wiggles" diminish and eventually there is a uniformity of temperatures, indicating homogenized behavior has been reached at a lower thermal diffusivity.

Figure 3.10 shows full surface images of the differences in temperatures between the baseline case with holes and uniform "A" solution (i.e., Equation 3.0.2 with aluminum properties) and uniform "B" (homogenized properties, diffusivity is 0.765x aluminum value).

If we treat the baseline case with holes solution as the "true" solution (because we have accounted for material variations), we can learn something about approximations made when treating all the material with a single set of properties. In this graph, a gray color represents no difference while other spectrum colors indicate higher or lower temperatures. Note that at very early times, the true solution is slightly more closely approximated (i.e., more gray, less of other colors) by the aluminum properties solution (Uniform A). At later times and farther into the sample the homogenized solution (Uniform B) does much better. In particular, there is a noticeable error of about 5 degrees (cyan color) for an extended period of time with Uniform A, while Uniform B does pretty well for much of the simulated time and over much of the domain.

This research suggests a couple goals. One goal would be to be able to develop models that can reproduce something like the "true" solution (i.e., include spatial and temporal variations of the right magnitude, in a probabilistic sense) without requiring the full geometric fidelity (i.e., don't model the "holes" explicitly). Another goal is the a priori prediction of appropriate effective material properties based on knowledge of geometric structure (e.g. connectivity, particle sizes, void fractions, etc.) and inter and intra-particle material properties (e.g., anisotropic properties, contact conductance, etc.).

A similar set of simulations was performed with 2-D arrays of boxes, this time without holes and bridges, but rather two components—a high thermal conductivity material and a low thermal conductivity material. These were used as test cases for an exercise in considering the issues pertinent to experimental validation of multi-scale models as well as to uncertainty quantification in disordered, complex materials. These results were published at a combined AIAA/ASME conference and the resulting paper [71].

Conduction in Materials with Random Materials Structure

The next two subsections explore simulation capabilities aimed at investigating the role of disorder in the materials micro-structure during thermal conduction. Two systems are described both consisting of anisotropic materials. The first consists of a pack of disks composed of anisotropic materials with random orientations. While the second shows a notional polycrystalline material with random grain orientations. In each case it is assumed for simplicity that thermal transport is well described by the diffusion equation.

2-D Array of Disks with Randomly Oriented Non-Isotropic Thermal Conductivity.

Here we examine the effects of non-isotropic thermal conductivity on the heat transfer through a multiple particle structure. The geometry was a two-dimensional array of disks arranged in a hexagonal close-packed arrangement between two plates. Each individual disk was assumed to be constructed of a material with highly non-isotropic thermal conductivity with a value of 100x in the "grain direction" vs. 1x in cross grain direction. (These were purely hypothetical but one might imagine some materials such as filled composites may have widely disparate properties in the various directions.) The disks were oriented in a random angular orientation such that the grain direction varied. Perfect thermal contact between disks (shared nodes) was assumed. The plates were used to apply temperature boundary conditions at the top and bottom surfaces; the plates themselves had very high thermal conductivity so that the temperature BC would be uniformly applied. Figure 3.11 shows the overall geometry meshed with quadralateral finite elements as well as the randomized grain orientation used.

Figure 3.12 shows the temperature profile for an imposed set of boundary conditions: T=1000 on the lower surface and T=0 on the upper. Note that the isotherms are not parallel, indicating non-uniform heat conduction. Figure 3.13 shows the corresponding heat flux paths through the disk array. There appear to be several preferential "channels" for heat flow. There also appear to be some locations which show an "eddy" like flow of heat (upstream to the overall bottom-to-top temperature gradient).

The detail of heat flow through Disk 34 (fourth row up, fourth disk from left) shows some interesting phenomena. Within that one disk, heat flow in several different directions occurs simultaneously, with an overall circuitous route. There are heat flow "entries" at the 3 o'clock (main entry), 5 o'clock, and 9 o'clock positions; and heat flow "exits" at the 1 o'clock (main exit), 7 o'clock and 11 o'clock positions.

One reason for modeling the particular set up here (i.e. disk array) was the potential for building a similar experimental set-up which could be used as a test system for an IR camera (see next Chapter). We discussed building an array with disks of various thermal

properties (randomized anisotropic, or mixture of high conductivity disks with low conductivity disks, etc.) and some method of heating (perhaps a heated copper plate at one end and a water-jacketed, cooled copper plate at the other). However, this particular system was not constructed.

3-D Random Grain Structure in Cube.

Here we examine perhaps a more realistic geometry, in terms of materials micro-structure, which approximates a polycrystalline material. An overall cube was constructed, then subdivided into separate "grains" by passing cutting planes through the cube at various locations and orientations. The final mesh consisted of 162 separate grains within the cube, and a randomized grain orientation direction was assigned to each one. Figure 3.14 shows the mesh and associated grain orientation vectors.

The grains were assumed to be similar to quartz crystals, having an anisotropic thermal conductivity which was 10 W/m-K in one principal direction and 5 W/m-K in the other two principal directions. The simulation consisted of applying a 1000 degree boundary condition on one side of the cube, with the opposite side having a 0 degree boundary condition. The four remaining sides were treated as adiabatic. Steady state solutions were obtained and then processed to obtain heat flux and a value of effective thermal conductivity. No contact resistance between grains was included; all shared grain faces had shared nodes.

Figure 3.15 shows the temperature profile and heat flux pathways produced by this simulation. The temperature contours are nearly parallel, though some asymmetries also appear. There are also some preferential heat transfer paths apparent. Overall the effective thermal conductivity from this particular instance was determined as 6.45 W/m-K. This is between the 10 W/m-K and 5 W/m-K principal direction values, but closer to the lower value. This might be expected given that two principal directions had the lower 5 W/m-K and only one direction had the 10 W/m-K value.

One might imagine building a series of these kind of computational models, each having different randomized structures and then performing the simulations to produce statistical variations. However, this remains for future work as does the creation of more realistic geometries of polycrystalline materials (see below).

Another aspect that should be remembered is that the thermal transport between individual grains having different orientations is not perfect as has been assumed here. The lattice vibrations characterizing thermal waves will not perfectly transfer across grain boundaries. Thermal contact resistance could be used to reproduce some of these effects, but knowing a priori what value to use for this becomes a more difficult problem. Other portions of this report delve into this area at a more fundamental level.

Creating Computer Models of Sub-Particle Microstructures

Following the initial scoping simulation of the previous subsection, more accurate polycrystalline geometries were generated by the Monte Carlo Potts (MCP) model [32] on a domain of 128x128x128 lattice sites for a total of just over two million. A total of 1,380 MCP simulations were performed, each with a different initial distribution of uniform random site occupancies, in order to create a population of distinct micro-structure models with similar overall characteristics. Simulation configurations were extracted after twenty million, thirty million, and fifty million MCP time steps, producing average grain volumes of approximately 1,200, 7,600, and 78,000 lattice sites respectively. Thus, a total of 4,140 distinct polycrystalline models was created for this study.

The voxellated polycrystalline models were converted into finite element meshes by simply creating a single, eight-node, cubic, hexahedral element for each voxel. Groups of voxels / elements were assigned unique material indices to demarcate the grains in the model. Figure 3.16 contains examples of three models from each grain size. These models of polycrystalline microstructures can be overlaid onto models of thermal transport in order to incorporate the effects of sub-particle microstructures on thermal transport. However, the continuation of this remains for future work.

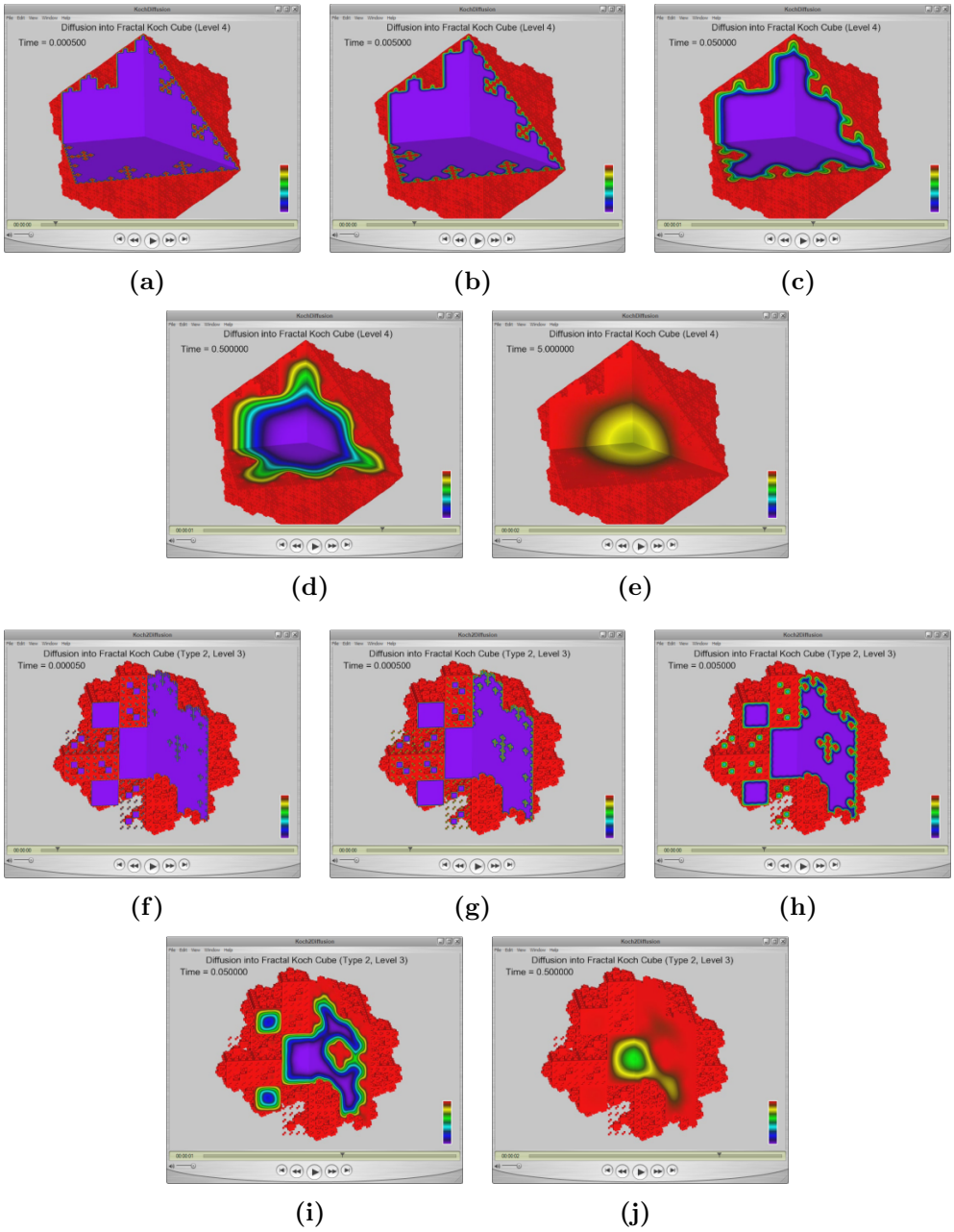

Figure 3.2. Evolving temperature history in Koch Cube models (a thru e: Type 1 (level 4); f thru j: Type 2 (level 3)). Images from left to right are at times of $5x10^{-5}$, $5x10^{-4}$, $5x10^{-3}$, $5x10^{-2}$, and $5x10^{-1}$ sec, respectively.

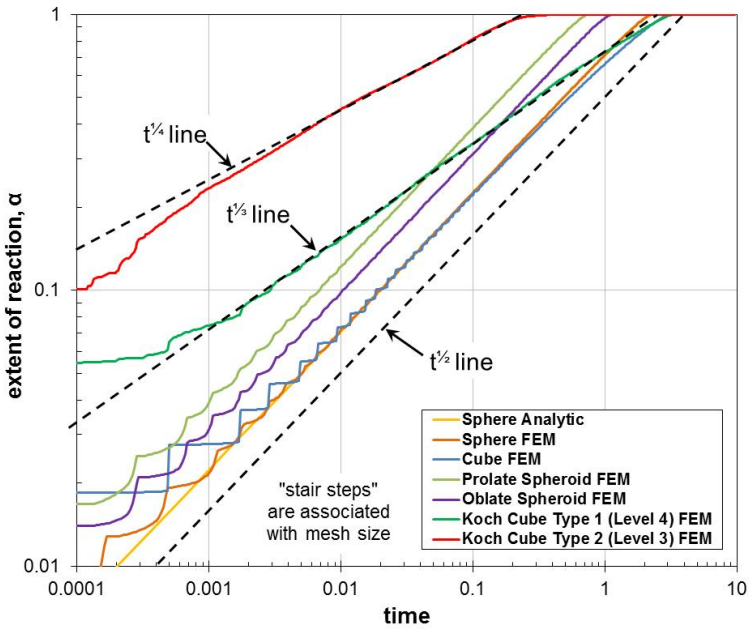

Figure 3.3. Extent of reaction vs. time for various 3-D and fractal objects.

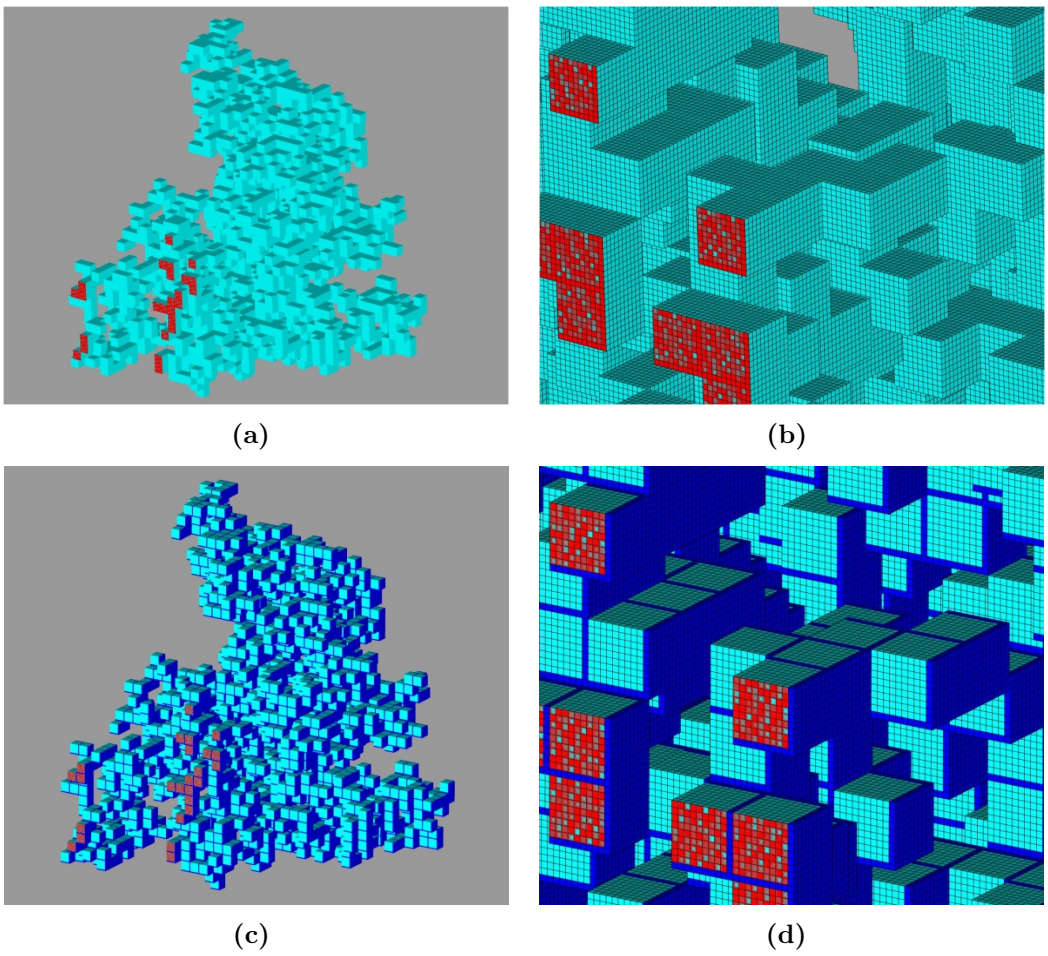

Figure 3.4. Connected and Isolated cluster finite element meshes. (a, b) Connected Mesh; (c, d) Isolated Mesh

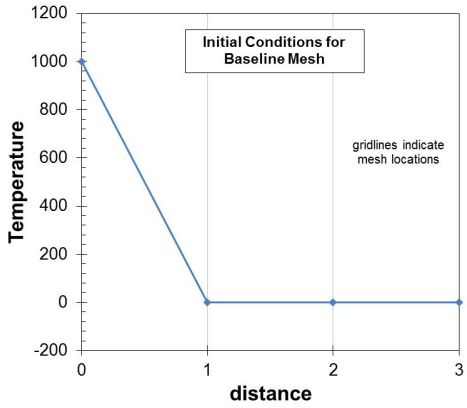

Figure 3.5. Initial condition applied to surface of red faces in Figure 3.4. Distance is in terms of element thickness.

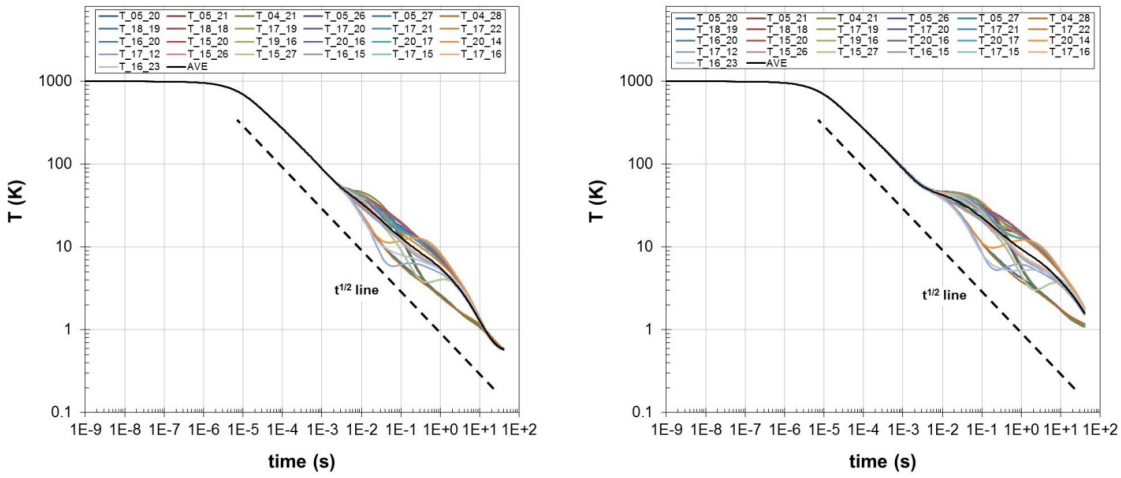

(a) **(b)**

Figure 3.6. Temporal response of heated regions in the two meshes of Figure 3.4. The two numbers in the labels of each line are coordinate locations on the heated faces (i.e., the first one is 5 units over and 20 units up on the original 30x30 cube face). (a) connected mesh thermal response; (b) isolated mesh thermal response

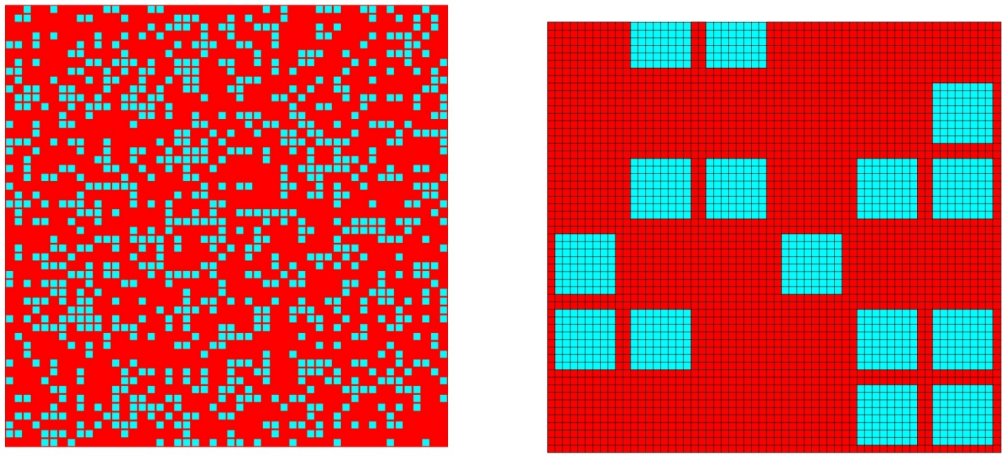

(a) **(b)**

Figure 3.7. 2-D square lattice of boxes with bridges. Red is matrix (aluminum properties), blue is void space (air properties). (a) Overall Box Array; (b) Close-up of lower left corner with FE mesh.

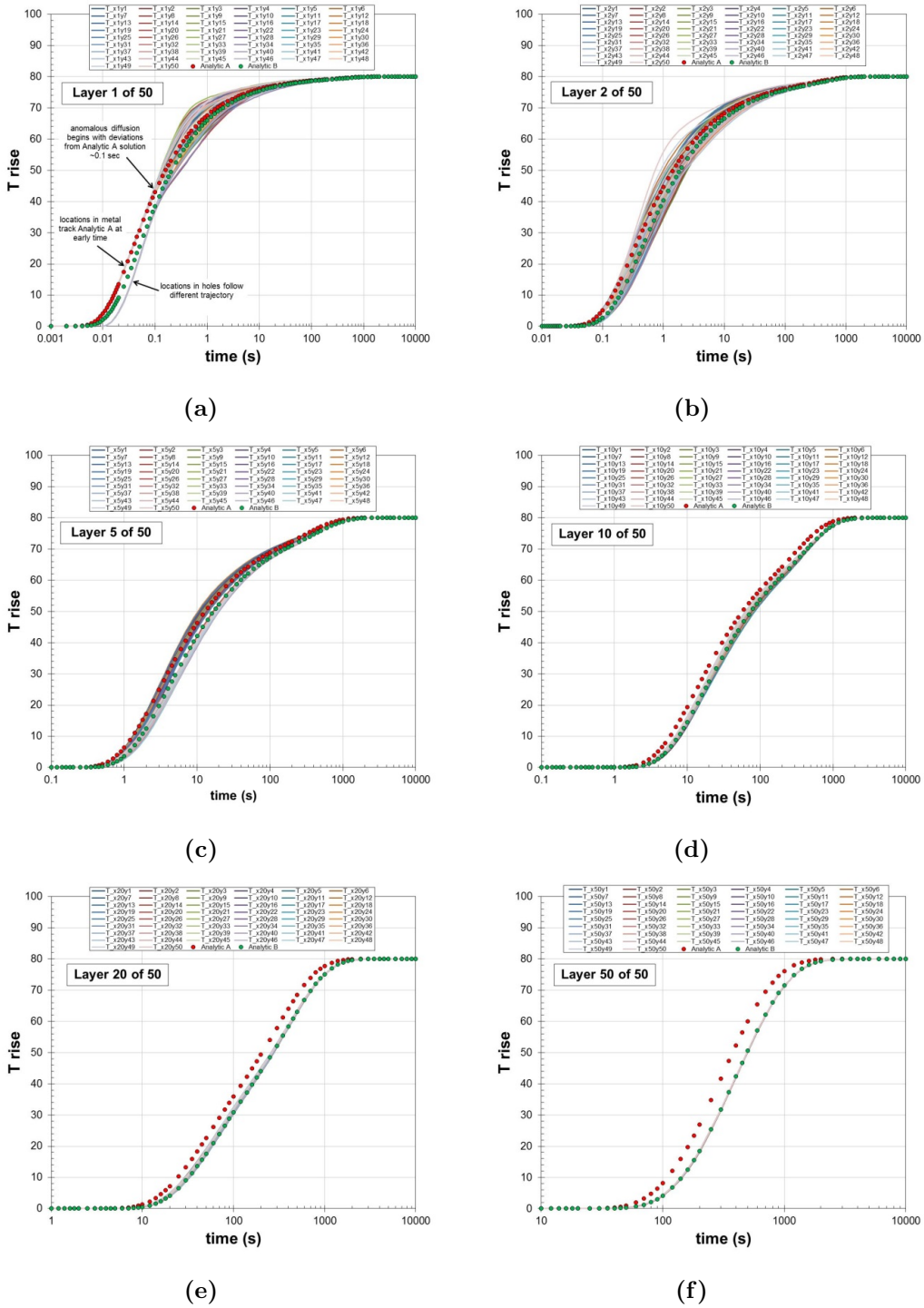

Figure 3.8. Temperature histories (lines) for several different layers in randomized box array (layer 1 is nearest to the heated boundary). Red dots represent the analytic solution for aluminum properties. Green dots represent the analytic solution for a homogenized mixture of aluminum and air.

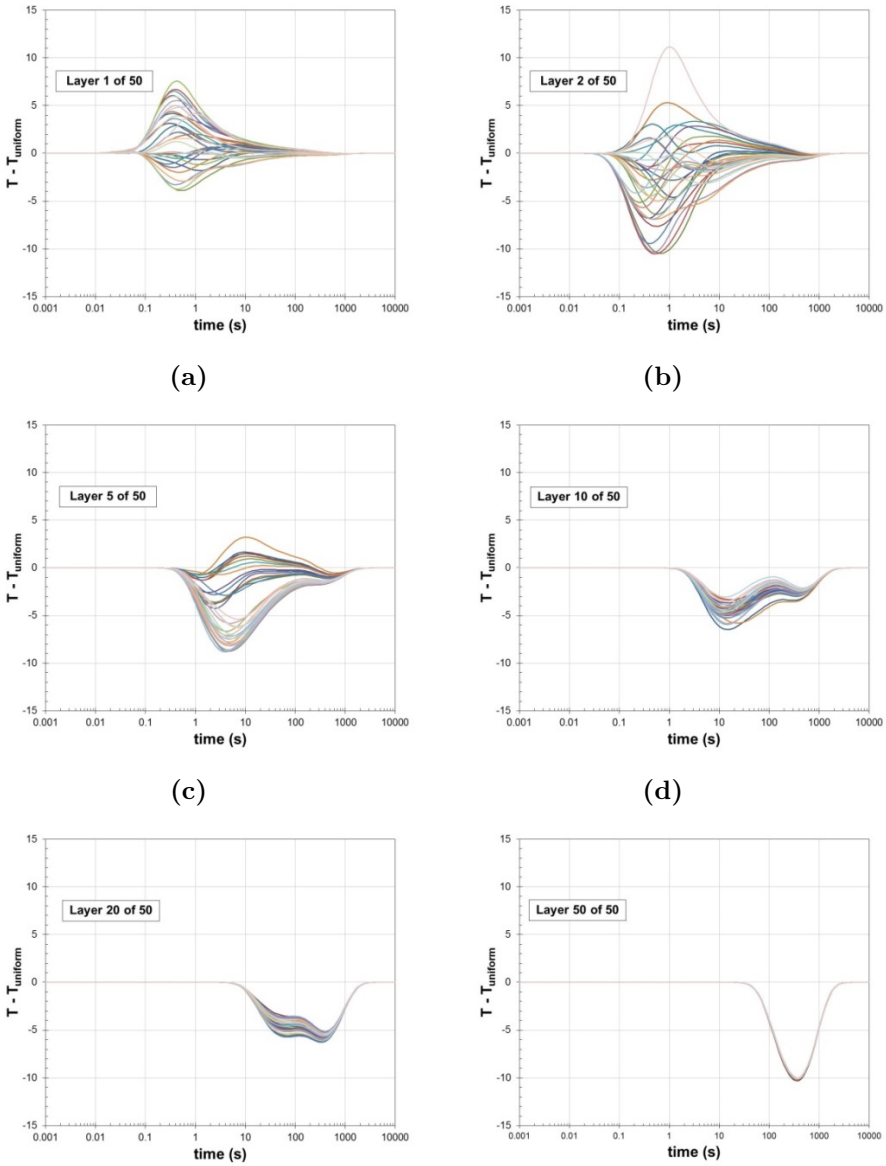

Figure 3.9. Deviation of temperature profiles from uniform temperature at various locations in random checker board system as function of time. The temperature at the center of each box in each layer is represented as a separate line.

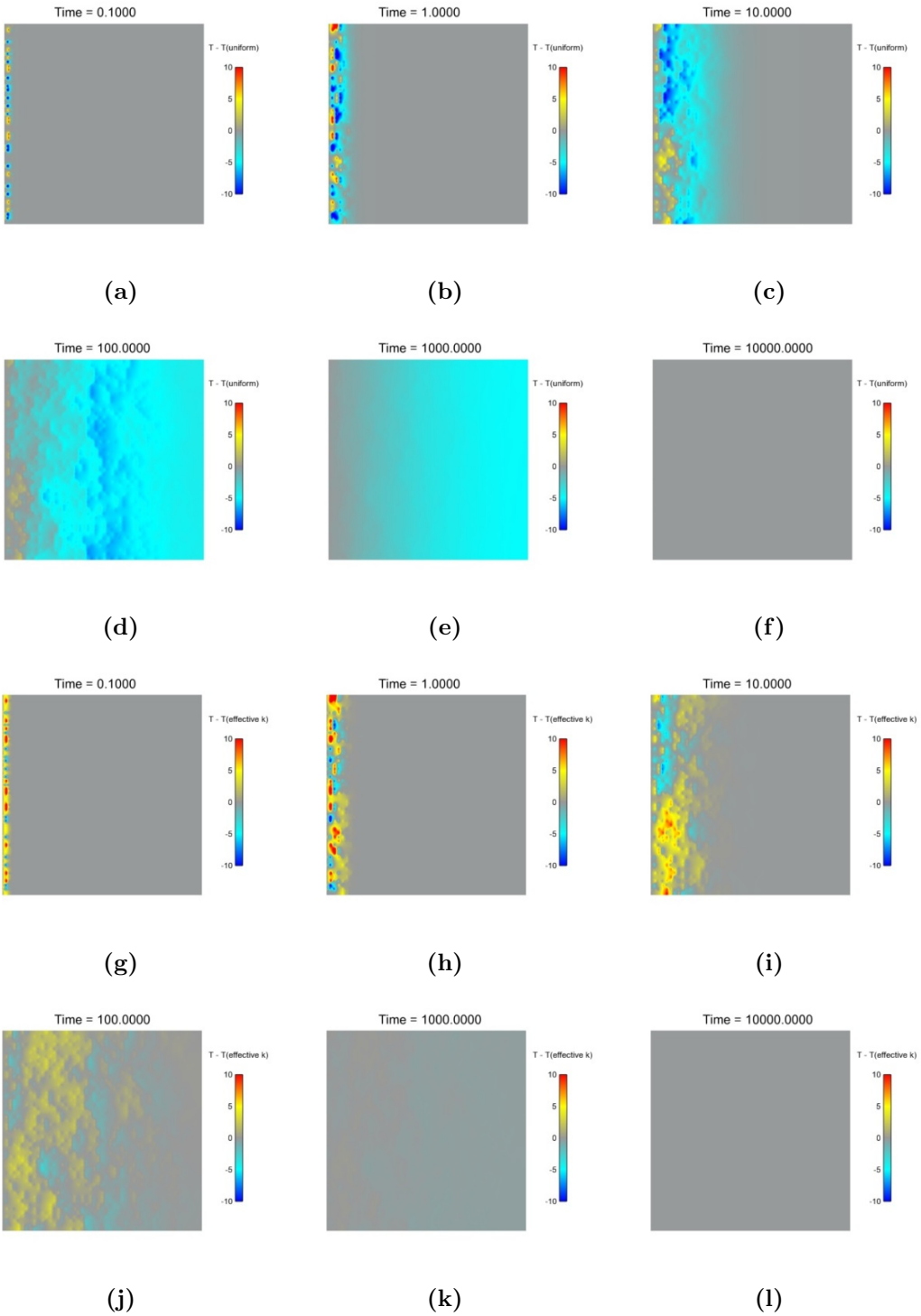

Figure 3.10. Deviation of temperature field: (a thru f) from uniform temperature at different time planes; (g thru l) from thermal field given by effective conductivity.

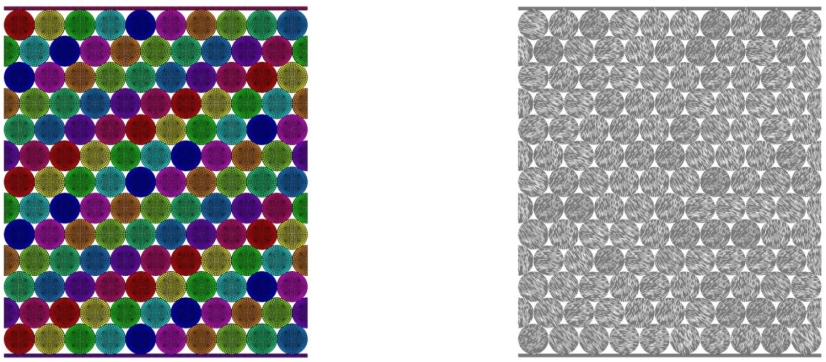

(a) **(b)**

Figure 3.11. Finite element mesh and grain orientation of 2-D disk array. (a) Finite Element Mesh of Disk Array; (b) Grain Orientation.

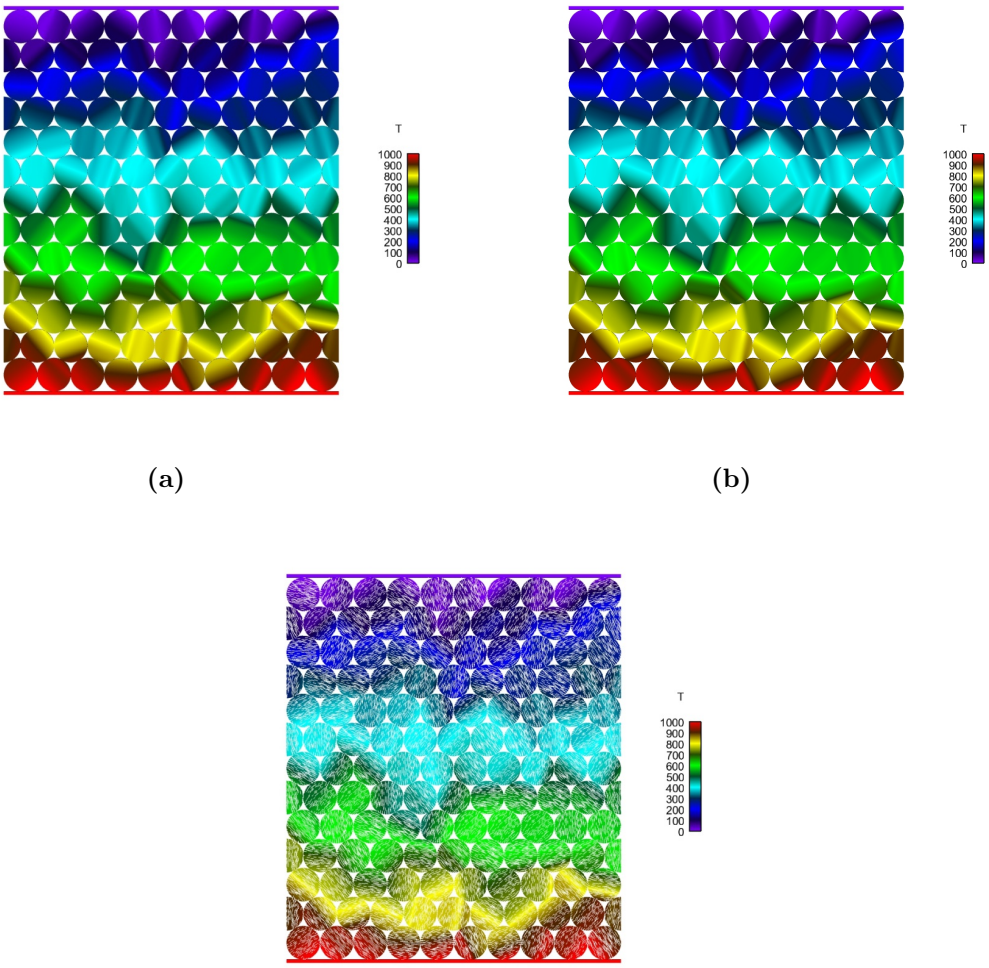

Figure 3.12. Steady-state temperature profile in Disk Array. (a) Temperature; (b) Temperature with Grain Orientation.

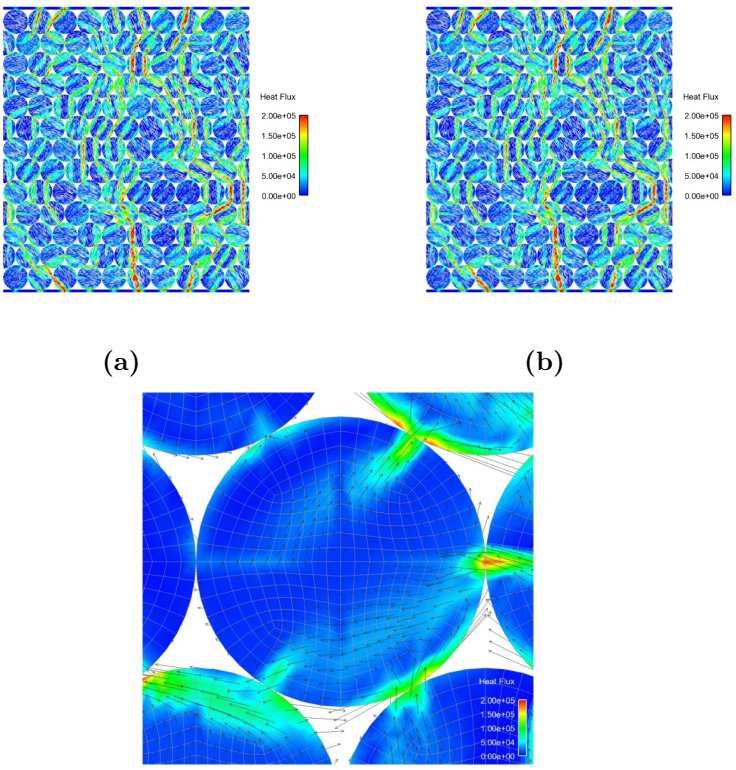

Figure 3.13. Heat flux pathways through disk array. In the left graph, X marks Disk 34. In the right graph, arrow indicates grain orientation of Disk 34. (a) Heat Flux Paths; (b) Detail of Disk 34.

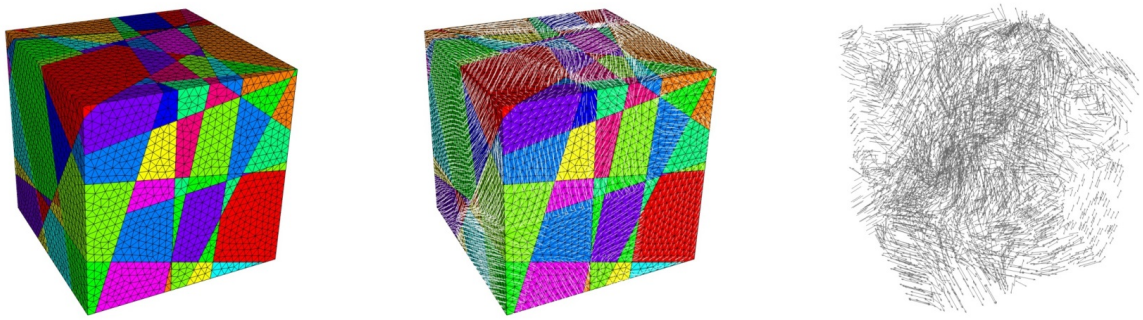

(a) **(b)** **(c)**

Figure 3.14. Cube consisting of 162 grains each of which has a randomized orientation. (a) Mesh (162 Grains); (b) Mesh and Grain Orientation Vectors; (c) Grain Orientation Vectors

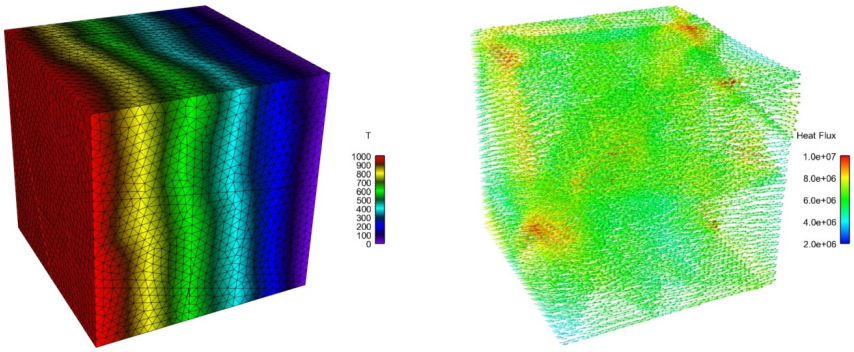

(a) **(b)**

Figure 3.15. Finite element mesh and grain orientation of model polycrystal. (a) Steady State Temperature Profile; (b) Heat Flux Pathways.

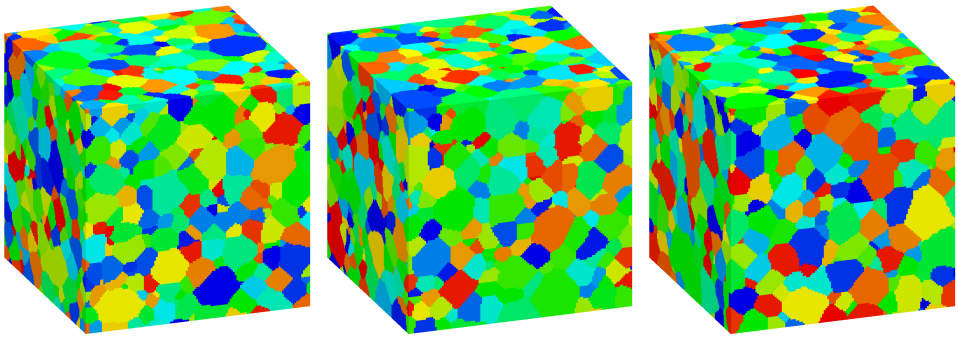

(a)

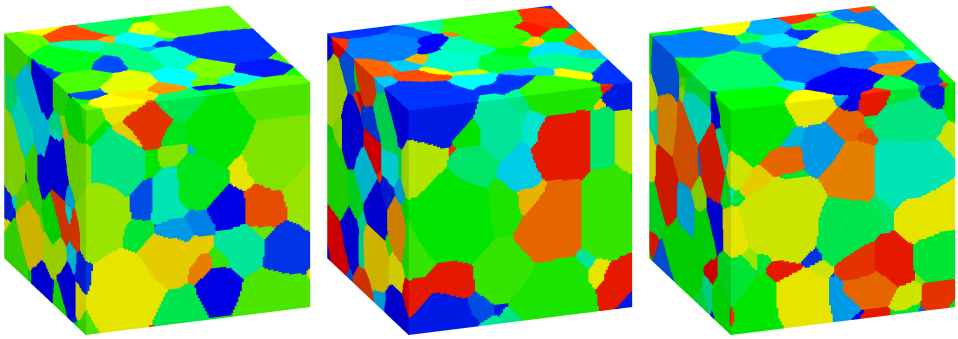

(b)

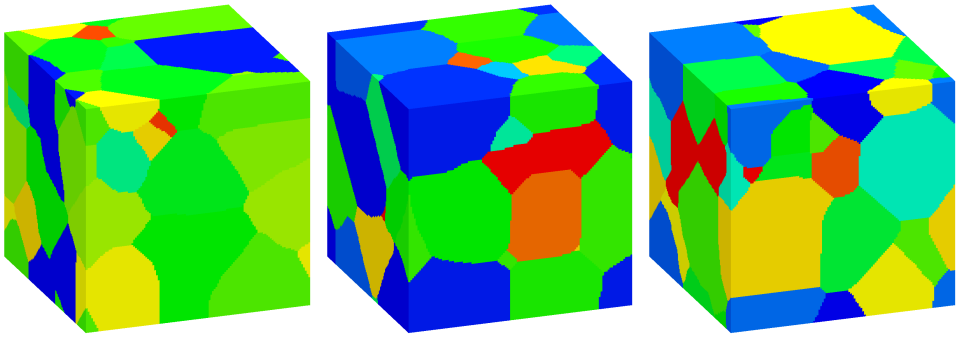

(c)

Figure 3.16. Models of polycrystals containing grains of approximate average volume a) 1,200; b) 7,600; and c) 78,000 voxels / finite-elements. The coloring is arbitrary, and meant only to distinguish one grain from another.

Chapter 4

Probing the Inhomogeniety of the Thermal Field in Pressed Pellets via Infrared Camera

The simulations in the previous chapter demonstrated the inhomogeneity of the thermal field due to structure on the mesoscale. In fact, it is the cross-over from homogeneous micro-scale to homogeneous macroscale which defines the "between" or meso-scale with its attendant variability. Clearly it is the inhomogeneous structure which regulates this process. Hence, characterizing the relationship between random meso-structure and transport properties is of considerable interest for prediction and control of the performance of these types of materials in various applications.

In this chapter, we seek to conduct a spatially and temporally resolved assessment of thermal transport in pressed powder beds. A measure of thermal transport within porous powders was conducted through the integration of a thermal imaging camera to macroscale porous test sample. Other methods of assessing thermal transport are typically conducted in a manner that averages the temperature profiles within the material or on a surface in time and space. Through the acquisition of a high-speed thermal imaging camera, the ability to monitor the thermal transport at relevant timescales and with high spatial resolution on the order of the particle sizes are possible.

Experimental Setup

A bench-top experiment coupling a thermal imaging camera to two slabs of pressed powder sandwiched around a heat source was built. This experiment (Figure 4.1) was designed around the need for thermal imaging with spatial resolution suitable for resolving particles and particle boundaries. The heat source consisted of a Tophet C ribbon connected to a constant current supply. This ribbon heater was stretched between an anchored copper block and a copper block mounted to a spring loaded micro slide that keeps the ribbon in tension as it expands and contracts during heating and cooling. The test sample slabs were held against the ribbon heater with adjustable aluminum blocks with width equal to 1.27 cm. The top aluminum block was pressed against the sample and fixed in place with a screw.

When electrical current was supplied to the ribbon heater, both mating surfaces of the slabs were heated nearly uniformly. Electrical current was instantaneously applied ($< 10\mu$s) and remained at a constant value until removed. Typical current values of 1-2.5 amps were used.

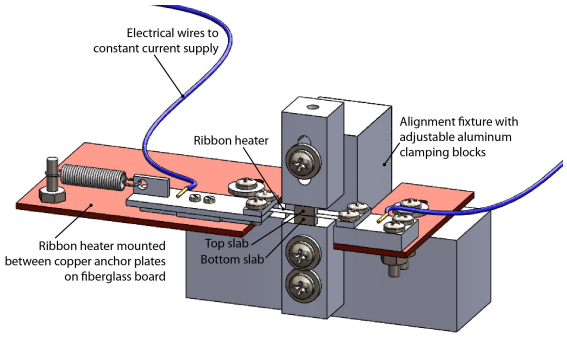

Figure 4.1. Illustration of the ignitor and pellet alignment fixture for observation of thermal transport.

The Tophet C ribbon had dimensions 50.8 um thick by 2.54 mm wide. The length of the ribbon spanned two copper anchoring plates between 17 to 24 mm apart. This separation distance was limited by the use of aluminum clamping blocks and the working distance of the spring. The stationary copper anchoring plate had dimensions of 19.3 mm x 12.8 mm x 4.9 mm and was attached with machine screws to an electrical grade (GPO3) fiberglass board. The ribbon was clamped to the anchoring plate with a copper bar, 6 mm x 12.8 mm x 1.4 mm. The other end of the ribbon was clamped in a similar manner to a thinner plate, 38.2 mm x 12.8 mm x 1.4 mm. This plate was attached to a precision ultra-miniature ball bearing carriage, McMaster-Carr part number 8381K29, allowing for 28 mm of travel. Electrical connections to the ribbon are made at both copper blocks by soldering on 18 AWG wires which were routed to a constant current power supply. The constant current power supply was connected to the ribbon heater by 18 AWG wire. This was all mounted to the test apparatus, as shown in Figure 4.2, which was machined from Delrin and allowed the fiberglass board (Figure 4.1) to be adjusted for alignment. The Delrin body was fastened to an array of micrometer adjustable translation stages that provide lateral and rotational adjustment in the x, y and z direction. A 1 m rail connects the camera to the stack of translation stages allowing quick realignment of the target (Figure 4.2).

The presented faces of the pressed powder slabs were monitored during heating with the thermal imaging camera. The camera and lens arrangement consisted of a FLIR SC8203 infrared camera with a 4x objective for a field of view that was 4.6 mm square (Figure 4.3). The camera CCD was a 1024 x 1024 pixel array for a spatial resolution of 4.5 μm/pixel. ExaminIR software was used for setup and control of the camera.

Samples were prepared by lapping the desired material to 2.54 mm x 2.54 mm by 6 to 12 mm long. This lapping process used progressively finer silicon carbide paper with the finishing passes at 1200 grit. The maximum length of the samples was limited to the width

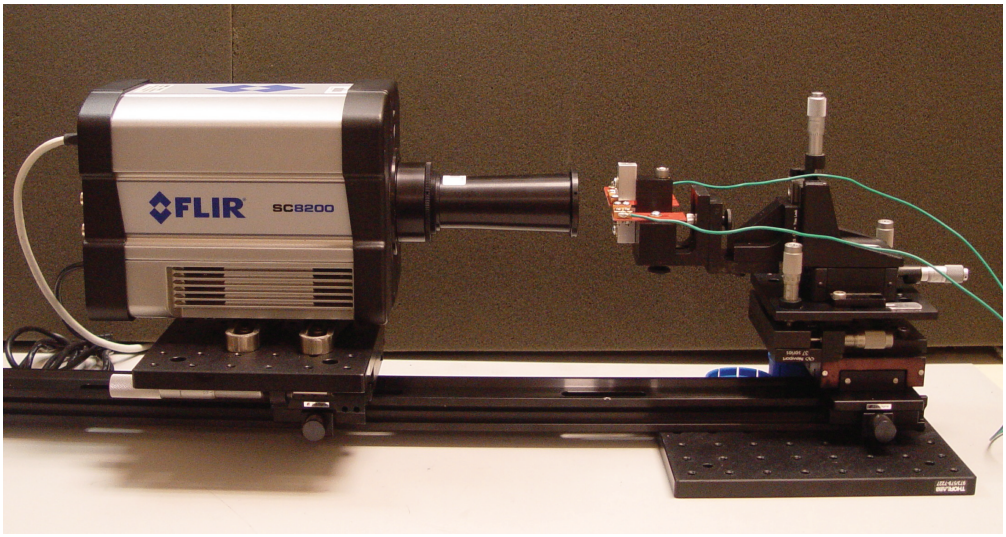

Figure 4.2. Photograph of IR camera for observation of ignitor and pellets arrangement.

of the aluminum clamps and the minimum by the source of the sample material. Ammonium perchlorate (AP) samples were lapped from 0.635 cm diameter pressed pellets made from 200 μm mean particle size and pressed to 94% TMD.

Because of the short depth of field when using the 4x objective, precise alignment was required. The edge of the ribbon closest to the camera must be lined up vertically with the front surface of the upper and lower pellet and the upper and lower clamping blocks. This was accomplished with a 1 mm thick aluminum wafer cut to fit under the top screw that secures the lower clamping block (left photo of Figure 4.4). Once installed, all components were aligned to the surface of the wafer facing the stack. The stack was clamped in place and the alignment wafer was removed (right photo of Figure 4.4).

Additive manufacturing samples

Before discussing the result of the pressed powder samples we performed a series of tests on additively manufacture plastic samples. Videos were collected from samples of a regular grid made by additive manufacturing with a thermoplastic (Figure 4.5). For these tests, the sample was simply placed on one of the narrow edges onto a hot plate that was controlled to nominally 70C. The thermal transport was recorded in videos with the IR camera. Due to the edge effects of the thin plastic sample, imperfections in the hot plate temperature uniformity and lens effects a radial temperature profile was measured.

Nonetheless, spatial line outs of temperature extracted from the video images are plotted in at various times in Figure 4.6 where the effect of the open spaces in the grid reflect

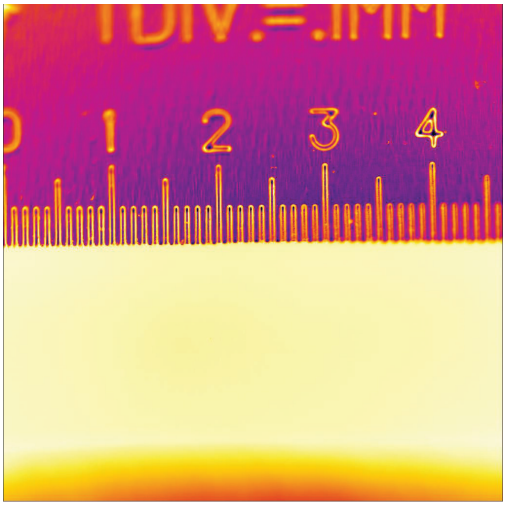

Figure 4.3. Scale measurement of FOV for 4x microscope lens.

a different temperature than the plastic regions as expected. This is observed at a y-axis position of 748 pixels (middle image of Figure 4.6). Very near the hot plate surface is a nearly constant temperature profile within the plastic sample (within the imposed radial artifact mentioned previously) as shown in the right image of Figure 4.6. Whereas, the temperature variations due to the disturbance provided by the open regions of the grid are observed in the solid area between two rows of open spaces as shown in the left image of Figure 4.6).

Experimentation with this additive manufacturing sample provided an convenient test bed for understanding camera operation, video data collection and Matlab processing. However, the non-ideal use of a hot plate and the sample variations inherent in the 3D printed parts resulted in limited testing with these samples. Even so, comparison to simulations in made in the following subsection.

Modeling of AM Samples

An attempt was made to capture the thermal behavior of the as-built and as-tested article with a checkerboard pattern of square holes or windows. A finite element mesh of the additive manufactured part was built along with a mesh of a flat plate representing the heater plate.

The article was assumed to be loosely attached to the heater; thermal transport from the heater to the article was done via a thermal contact conductance (a value of 20 W/m2-K was used). Thermal radiation heat transfer was represented using a partial enclosure configuration with the external field having an emissivity of one and a temperature of 300 K. All surfaces of the plate and checkerboard article were assumed to have an emissivity

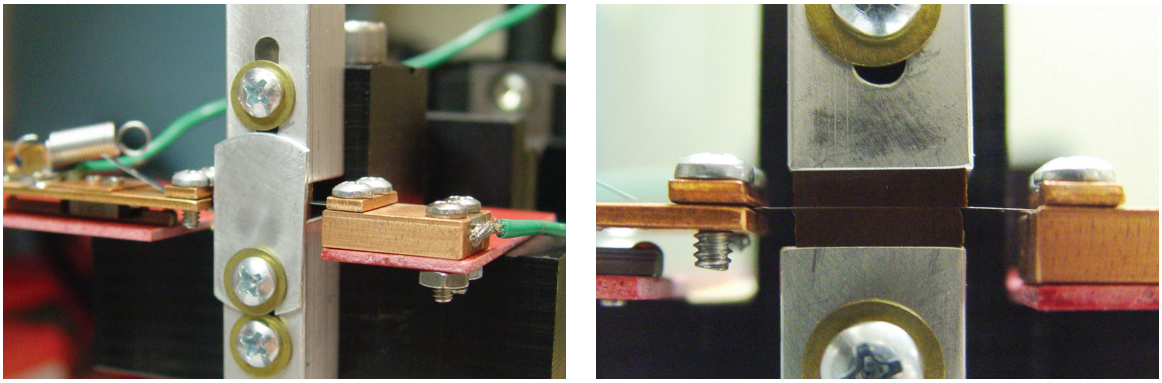

Figure 4.4. Photograph of aligned pellets and alignment process to accommodate narrow depth of field.

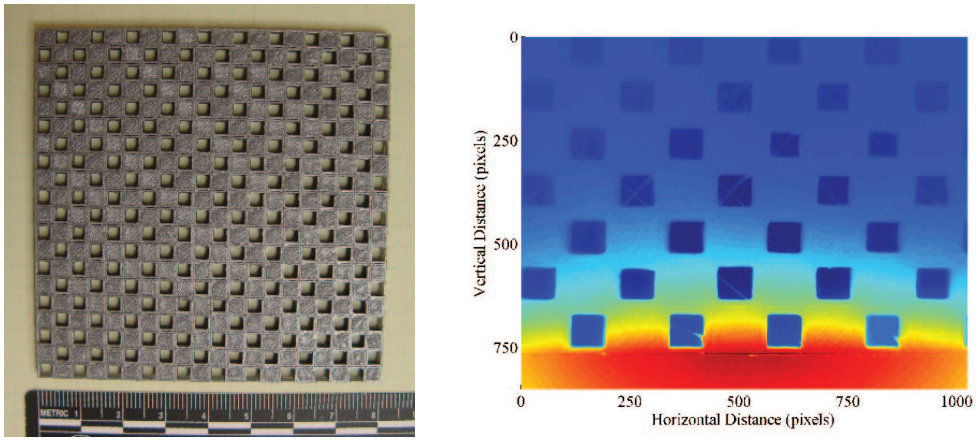

Figure 4.5. Spatial temperature histories at line-out within region of interest showing sample heating in time.

of one. The article was initially at 300 K (27C) and the temperature of the plate was maintained at 360 K (87C). Thermal properties of the checkerboard article were estimated as ρ=500 kg/m3, Cp=1200 J/kg-K, and κ=0.1 W/m-K.

The calculation was run for 10 min of simulated time. Figure 4.7 shows the mesh of the article atop the heater plate and the temperature at t=10 min. Note the arched shape of the temperature profile. This is due to radiative heat transfer, where the middle portion sees a greater fraction of hot heater plate than do the left and right sides which see more of the relatively colder surroundings.

Temperatures across the front face, midway between the first and second row (from bottom) of holes, were monitored and recorded at 1 sec intervals. Figure 4.8 shows snapshots of temperature at t=5 sec and t=30 sec; temperature scales were adjusted to highlight the

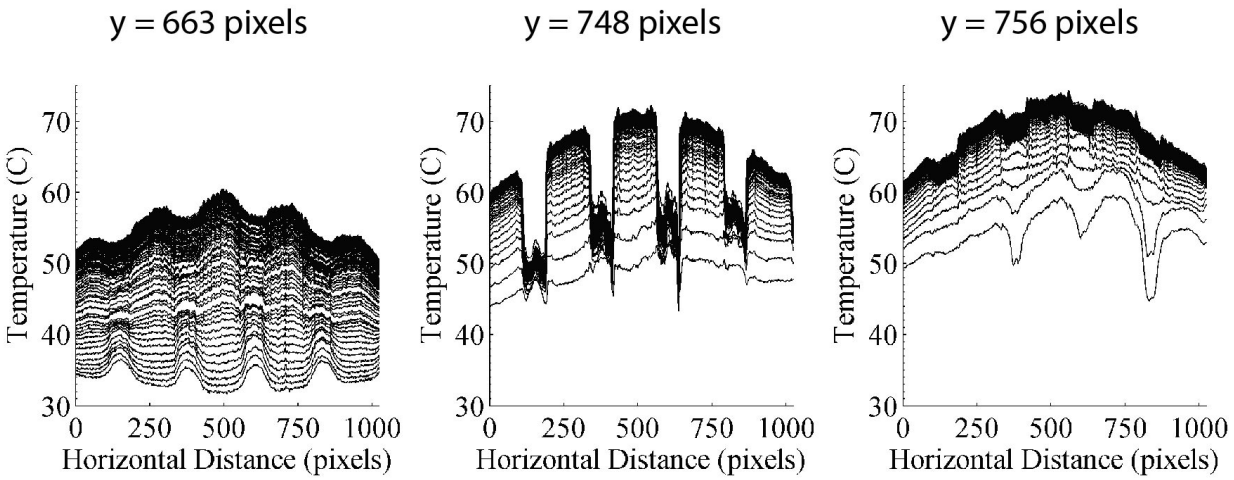

Figure 4.6. Spatial temperature histories at line-out within region of interest showing sample heating in time.

distributions about the region between first and second rows of holes. Note that in the t=5 sec images there is a "cap" or "halo" of slightly elevated temperature above each of the windows. This is due to radiation heat transfer-the upper surface of each window can directly see the hot heater plate so it receives extra thermal loading. By the time the t=30 point is reached, the profile has switched such that the region above the windows is cooler than the windowless regions; this is due to thermal conduction beginning to dominate.

The left to right temperature profiles recorded at 1 sec intervals between t=5 sec and t=30 sec are plotted in Figure 4.9. Note that scalloped shape of the profile which inverts over time: at t=5 sec, the regions directly above the windows are slightly hotter than the windowless regions. At t=14 sec, the profile is nearly flat. By t=30 sec, thermal conduction has resulted in the windowless region becoming hotter that the region above the windows (compare experimental data in Figure 4.6).

Figure 4.9 resembles qualitatively the results taken from the experiment as shown in Fig 4.6, complete with the scalloped shape and the switching of hot locations from above the windows to the non-window locations. More quantitative agreement could likely be achieved with better information on the material properties and a more complete model of the experimental set-up.

Homogeneous samples

Videos were collected from machined slabs of Vespel plastic assumed to be a homogeneous material suitable for comparison with porous samples of later testing. The ribbon heater appears as a thin boundary between the two mating faces of the Vespel slabs at the center

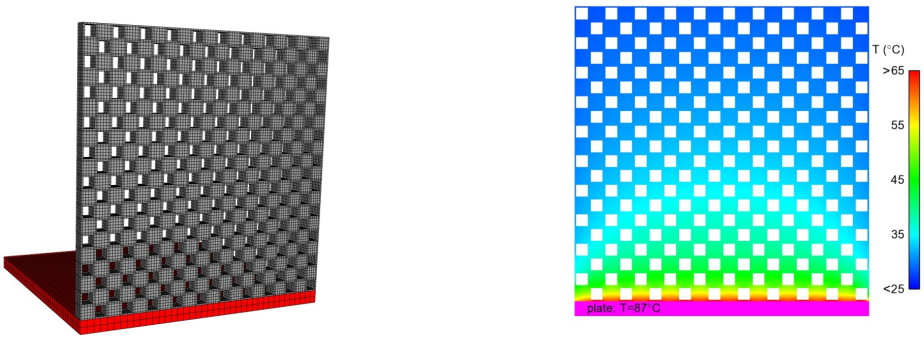

(a) **(b)**

Figure 4.7. (a) mesh of checkerboard AM article atop heater plate. (b) temperature profiles at a simulated time of 10 min.

of the region of interest (Figure 4.10).

Through analysis of the collected images in time, temperature histories at fixed spatial location was extracted. Temperatures across the region of interest at a position of 23 μm below the ribbon heater are plotted for times during heating for a low and high constant current value (Figure 4.11). The profiles are nearly of uniform temperature in space and time as would be expected from a homogeneous sample. The signal-to-noise differences are observed depending on the magnitude of the thermal gradient established by the current value and the required camera integration time. Slight spatial variations in the temperature are observed and likely due to an imperfect contact at the heater-slab interface or material variations.

Powder samples

Videos were collected from pressed pellets of ammonium perchlorate powders with mean particle size of 200 μm and 94%TMD. The ribbon heater appears as a thin boundary between the two mating faces of the powder slabs at the center of the region of interest (Figure 4.10). The video was collected at 30 fps although faster and slower collection rates were possible. 1862 images were collected such that statistics could be extracted from each image as a function of time.

The same spatial line-outs of temperature were collected as a function of time at different current values as shown in Figure 4.12. Here, the effect of material variations are observable within the temperature histories that are distinctly non-uniform as compared to the profiles of Figure 4.11.

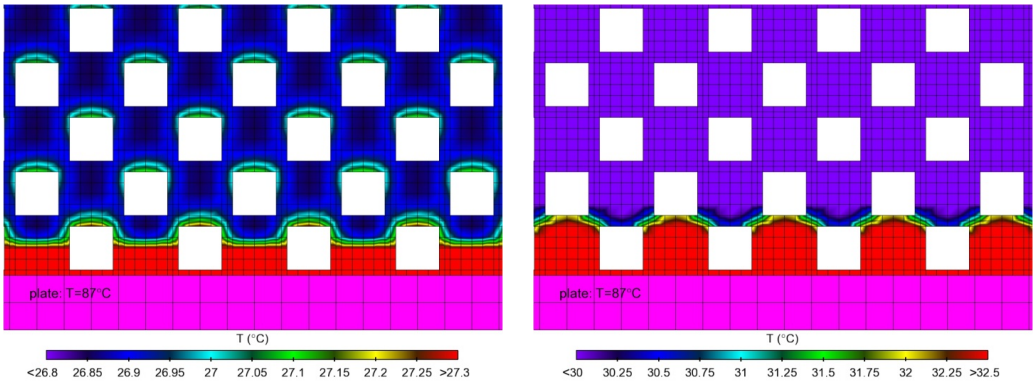

(a) **(b)**

Figure 4.8. Details of temperature profile highlighting the region between the first and second row of holes. Left: at t=5 sec; Right: at t=30 sec.

Summary

An experimental capability has been established for the observation of thermal transport processes in porous materials at relevant time scales and spatial scales suitable for particle size resolution. This work only began to explore the data collection opportunities from this experiment and future work will be focused on the application of heat transfer between hot wires and pyrotechnic beds. Additional efforts on the temperature data extraction from the volume of collected images and determination of frequency content as it relates to measurable material characteristics is a worthy next step.

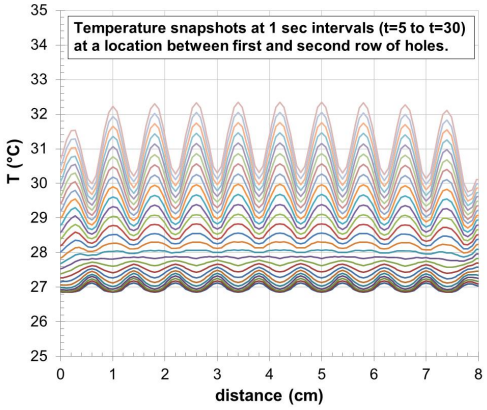

Figure 4.9. Temperature snapshots between the first and second row of windows taken at 1 sec intervals from t=5 sec to t=30 sec.

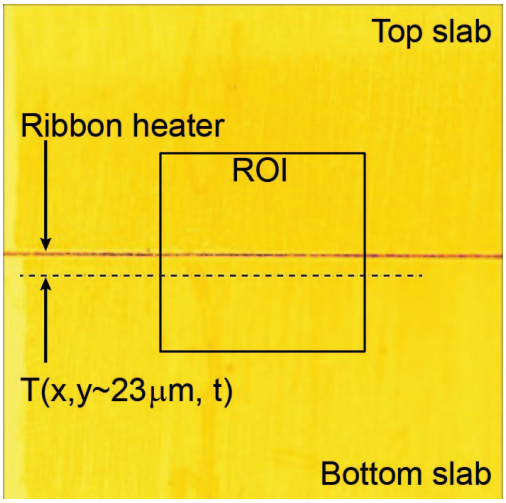

Figure 4.10. Camera FOV and region of interest for data analysis showing ribbon heater location between top and bottom pressed pellet slab.

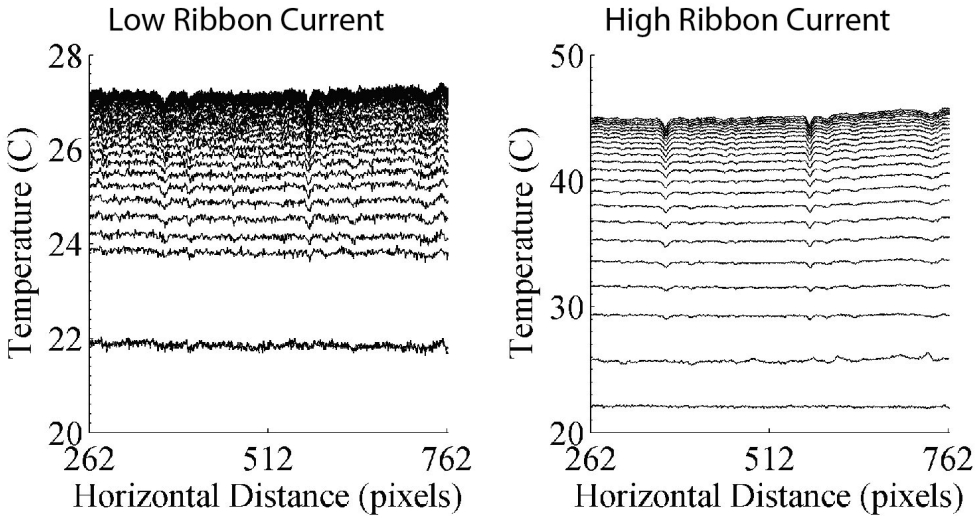

Figure 4.11. Spatial temperature histories at line-out within region of interest showing sample heating in time.

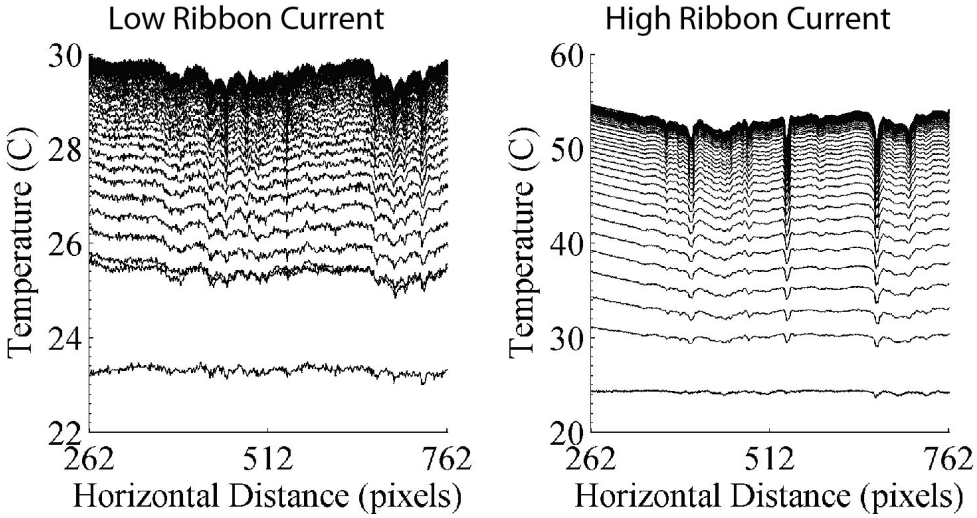

Figure 4.12. Camera FOV and region of interest for data analysis showing ribbon heater location between top and bottom pressed pellet slab.

Chapter 5

Computational Thermal Analysis of Pressed Pellets Based on FIB-SEM Data

In this chapter we consider mod/sim approaches to analyze inhomogeneous temperature fields in physical microstructures obtained from pressed powders. We present a set of tools for constructing models suitable for thermal analysis based on microstructures obtained by serial sectioning imaging experiments. In particular, we set out to calculate the effective bulk conductivity of a pyrotechnic material composed of a mixture of potassium perchlorate ($KClO_4$) and Titanium (Ti) given the spatial arrangement of its components as measured by focused ion beam scanning electron microscopy (FIB-SEM). The computed effective thermal conductivity is then compared to experimental flash diffusivity measurements.

The comparison is not straightforward, since the Ti phase is highly porous, with microstructural variations on length scales that cannot be resolved by FIB-SEM. We therefore use a Bruggeman effective medium approximation for the Ti phase as input to the simulations of the composite powder, and infer the porosity of the Ti phase based on comparisons between experimental and simulated bulk conductivity values. Fair agreement is obtained for realistic porosity values, suggesting that the overall approach is feasible. However, given the complexities of thermal transport in such heterogeneous materials, a number of shortcomings in the approach are evident, and we therefore outline several areas for future work. Overall, the tools discussed here are sufficiently general to be useful for a broad range of applications where bridging of microstructural information to bulk properties is necessary.

Introduction

Pyrotechnic and energetic materials are well-studied examples of heterogeneous materials where small-scale variations in structure can have a drastic effect on large-scale bulk behavior. In typical applications, limited information is available on the microstructural properties of a given material, while a plethora of bulk material properties can be characterized (e.g. heat capacity, density, thermal conductivity). In many cases, different mixes of compositionally identical powders that meet the same specifications can perform quite differently.

The reasons for these discrepancies are not always clear, but given the nature of the materials, it is highly likely that material micro-structure plays a crucial role. We have therefore set out to develop a greater understanding of the connections between micro-structure and bulk properties; in this chapter we evaluate several computational tools for direct numerical simulations of thermal transport in complex microstructures.

The theoretical study of transport through heterogeneous media is an area of research with a rich history [89, 76]. Early works focused on effective medium theories [50, 8, 58, 87, 89, 76], where the goal is to derive relatively simple analytical expressions for effective properties as a function of various microstructural parameters. While these approaches continue to be highly useful in many applications, their use is often limited by assumptions regarding the nature of microstructural variations and transport physics.

With the advent of powerful computers, direct numerical simulations based on explicitly represented microstructures have gained popularity [73, 47]. In parallel, significant advances have been made in experimental techniques for three-dimensional imaging of complex microstructures, and their use is becoming increasingly widespread [28, 29, 80]. The development of software tools for generating computational models based on experimental data has also seen significant growth in recent years (e.g. Dream3D [30], SimpleWare IPScan). While significant advances toward automation of this process have been made, the quality of the resulting model is not surprisingly highly dependent on the input experimental microstructure imaging data. We have therefore explored a number of approaches for generating computational models of thermal transport for a particular pyrotechnic material.

Given that the focus of this chapter is developing and evaluating a number of computational tools, a significant emphasis is placed on descriptions of the methodology; in the section that follows, we describe the details of image segmentation, the mapping of the resulting segmented micro-structure to a spatially-varying conductivity field, and the finite element method (FEM) analysis. In the Results section, we present sample results for the effective conductivity obtained in this manner, and compare these to flash diffusivity experiments. Finally, we conclude with a summary of the methods and tools, and discuss future areas of improvement.

Methods

The experimental micro-structure data set consists of focused ion beam scanning electron microscopy (FIB-SEM) imaging of a small sample of a $KClO_4$/Ti mixture corresponding to the TKP-IP pyrotechnic material. This material was not compacted prior to FIB-SEM imaging. The data were obtained with a resolution of 38.5 $\times$ 48.8 $\times$ 40 nm per voxel in the x,y and z directions respectively, where the z-direction corresponds to the direction of FIB sectioning (i.e. normal to the plane of the images). The total 3D extent (or field of view) of the imaged region is $\sim$ 38$\times$ 34$\times$ 10 μm. Unfortunately, characteristic dimensions of $KClO_4$ particles approach the field of view dimensions, meaning that a single image stack

may not be a statistically representative sample of the material. A larger field of view can be attained, but this comes at the cost of decreased resolution, a compromise that must be made for virtually all imaging techniques. Nevertheless, for the purposes of developing and testing overall workflows, these dimensions are adequate.

Image segmentation

A sample image from the FIB-SEM image stack that we use here is shown in figure 5.1(a). Small black regions correspond to void space, large dark-gray crystalline particles are $KClO_4$ particles, and the white/light gray microporous material is the Ti phase. The full data set consists of 250 such images corresponding to different serial sections of the material, which together form an image stack that is a 3D representation of the micro-structure. The image data set is therefore a 3D array of 8-bit voxels, with each voxel having a grayscale value between 0 and 255, where 0 corresponds to black and 255 to white. The first step for any quantitative analysis of the micro-structure is to identify different spatial regions with different materials, a process we refer to as image segmentation (in some contexts, image segmentation is taken to mean the separation of an image into distinct physical features; in this case, the relevant features are simply the three material phases, but more sophisticated image segmentation would also resolve distinct particles). Ideally, one could simply threshold the grayscale values for different materials, so that a given grayscale range corresponds to a particular material. We have found this to yield poor quality segmented images, partly because of noise in the images, as well as overlapping grayscale ranges for different materials. A more sophisticated protocol was employed, as outlined next.

First, images were aligned and cropped to remove any imaging artifacts near edges, and ensure that all edges are aligned. To remove noise in the images, a bilateral filter [86] was applied to each image, which has the effect of smoothing noise in the image while minimizing any blurring of actual feature edges (see Figure 5.1(b)). Next, a two-value threshold operation was carried out, with the lower and upper threshold values set so as to isolate the $KClO_4$ phase (in Figure 5.1(c), all regions that are not deemed to be part of the $KClO_4$ phase are colored black). To remove erroneous small features, a series of 3 image erosion followed by 3 dilation operations were then carried out (Figure 5.1(d)). The process was then repeated to isolate the Ti phase (Figure 5.1(e)), and any remaining regions that were neither in the $KClO_4$ or Ti phase were assigned as void space to produce the final segmented image in Figure 5.1(f). All image processing was carried out using the open source, freely available OpenCV image processing library [7], which allows for simple Python scripting that easily automates the entire process. The only manual adjustments were the threshold values, but these only needed minor adjustments for different portions of the image stack, as the overall grayscale intensity does not vary significantly in the sectioning direction. Additional automated thresholding algorithms (e.g. Otsu's method [68]) were also explored; for cases where the overall contrast varies spatially within each image slice, adaptive thresholding schemes may be appropriate. For the present case, these more advanced thresholding algorithms were not found to be necessary. Furthermore, in the current version of the OpenCV library, both Otsu and adaptive thresholding implementations are designed strictly for binary

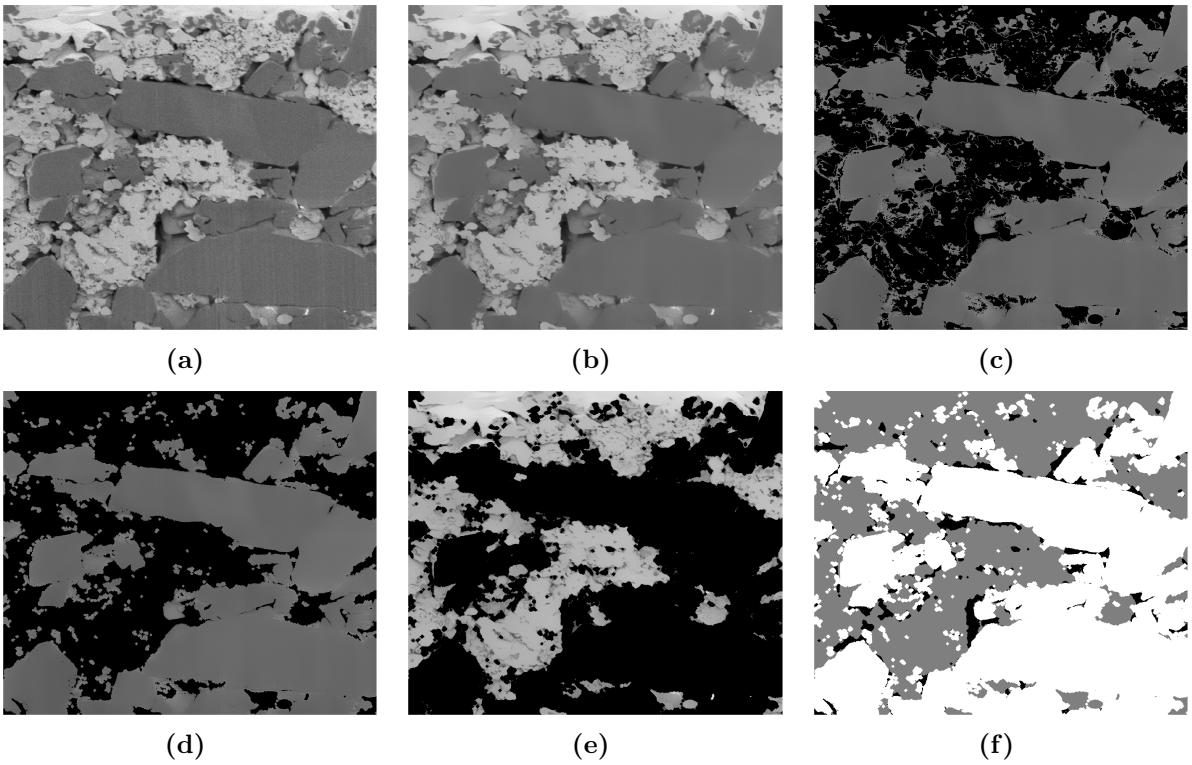

Figure 5.1. The image segmentation process. The original image (a) is treated with a bilateral filter (b), followed by a two-value thresholding operation to isolate the $KClO_4$ (dark grey) phase (c). Small features are removed by erosion and dilation operations (d), and the process is repeated for the Ti (light grey) phase (e). The final image (f) shows the three segmented phases, where black, grey and white correspond to void space, Ti and $KClO_4$, respectively. See text for additional details.

segmentation, so their use for the present three-phase segmentation case is problematic.

Generating a finite element mesh from segmented voxel data

We initially hoped to create explicit three-dimensional models of particle packs based on the FIB-SEM data discussed above. Ideally, the set of voxels corresponding to each feature (particle) could be identified from the image stack, and a 3D-surface mesh could be generated to represent each such object. The surface meshes for all objects could then be imported into a meshing software package (e.g. Cubit), and volume meshes would be generated. The advantage of this approach is that the resulting model potentially includes an explicit description of the composite material, including all particle boundaries. This would allow for more sophisticated thermal analysis (e.g. inclusion of thermal contact resistance, convection in pore space, etc.).

While a number of algorithms and tools for precisely this task have been developed [53, 30] and are well-established in fields such as biomedical imaging and modeling, automotive engineering and geophysics, their success is highly dependent on the input images. In the present case, the nature of the images (or more precisely, the particles imaged) unfortunately renders this approach infeasible. For instance, the Ti region is clearly not made up of discrete particles that can be identified as distinct image regions; on the contrary, the small-scale variations in the porous Ti micro-structure are convoluted with void regions and are not well-resolved by the FIB-SEM technique. Even the $KClO_4$ particles, which are well-imaged and have clear boundaries, cannot be readily identified as separate objects when they are in close contact. We have nonetheless attempted to carry out such image segmentations and model generation with limited sections of the image stack. Although we were not successful in creating a useful model, the expertise acquired and the development of associated workflows has already proven fruitful in other related efforts.

Instead of attempting to generate computer models with explicit geometric representations, we have adopted a much simpler approach, where only the spatial variation of material properties is captured. The basic approach involves generating a structured three-dimensional mesh corresponding to the dimensions of the image stack, then assigning spatially-varying mesh-based thermal properties corresponding to the spatial distribution of the different components in the pyrotechnic material. Since we aim to use the finite element method for thermal analysis, we use a recent technique implemented in Goma, a Sandia-developed, open source finite element code [77, 78]. We refer to this mapping procedure as voxel-to-mesh mapping. The implementation has been discussed in greater detail in a tutorial/memorandum that will be incorporated in the Goma documentation in the near future.

Thermal analysis

The voxel-to-mesh technique results in a structured mesh with an associated spatially-varying thermal conductivity $k(\mathbf{x})$ based on the input segmented voxel data set. This mesh forms the basis for the present thermal analysis calculations. The relevant governing equation for our present purposes is simply a steady-state diffusion equation with a spatially-varying diffusivity $k(\mathbf{x})$:

$$\nabla \cdot (k(\mathbf{x})\nabla T) = 0 \tag{5.0.1}$$

In all cases, a temperature difference is applied in the z-direction by setting T to 0 and 1 at opposing faces of the simulation domain (simple Dirichlet boundary conditions, where $T(z = 0) = 0$ and $T(z = L) = 1$). No-flux boundary conditions are used in the x and y directions. The spatial dimensions in equation 5.0.1 correspond to those of the FIB-SEM sample, and the conductivity is expressed in units of W/m/K. Equation 5.0.1 is solved with Goma's standard full Newton solver routines, using linear (Q1) basis functions to represent the solution. A conjugate gradient algorithm with no preconditioner is used to solve the resulting linear system.

We define an effective property of a composite material as equivalent to the conductivity of a homogeneous medium that results in the same heat flux for a given applied temperature difference and geometry. For a homogeneous material with conductivity k_{eff}, equation 5.0.1 reduces to a trivial one-dimensional case, with the heat flux q_h given by $q_h = -k_{\text{eff}}\Delta T/\Delta z$, where ΔT and Δz are the temperature difference and the size of the domain in the z dimension, respectively. From the numerical solution to equation 5.0.1, the equivalent heat flux q_{num} can be computed as the integral over the x and y dimensions at any fixed value of z:

$$q_{num} = \frac{1}{A_{xy}} \iint -k\left(\mathbf{x}\right) \frac{dT}{dz}\bigg|_{z=L} \mathrm{d}x\,\mathrm{d}y \tag{5.0.2}$$

Here, we have taken $z = L$ as the x-y plane for flux calculations, but any other value will work, provided a sideset can be adequately defined. A_{xy} is the surface area of the domain in the x-y plane.

Equating the computed flux q_{num} to the expression for the homogeneous case q_h, we obtain the following expression for the effective conductivity k_{eff}:

$$k_{\text{eff}} = \frac{q_{num}\Delta z}{\Delta T} \tag{5.0.3}$$

Results

The input to the voxel-to-mesh procedure is the full segmented three-dimensional voxel data set, prepared from the FIB-SEM data as discussed in figure 5.1 and related text. However, instead of distinct voxel intensities, each phase is assigned a conductivity value. Initially, we simply used the pure component conductivities for $KClO_4$, Ti and air; however, it is clear that the Ti-rich phase is not pure Ti, but rather a complex microporous structure with variations below the resolution of the FIB-SEM. Since we cannot resolve this structure even in terms of spatial variations of the conductivity, we use a Bruggeman effective medium approximation [8] to calculate the conductivity of the Ti-rich phase, where we assume the Ti-rich phase is simply a two-phase mixture of pure Ti and air. Its effective conductivity $k_{eff,Ti}$ is then given implicitly by:

$$\phi_{Ti}\frac{k_{Ti}-k_{\text{eff,Ti}}}{k_{Ti}+2k_{\text{eff,Ti}}}+(1-\phi_{Ti})\frac{k_{air}-k_{\text{eff,Ti}}}{k_{air}+2k_{\text{eff,Ti}}}=0 \tag{5.0.4}$$

Here, k_{Ti} and k_{air} are the pure component thermal conductivities of Ti and air, set to 21.9 and 0.025 W/m/K, respectively. Of particular importance is ϕ_{Ti}, the volume fraction of Ti in the Ti-rich phase, not to be confused with the overall volume fraction of Ti in the mixture. Since we cannot ascertain ϕ_{Ti} from the FIB-SEM images, we allow it to be a variable parameter in the thermal analysis calculations. The $KClO_4$ region is assumed to have the same thermal conductivity as $KClO_4$, set here to 0.47 W/m/K.

Figure 5.2(a) shows a three-dimensional representation of the conductivity field corresponding to $\phi_{Ti} = 1$ (equivalently, $k_{eff,Ti} = k_{Ti}$). This is to illustrate the voxel-to-mesh mapping procedure, and the spatial heterogeneity in the thermal conductivity. The resulting temperature field is shown in figure 5.2(b), where heterogeneity is again apparent. Applying the analysis discussed above to compute the effective conductivity of the sample from the finite element calculation (see equations 5.0.2 and 5.0.3), we obtain a value of $k_{\text{eff}} \approx 6.9$ W/m/K.

In figure 5.3, we plot the effective conductivity k_{eff} as a function of the size of the background mesh used for the voxel-to-mesh mapping. The mesh size refers to the size of a single element, in this case the side length of the hexahedral elements used for the background mesh. A smaller value therefore corresponds to a finer mesh. We observe no significant sensitivity of the computed k_{eff} value to the mesh size, and therefore use a mesh size of 10 voxels for all remaining calculations.

We have repeated the analysis above to obtain k_{eff} values for ϕ_{Ti} in the range 0 to 1. For each ϕ_{Ti} value, the Bruggeman effective medium approximation (equation 5.0.4) is applied to obtain the effective conductivity of the Ti-rich phase, $k_{\text{eff,Ti}}$. This is then assigned to the voxels corresponding to the Ti-rich phase (e.g. gray region in figure 5.1), and the voxel-to-mesh mapping and thermal analysis are carried out for each ϕ_{Ti} value. The resulting k_{eff} values are plotted together with experimental flash diffusivity data in figure 5.4 as a function of the percent theoretical maximum density (%TMD). The %TMD refers to the

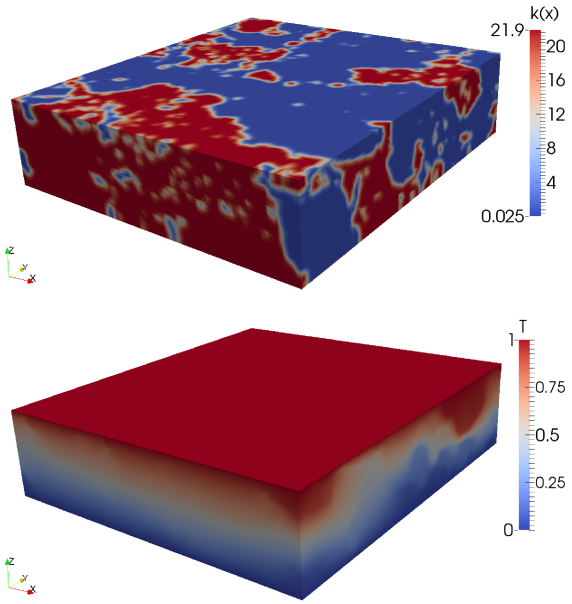

Figure 5.2. Thermal conductivity (a) and temperature field (b) in the finite element model.

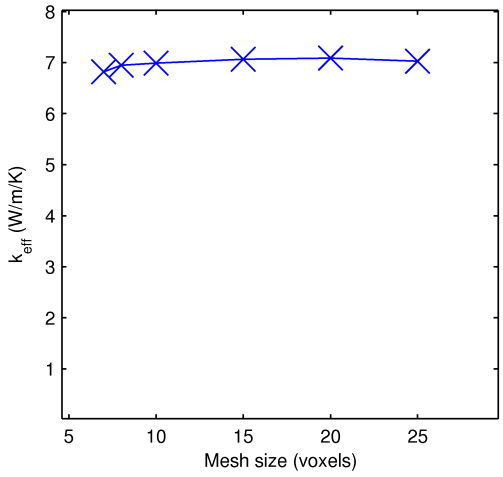

Figure 5.3. Sensitivity of computed effective conductivity to mesh size

percentage of the maximum particle packing achieved, assuming that the solid phases are incompressible and any increase in density is a result of rearranging the solid material to displace air. Corresponding ϕ_{Ti} values for the simulation data are indicated in using the top x-axis in figure 5.4; note that the %TMD value does not reach 100% even at $\phi_{Ti} = 1$, since there is additional void space outside the Ti-rich phase (see black regions in figure 5.1(f)). The sharp increase in computed k_{eff} values (as well as the Bruggeman approximation to this case) is accurate and is a result of the much higher conductivity of Ti as compared to the other components. However, it does suggest that ϕ_{Ti} values above ∼0.3 are likely not realistic for the Ti-rich phase of the FIB-SEM material.

Also plotted in figure 5.4 is a three-phase Bruggeman approximation for the TKP-IP material based on the experimentally known weight fractions of the different components and %TMD values (data labelled TKP-IP, 3-phase Bruggeman). Although the experimental data here are in a fairly limited range, the Bruggeman approximation is surprisingly successful at predicting effective conductivity values. Additionally, we have plotted the Bruggeman approximation for the FIB-SEM material, where three phases are considered: the air phase and the $KClO_4$ phases, with corresponding pure component conductivities and volume fractions as identified from the image segmentation; and the Ti-rich phase, with its conductivity $k_{\text{eff,Ti}}$ set based on the two-component Bruggeman model (equation 5.0.4), which is the same value that is input to the voxel-to-mesh mapping. At relatively low ϕ_{Ti} values, the Bruggeman approximation again tracks the simulation data surprisingly well; however, at higher ϕ_{Ti} values (> 0.5), the Bruggeman approximation fails for this case (this is more apparent in figure 5.4(a)).

The direct comparison of k_{eff} values computed based on FIB-SEM data to experimental flash diffusivity data is not straightforward. In the flash diffusivity experiments, the increase in %TMD corresponds to increased compaction of the entire sample. In the FIB-SEM material, the sample is not compacted prior to imaging, and the increase in %TMD in figure 5.4 is only due to changes in ϕ_{Ti}, the assumed volume fraction of Ti in the Ti-rich phase. Therefore, a direct comparison between experiments and simulations is only valid at low experimental %TMD values. At higher values, the simulation data presumably corresponds to a material where the %TMD value is artificially too high because of an unrealistically high ϕ_{Ti} value. For low %TMD values, the agreement in computed and measured k_{eff} values is quite good (within ∼20%), with a corresponding ϕ_{Ti} value of ∼0.3.

To check whether this is a reasonable value of ϕ_{Ti}, we can compare the known overall weight fractions of Ti and $KClO_4$ (0.33 and 0.67, respectively) to those implied by ϕ_{Ti} values for the FIB-SEM material. The latter are simple functions of ϕ_{Ti} and the volume fractions of the Ti-rich phase, $KClO_4$ and air as measured from the FIB-SEM segmented images. Figure 5.5(a) shows this comparison. The horizontal dashed lines correspond to the experimentally known values; where these intersect the solid curves is the ϕ_{Ti} value that gives the same overall mixture weight composition. The relevant ϕ_{Ti} value is ~ 0.37, somewhat higher but in reasonable agreement with $\phi_{Ti} \sim 0.3$, the value at which good agreement is obtained in k_{eff} values. We also plot the effective conductivity of the Ti-rich phase in figure 5.5(b) as a function of ϕ_{Ti}, as given by the two-phase Bruggeman approximation,

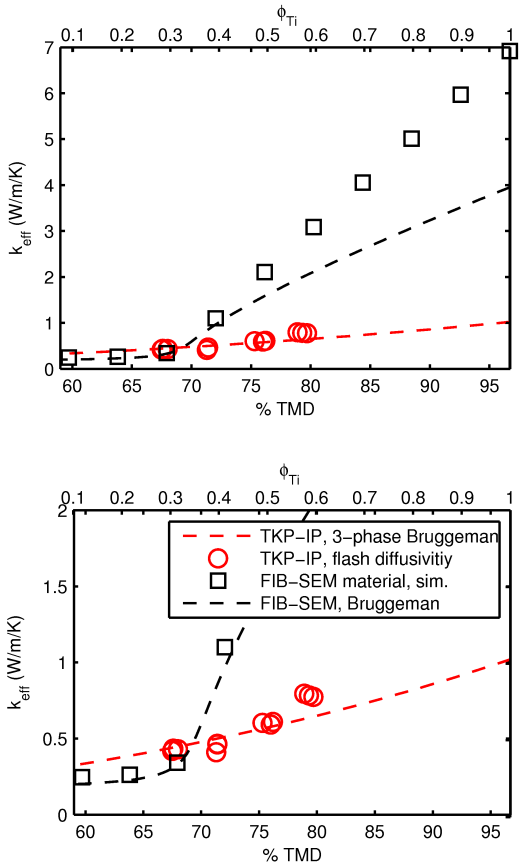

Figure 5.4. Computed and experimental effective conductivity as a function of %TMD. See text for additional details. Panel (b) is simply an enlarged portion of the low k_{eff} region in panel (a).

equation 5.0.4. In future work, measuring the conductivity of the Ti-rich component powder in isolation may be of interest and would provide validation of the Bruggeman approach for this system. Additionally, repeating the imaging and segmentation on a packing of just $KClO_4$ particles would be useful as data exist for thermal diffusivity of these materials.

Conclusions

We have applied a set of tools aimed at creating detailed models for thermal analysis of complex heterogeneous materials based directly on experimentally obtained micro-structure data. The present work represents only a cursory attempt at tackling this problem. The agreement obtained between computed and measured effective bulk conductivity values is encouraging, sufficiently so to motivate future work in this area. However, given the many approximations introduced throughout the modeling workflow, as well as the differences between the experimental system and the simulation system, this agreement may be fortuitous. Furthermore, while the computed value of the effective conductivity is reasonably close to the measured value, the level of confidence in this value is relatively low, and likely will only be useful for qualitative insights into microstructure-property relationships, rather than a reliable, quantitative value for engineering and qualification purposes. We also note that we have only briefly addressed the sensitivity of the computed values with respect to the mesh size, but a much larger parameter space needs to be addressed to ascertain the precision of the reported value (e.g. sensitivity to different thresholding/segmentation techniques; multiple FIB-SEM samples of the same material; assumptions about the pure component conductivities).

Several shortcomings have already been identified in the overall approach presented above. Perhaps the strongest is the lack of information in the model relating to interfacial transport. This has been addressed in a different context in later chapters of this report; to include explicit models of thermal contact resistance for the 3D reconstruction approach, a far more sophisticated segmentation tool is needed that can separate individual particles and solid regions with high fidelity, rather than simply distinguishing the different phases. As already discussed, this may not be feasible for the materials studied here, at least given the current limitations of the FIB-SEM technique. Additionally, obtaining detailed information about the interfacial geometry, chemistry, and the nature of inter-particle contacts is difficult, especially if a full computational reconstruction is to be attempted. More likely, such a model would be more useful if interfacial properties are treated as model variables, rather than attempting to fully discern them from micro-structure images. As such, there is significant potential to explore qualitative trends in bulk properties as a function of various interfacial properties; in turn, these surface properties could potentially be related to processing conditions (e.g. compression, particle surface characteristics, chemical modifications).

Finally, the comparison between simulations and experiments is also challenging due to the limited experimental data set. In particular, it would be of interest to repeat the analysis

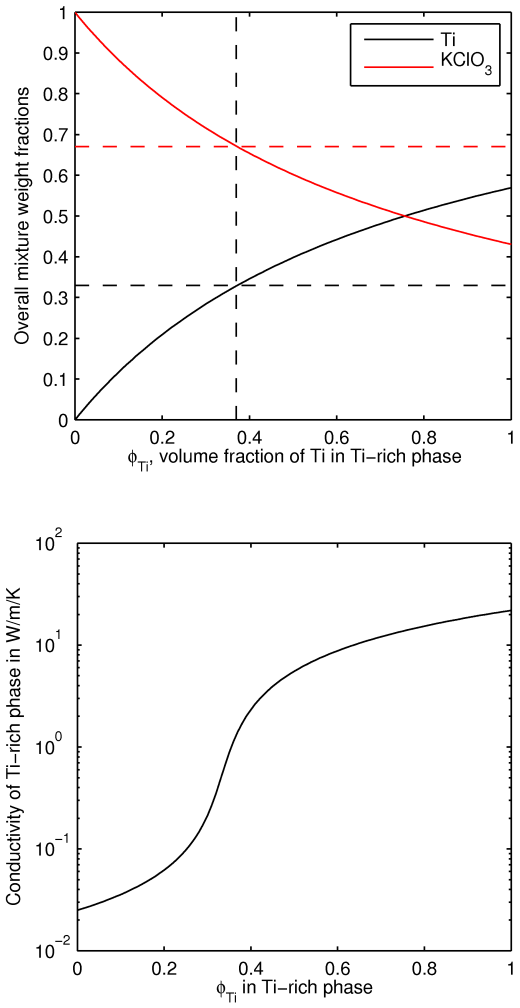

Figure 5.5. Variations in other properties as a function of ϕ_{Ti}, the assumed volume fraction of Ti in the Ti-rich phase. Panel (a) shows the overall weight fractions of Ti and $KClO_4$ in the mixture, while panel (b) shows the effective conductivity of the Ti-rich phase according to equation 5.0.4

with FIB-SEM data for various levels of compaction (larger range of %TMD values), as well as multiple FIB-SEM data sets for the same material. In addition, a significant discrepancy in length scales exists between the flash diffusivity experiments, which are carried out with samples of dimensions on the order of several millimeters, whereas FIB-SEM imaging is limited to a field of view of several tens of microns this may contribute to variability of the computation results as the representative volumes may be smaller than the macroscopic, homogeneous scale.

It is hoped that the work discussed here will form a useful basis for related work in the future. The tools and workflows employed herein - automated image processing and segmentation; voxel-to-mesh mapping; thermal analysis of complex materials - have already proven fruitful in related work at Sandia National Laboratories, and a much stronger understanding of their potential as well as limitations now exists as a result of this work.

Chapter 6

Computational Thermal Analysis in Numerically Simulated Particle Packs

In this chapter, we detail results of a stochastic simulation method newly implemented in LAMMPS for obtaining insight and data to develop coarse-grained models able to bridge scales in complex structured systems. The scales in focus here are defined by a characteristic particle size and a macroscopic, homogeneous scale. Hence, models are sought that bridge these scales, or alternatively, which are consistent on the meso-scale that is between these two scales. We point to an approach that seems capable, by capturing the relevant phenomena, of accomplishing this goal and sketch some of the initial challenges associated with such an approach.

In chapter 3 we reported results for conduction in fractal structured objects, particularly in fractal clusters taken from bond percolation networks. There it was seen that "anomalous" transport in terms of the temporal or transient scaling of thermal conduction on/through these structures was related to the spatial structure of the network. Here we describe conduction on a different random network formed by a pack of mono-sized spheres. Percolation-like behavior (in a continuum sense – i.e., the "inverse Swiss-cheese problem" [3]) is still seen as a critical packing packing fraction is approached, but the conduction on the resulting network is not anomalous (i.e., MSD $\sim$t, or Fickian) in the long time limit [26]. In fact, the non-Fickian behavior of the MSD that is observed is shown to be governed by small-scale features of the particle packing. We analyze this in terms of narrow escape or mean first passage time and show how this relates the the non-Fickian behavior of the MSD. Also, the non-Gaussian behavior of the probability distribution associated with the location of a random walker at a given time is illustrated. These two "anomalous" features of the transport related to the inhomogeneity of the structure are taken to be the main phenomena to be captured in a consistent scale-bridging modeling approach.

Random Walk in Jammed Particle Packs

We report stochastic simulations of equilibrium diffusion through packs of spherical particles in the limit of a perfectly insulating surrounding medium and vanishing bulk pressure of the particle pack. The time dependence of various diffusion properties is resolved over several

orders of magnitude. Two well-separated time regimes of normal diffusion (MSD $\sim$ t) are observed. The first corresponds to diffusion on scales smaller than individual particles, while the latter is the expected large-scale and long-time diffusion. The intermediate anomalous diffusion regime and the long-time value of the diffusion coefficient are both controlled by the contact between particles, which in turn depend on the global pressure p of the particle packs. Scaling laws are established for both the time required to recover normal diffusion (t^*) as well as the long-time diffusivity (D_∞), wherein $t^* \sim p^{-0.5}$ and $D_\infty \sim p^{0.5}$. The mean first passage time (MFPT) associated with the escape of random walkers from the particles is shown to control both t^* and D_∞ in the low pressure limit.

Diffusive transport through heterogeneous media has been a long-standing area of interest [89, 76], with wide-ranging applications in biology, geophysics and materials science. Heterogeneous media consisting of packed particles are of particular interest for industrial applications that involve powder processing routes, and transport through such particle packs can have significant implications for the resulting material properties. Much of the motivation for the present work comes from energetic and pyrotechnic material applications, where a strong understanding of thermal conduction through particle packs is an essential first step in predicting bulk material properties and ultimately product performance. In particular, we explore the relationship between the bulk particle pack pressure, which can be measured and controlled experimentally, and microstructural features that govern transport, such as the interparticle contact area, and diffusive transport over a broad range of length and time scales.

One of the greatest challenges in modeling heterogeneous media comes from the complexity of the underlying microstructure and the large separations of length and time scales that often arise. An extremely rich literature exists describing effective medium theories for predicting transport properties of heterogeneous media [50, 8, 58, 87, 89, 76], but in all cases limitations exist with regard to the nature of the underlying microstructure and range of applicability. In this work, we carry out simulations of diffusive transport using an explicit geometric representation of the microstructure. While traditional grid-based numerical methods (e.g. finite element or finite difference) have been successfully used for explicit modeling of transport [73, 47] and mechanics [59] in complex geometries, we have employed a stochastic method based on a simple random walk algorithm [88] to model diffusion in computationally generated particle packs. Due to the complexity of the microstructure and the large separation of length scales inherent to the present systems, traditional grid-based numerical methods are not feasible. Furthermore, the random walk approach allows us to quantify equilibrium (or steady-state, isothermal) transport dynamics in a way that a continuum-based approach cannot (e.g. time dependence of effective diffusivities).

We explore both disordered and ordered particle packs and compare key diffusion characteristics between them. As a canonical disordered system, we have used three-dimensional jammed packs of monodisperse spherical particles. The jamming transition is a surprisingly universal phenomenon common to disordered systems ranging from granular materials to glasses, foams, colloidal suspensions and traffic patterns, wherein a disordered fluid systems becomes rigid (or mechanically stable) at a sufficiently high density. The characterization of

the structural and mechanical properties of jammed systems has received significant interest in recent years [52, 17, 66, 79], and a number of universal scaling laws suggestive of a phase transition have been uncovered. For the present purposes, we use granular packs of frictionless, monodisperse spheres near the jamming transition as representative disordered systems. Furthermore, the global system pressure of the jammed particle packs, which approaches zero near the jamming transition point 'J', is a convenient macroscale parameter that controls the nature of the interparticle contacts. We also compare results to an ordered simple cubic lattice (SCL) system with comparable interparticle contact areas; however, in this case the interparticle contact area is a single value, whereas in the jammed configurations, a wide distribution of contact areas is characteristic of each pressure.

In all cases, we investigate diffusive transport through particle packs assuming a perfectly insulating surrounding medium, so that random walkers only move through the particle phase. The interparticle contacts therefore play a crucial role in controlling the effective diffusivity, particularly at low pressures, where the interparticle contact areas are extremely small compared to the particle size. This gives rise to two distinct diffusion domains, one governed by diffusion inside the particles, and the other by rare crossings of random walkers between neighboring particles. As the pressure is decreased, the separation in time scales for these domains diverges, and inter-particle hopping becomes the dominant, transport-limiting process. We therefore discuss the transport problem in the context of narrow escape/mean first passage time analysis [75]. In particular, a recent analysis of mean first passage time from a sphere with multiple small absorbing windows [14] provides the essential parameters and scaling laws relating transport properties to overlap areas and pressures. Although these features arise partially due to the idealized nature of the systems considered here (perfect spheres with interfaces consisting only of small overlaps; perfectly insulating medium), the notion of transport governed by a combination of bulk diffusion at the particle scale and rate-limiting interfacial transport is common to a broad range of physical situations.

Methods

Jammed particle packs were prepared as discussed in recent work by Silbert [79]. Briefly, systems consisting of N=1000 particles of diameter $d = 1$ and mass $m = 1$ were placed in a cubic simulation box with periodic boundary conditions. Interparticle interactions were modeled using a pairwise frictionless Hookean spring-dashpot force F_{hk}, which is active only when particle pairs are in contact (i.e. when the separation distance $r_{ij} < d$):

$$\mathbf{F}_{hook} = k_n \delta \mathbf{n} - 0.5m(\gamma_n \mathbf{v}_n - \gamma_t \mathbf{v}_t) \tag{6.0.1}$$

Here, k_n is the elastic constant for normal contact, δ is the overlap distance ($\delta = d - r_{ij}$), $\mathbf{n}$ denotes the unit vector along the line connecting the centers of the two particles, and $\mathbf{v}_n$ and $\mathbf{v}_t$ are the normal and tangential component of the relative particle velocity, and γ_n and γ_t are the normal and tangential viscoelastic damping constants.

For these systems, the pressure is given by the virial:

$$P = \frac{1}{3V} \sum_i \sum_{j>i} \mathbf{r}_{ij} \cdot \mathbf{F}_{ij} \tag{6.0.2}$$

Notably, this leads to the pressure scaling as $P \sim \delta$ for the Hookean force law (eq. 6.0.1) Here and in the remainder of this paper, all quantities are unitless. Equivalently, they are expressed in simulation units, where the mass unit is the particle mass m, the length unit is the particle diameter d, and a time scale is set based on the diffusion coefficient inside the particles D_0; without loss of generality, all of these quantities are set to unity.

Initially dilute configurations of particles were compressed to a volume fraction of $\phi = 0.65$, and allowed to relax to a mechanically stable state. The box size was then increased, allowing the particles to reach a new mechanical equilibrium at each step. Visualizations of the particle packs at a high and low pressure are show in figure 6.1, with particles color-coded by the volume-averaged mean first passage time (MFPT) as given by the analytical expression of Cheviakov et al [14]; this will be discussed in greater detail in subsequent sections. Of note are the significant differences in the MFPT values between the two pressures, where the low pressure, for which interfacial contact areas are extremely small, results in MFPT values several orders of magnitude larger.

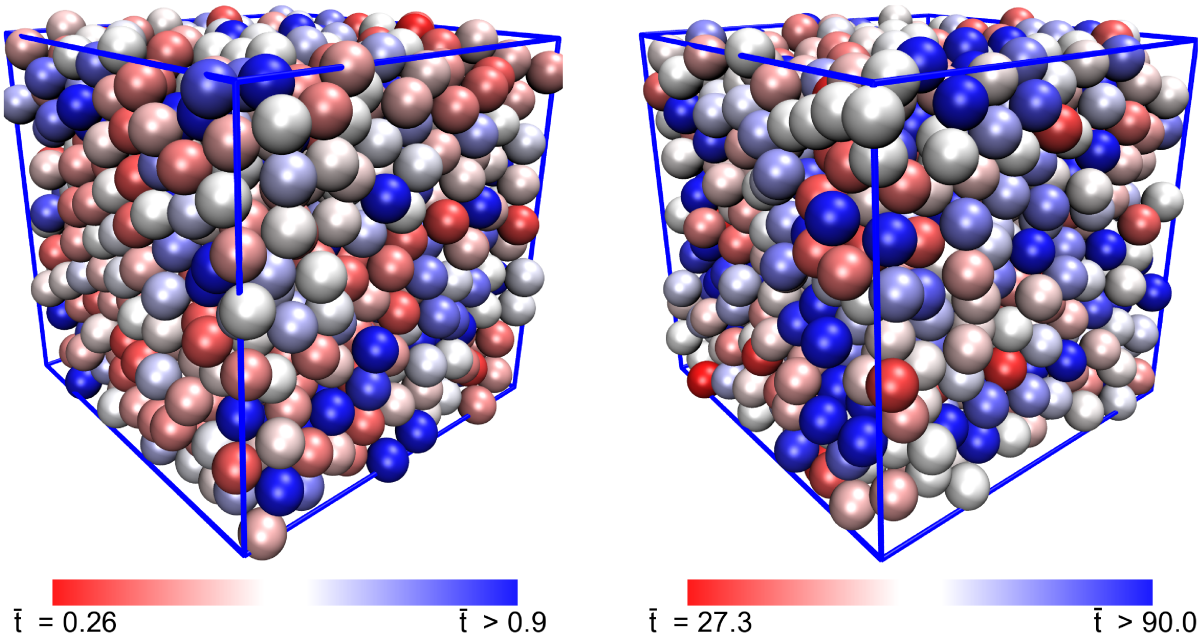

(a) p=0.004 **(b)** p=0.0000004

Figure 6.1. Jammed particle packs at low and high pressures. Particles are colored by their volume-averaged mean first passage time ($\bar{t}$). See text for more details

Prior to random walk simulations, a cluster analysis is performed on each configuration, where clusters are defined so that there is a connecting path along particle contacts among all particles within a cluster. Any particles that are in clusters other than the main percolating cluster are then removed. This is carried out to ensure that random walkers are not placed in isolated clusters that they can never escape. In practice, this results in the removal of only <20 isolated particles (so-called "rattlers") for the pressures tested.

The random walker algorithm that we have employed is closely based on the algorithm developed by Kim and Torquato [88, 44, 45], which has its roots in earlier works focused on predicting the effective conductivities of heterogeneous media [33]. The basic premise is to carry out a continuous-time, off-lattice random walk within a heterogeneous structure of interest. Within each region, the time elapsed for a random walker move is related to the conductivity in that region, and the ratio of conductivities of neighboring regions is used to determine the probability of crossing internal boundaries that separate different regions. The long-time displacement of the random walkers can then be related to the effective conductivity of the heterogeneous medium. For our present purposes, the time-dependence of various properties is also of interest. As such, a key difference in our algorithm as compared to that of Kim and Torquato is that at each integration step, the time elapsed must be the same for all walkers. This leads to slightly more complex simulation algorithm, but it simplifies the subsequent analysis of time-dependent properties. We therefore force all random walkers to have the same net displacement Δx_o (and therefore the same elapsed time) at any given integration step. The net displacement Δx_o is selected based on computational considerations, and does not affect the overall results. We have selected $\Delta x_o = 0.02d$ for all cases, where d is the diameter of the particles. An additional step size constraint Δx_i is required, as outlined below, which effectively sets the spatial resolution of the algorithm.

At the start of each simulation, a large number of random walkers are randomly placed in the interior of particles. For a given walker at the start of a step, the distance to the edge of the particle that it is currently in is computed (denote this distance Δx_p). If this distance is greater than Δx_o, the walker is translated a distance of Δx_o in a randomly chosen direction, and the time step is completed. The time associated with this move is simply $\Delta x_o^2/6D$, where D is the bulk diffusion coefficient inside the particles, which we set to unity with no loss of generality. On the other hand, if Δx_p is less than Δx_o but greater than Δx_i, the random walker is translated a distance Δx_p in a randomly chosen direction, but the time step is not completed, and its initial position is stored. The process is repeated until the total displacement of the walker is greater than Δx_o, at which point the random walker is translated backward along the last segment of its motion, such that its net displacement during the time step is exactly equal to Δx_o. This then completes the time step. If at some point $\Delta x_p < \Delta x_i$, the random walker is translated a distance of Δx_i in a random direction; if this move results in the random walker being located outside of any particle, it is reflected back into the interior of the particle by a distance Δx_i in a new random direction. As expected, the value of Δx_i can affect the measured properties, and must decrease as the particle contact size decreases (i.e. lower pressures require smaller values of Δx_i); we have therefore tested several values of Δx_i for the relevant range of pressures until acceptable convergence of the desired properties was obtained.

Results

Random, jammed particle packs

Random walk simulations were carried out for particle packs corresponding to a range of pressures spanning several decades from $p = 4 \times 10^{-7}$ to $p = 0.04$. In all cases, a million random walk steps were performed prior to sampling of diffusion properties to ensure an equilibrated distribution of the walkers, and a moving time origin approach was used for all analyses. Again, the diffusion coefficient inside the particles (D_0) was set to unity.

Figure 6.2 shows several key measures characterizing the diffusion of random walkers in jammed particle packs at several pressures. As seen from the plot of mean squared displacement (MSD) in Figure 6.2(a), the short-time diffusion behavior is Fickian (MSD $\sim t$) for all pressures. This corresponds to diffusion of random walkers inside individual particles, on time scales shorter than that at which random walkers encounter particle boundaries. At intermediate times (starting at $t \sim 10^{-1}$), there is a subdiffusive plateau, which is broader and more pronounced for lower pressures (closer to the true jammed state). At sufficiently long times, linear diffusive behavior is once again recovered for all pressures. The time required to reach the long-time linear regime increases with decreasing pressure.This time-dependent diffusion behavior can be expressed either as a time-dependent effective diffusion coefficient D, such that MSD $= D(t)t/6$, or a time-dependent exponent, so that MSD $\sim t^{\alpha(t)}/6$. The inset of Figure 6.2(a) shows plots of α for various pressures, calculated as $\alpha = d\log \text{MSD}/d\log t$. Fickian diffusion occurs at short and long times where α approaches unity. Conversely, figure 6.2(b) shows the time-dependent behavior of the effective diffusion coefficient $D(t)$.

In order to further quantify the transition between the various diffusion regimes, we define the characteristic times $t^*_{0.95}$ and $t^*_{0.99}$ such that $\alpha(t^*_{0.95}) = 0.95$ and $\alpha(t^*_{0.99}) = 0.99$ near the transition from the intermediate subdiffusive regime back to the Fickian regime. These values then represent characteristic times at which bulk Fickian diffusion is recovered. In Figure 6.3(a), we plot $t^*_{0.95}$ and $t^*_{0.99}$ as a function of pressure for the jammed particle configurations. In both cases, we note a clear scaling of $t^* \sim p^{-0.5}$, with perhaps the exception of the highest few pressures. Similarly, in Figure 6.3 (b), we plot the long-time plateau value of the diffusion coefficient (late-time values in Figure 6.2(b)) as a function of pressure, and note a clear scaling of $D_\infty \sim p^{0.5}$.

Mean first passage times

In order to understand the scaling behavior observed for t^* and D_∞, we analyze the diffusion of random walkers in the context of a narrow escape, or first passage time problem [75]. Specifically, we are interested in the first passage time associated with a random walk escaping the interior of a given particle to any of its neighboring particles. In order to do so, a random walker must reach one of the small circular contact areas that separate its starting particle from its neighboring particles. The analogous problem has been studied

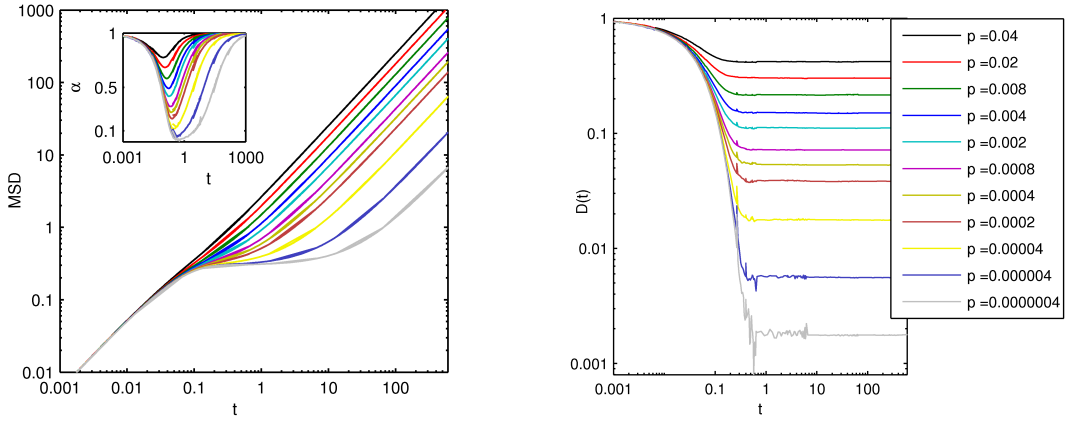

(a) Mean squared displacement **(b)** Diffusion coefficient

Figure 6.2. Diffusion characteristics of random walkers in jammed particle packs. Inset in panel (a) shows plots of the exponent α, where MSD $= Dt^{\alpha(t)}/6$.

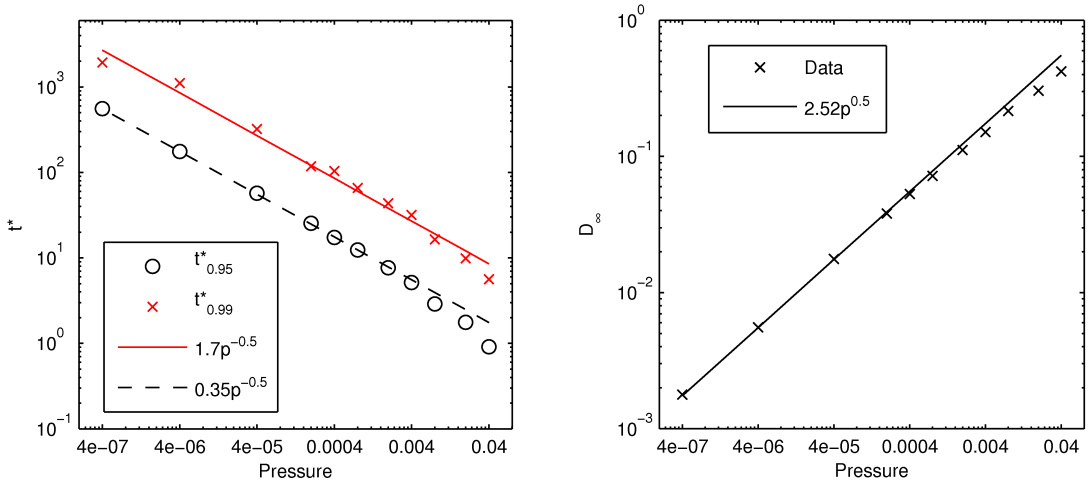

Figure 6.3. Characteristic times at which Fickian diffusion is recovered (a) and late-time value of the diffusion coefficient (b) as a function of pressure in jammed particle packs.

by Cheviakov et al [14], who derived an analytical solution for the mean first passage time MFPT($\mathbf{x}$) as a function of the starting position $\mathbf{x}$ and the size and relative orientation of small circular openings on the surface of a spherical particle. The analytical solution requires that the radius of the circular openings r_c be much smaller than the radius of the particle r [14], which is satisfied for all cases of interest here. For a given particle, we are interested in the volume-averaged MFPT, i.e. the MFPT averaged over all starting positions $\mathbf{x}$ and random walk realizations inside the particle. We refer to the volume-averaged MFPT as $\bar{t}$. This quantity was also derived by Cheviakov et al (see equation 2.44 of their work [14]). We have computed $\bar{t}$ for all particles for the $p = 4x10^{-5}$ system using the analytical expression of Cheviakov et al as well as random walk simulations. For the latter, we used a modification of the algorithm described above, where the elapsed time is allowed to be different for each random walker (i.e. no constraint is placed on the displacement at each time step). Independent simulations were carried out for all particles, where 10,000 walkers were initially placed at random locations inside each particle, and the average elapsed time for walkers to escape was computed. The results show some sensitivity to the total number of random walkers, as well as other simulation parameters, but the values thus obtained are well-converged for most particles. Figure 6.4(a) shows comparisons of the $\bar{t}$ values obtained using both the analytical expression of Cheviakov et al and direct simulation results. The agreement is strong, and we attribute small discrepancies to convergence errors in the simulation data. We therefore use the analytical expression for subsequent analysis, where $\bar{t}$ values were computed for all particles at all pressures. For each pressure, the median value of $\bar{t}$, denoted t_m, is used as a representative volume-averaged MFPT. In Figure 6.4(b), we plot t^*_{95}/t_m as a function of pressure. At all but the highest pressures, the ratio is constant, indicating that the characteristic time t^* is set by the MFPT, i.e. $t^* \sim t_m$. This shows that large-scale diffusion at low pressures is limited by the ability of random walkers to escape from a given particle to its neighbors, which in turn is governed by the interparticle contacts.

The constant value of ~ 10 to which the t^*_{95}/t_m ratio converges is not particularly instructive, since it is convoluted by the fact that t_m is a median value of the volume-averaged MFPT. Instead, we plot the mean squared displacement (MSD) of the random walkers at $t = t^*_{95}$ in the inset of figure 6.4(b). This quantity, which we denote MSD*, converges to a constant value of $\sim$6 as the pressure decreases. This can be readily interpreted as the average squared distance that a random walker must travel before its trajectory exhibits regular diffusion characteristics, i.e. MSD $\sim t$. The corresponding distance is $\sqrt{\text{MSD}^*} \sim 2.5$; in other words, in the low-pressure limit, where diffusion is dominated by rare event interparticle hopping, a walker must carry out $\sim$2-3 such hops to reach the diffusive regime.

We have established that $t^* \sim t_m$, and Figure 6.3 shows that $t^* \sim p^{-0.5}$. It therefore follows that $t_m \sim p^{-0.5}$, which can now be fully explained. First, we note that to leading order, the analytical expression for the mean first passage time $\bar{t}$ given by Cheviakov et al leads to $\bar{t} \sim r_c^{-1}$, and therefore $t_m \sim r_c^{-1}$ (in their notation, the radius of the contact region r_c is denoted as ϵ) [14]. Second, given the Hookean contact potential used in preparing the jammed particle configurations, it is easy to show that $p \sim \delta$, where δ is the overlap distance between neighboring particles ($\delta = 2r - r_{ij}$, with r_{ij} the distance between particle centers). The simple geometric relationship between r_c and δ shows that $r_c \sim \delta^{0.5}$. Finally, combining

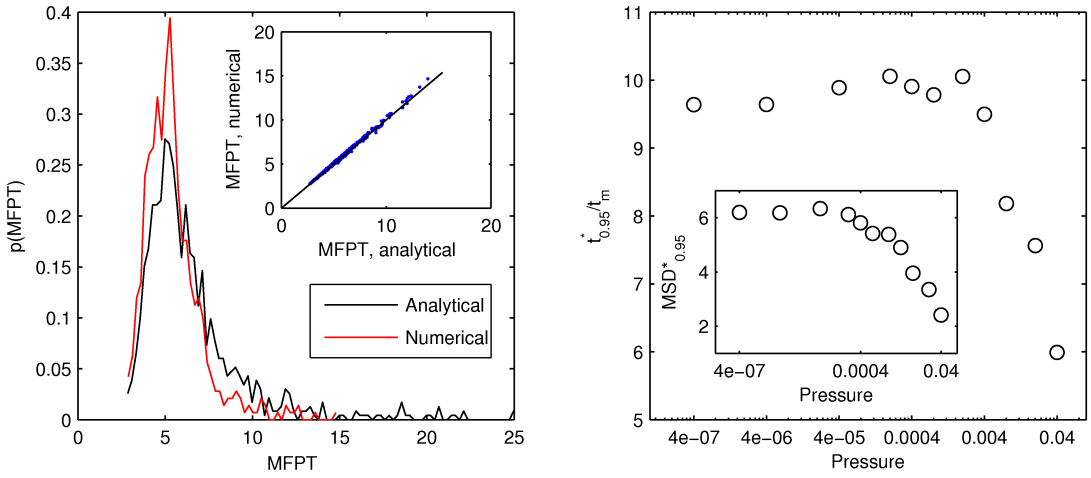

Figure 6.4. Mean first passage times. (a) Comparison of volume-averaged MFPTs computed from simulations and from the analytical expression of Cheviakov et al [14]. The main figure shows the comparison of the histograms, the inset shows the direct comparison of values for all particles, with a solid line corresponding to a slope of unity and zero intercept. (b) Relationship between t^*_{95}/t_m and MFPT for all pressures. Inset shows corresponding MSD* at $t = t^*_{95}$; see text for details.

all of these relationships, we see that $t^* \sim t_m \sim r_c^{-1} \sim \delta^{-0.5} \sim p^{-0.5}$. This explains the scaling of $t^* \sim p^{-0.5}$ observed in Figure 6.3(a).

The scaling behavior of the long-time effective diffusion coefficient D_∞ can also be readily explained by a similar argument. In the long-time limit, normal diffusion is recovered, such that MSD $\sim t$. For any t^* value selected so that α is arbitrarily close to unity, the corresponding MSD* will be constant at lower pressures (see inset of Figure 6.4(b) for $t^*_{0.95}$, which was defined such that $\alpha(t^*_{0.95}) = 0.95$). The long-time diffusion coefficient in this case is then simply $D_\infty = \text{MSD}^*/6t^*$, and so $D_\infty \sim 1/t^*$. Since we have established that $t^* \sim p^{-0.5}$, it then follows that $D_\infty \sim p^{0.5}$, the scaling behavior noted in Figure 6.3(b).

Comparison to simple cubic lattice

Since nearest-neighbor inter-particle contacts appear to control the large-scale transport properties in the particle packs considered here, it stands to reason that the behavior noted thus far is not unique to the jammed configurations discussed thus far. We have therefore repeated the analysis above for an arrangement of particles in a simple cubic lattice (SCL). SCL systems are constructed such that the system pressure is equal to that of the jammed particle packs, using the same Hookean contact potential. In the jammed configurations at the lowest pressures, the average coordination number approaches a value of six, which is the coordination number of the SCL systems. However, an important difference between the two cases is that the size of the contacts and therefore the MFPT are single values in SCL systems, as compared to the distributions noted for jammed packs. As expected, the same average diffusion behavior presented above for jammed configurations is observed in SCL systems, with two distinct Fickian diffusion time scales separated by a sub-diffusive intermediate domain. We extract t^*_{95} and D_∞ values for the SCL systems, and plot them together with those previously shown for jammed systems in Figure 6.5. The match is nearly quantitative, but more importantly, the same scaling behaviors are observed, where $t^*_{0.95} \sim p^{-0.5}$ and $D_\infty \sim p^{0.5}$. This is not surprising, since we have shown that this scaling can be fully explained in the context of a first passage problem and several simple geometric arguments, all of which are equally valid in SCL systems.

Summary

We have presented random walk simulations of diffusive transport in disordered particle packs near the jamming transition. Two distinct linear diffusive regimes where MSD $\sim t$ are observed at short and long time scales, separated by an intermediate subdiffusive regime. The first regime corresponds to regular diffusion in the interior of particles, while the second regime is the expected long-time bulk diffusion behavior. The time scale separation between the two regimes grows as the pressure decreases. This is caused by the corresponding decrease in the size of interparticle contacts, which leads to the average diffusion behavior being controlled by the ability of random walkers to escape from one particle to neighboring

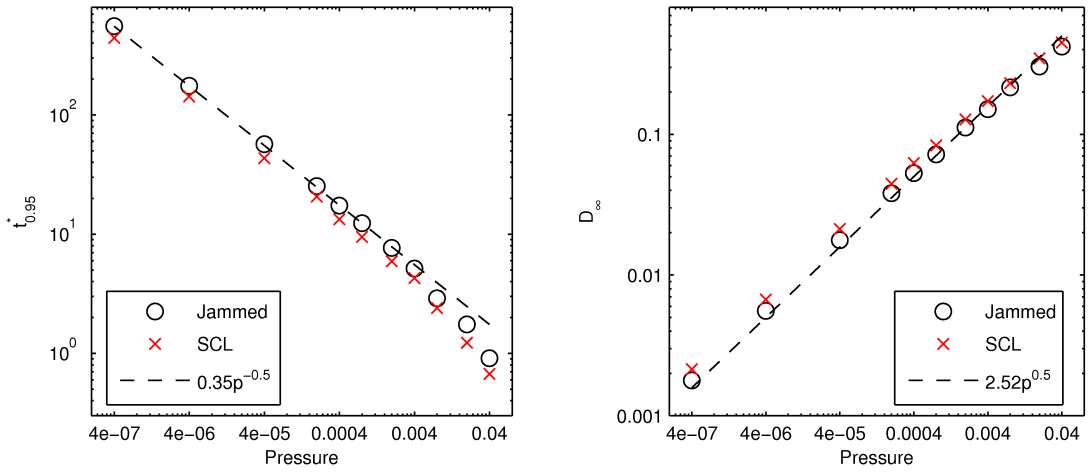

Figure 6.5. Key scaling behaviors in simple cubic lattice particle arrangements as compared to jammed systems.

coordinated particles. We have analyzed this behavior in the context of a mean first passage time problem, and have fully explained the $t^*_{0.95} \sim p^{-0.5}$ and $D_\infty \sim p^{0.5}$ scaling observed, where $t^*_{0.95}$ is the characteristic time at which linear diffusion is recovered and D_∞ is the long-time effective bulk diffusion coefficient. The multi-scale nature of the diffusive behavior as well as the scaling exponents are common to other particle arrangements, such as a simple cubic lattice, so long as the interparticle contact overlap distances are much smaller than the particle characteristic size. Overall, this work provides detailed insights into transport through particulate media, where interfacial effects are likely to be dominant. Interfacial models are the subject of the following chapter, but before that, the question of scale-bridging models is addressed.

Further Model Development

Brownian motion can serve as a reasonable description of multi-scale heat conduction by phonons [63, 94] and, of course, random walks are the stochastic process that underlies the Heat Equation, the basic thermal transport process. However, classical random walk processes in homogeneous, isotropic media are independent of the scale on which the process is resolved, $MSD \sim t$ for any Δx or Δt. Here (recall Figure 6.2(a)), the diffusion of walkers is not scale independent, in fact by effectively dividing-up an homogeneous, isotropic material into slightly overlapping, equal-sized spherical chunks we have introduced a time scale (related to the ratio of the size of the spheres, d, to the amount of overlap, δ) – a mean time for a walker to escape a spherical region. Hence, in this inhomogeneous material scale matters. Either we must resolve the geometric structure of the particle pack, including the spherical clumps of materials as well as the details of their mutual contact and solve for transport on

this "quenched" random structure, which was accomplished above, or, assuming an isotropic packing of spheres, we can average over the random microstructure leading to an "annealed" description that captures the relevant scale dependence. The main task of this subsection is to further demonstrate that the latter type of models can be applied to conduction (thermal/electrical) in particle packs with the potential of resolving and bridging scales (here, from sub-particle through particle-particle microstructure to homogeneous macro-scale). In particular, in this subsection a certain so-called Continuous Time Random Walk model is shown to capture (semi-quantitatively) the relevant scale dependent phenomena.

There are two main aspects of the phenomenology of "anomalous" and scale dependent transport that we must address: (i) Non-Fickian (often subdiffusive) behavior at intermediate times (not just in the asymptotic long time limit); and (ii) non-Gaussian probability distribution of location of walkers at a given time. Simple random walk processes on certain structures (e.g., so-called blind and myopic ant random walks on fractal percolation clusters) lead to anomalous long time/asymptotic or macro scaling of MSD with t (see [26, 6]). Here, we must account for subdiffusive behavior at intermediate times related to the scale dependent or multi-scale nature of transport in these particle packs. Non-Fickian behavior is best demonstrated plotting the exponent on time in the MSD $\sim t^{\alpha(t)}$ relationship, where $\alpha \neq 1$ indicates non-Fickian. This is done in 6.6. In addition, recent work has highlighted the non-Gaussian of the more fundamental jump distribution both experimentally as well as through numerical simulations (see [92, 13]), showing it to be a general feature of scale dependent relaxation phenomena in complex disordered materials.

A modeling framework to capture this behavior can be found in so-called Continuous-Time Random Walks (CRTW) and Generalized Master Equations (GME). Examples of this approach for disordered or heterogeneous materials can be found in (i) Klafter and Silbey [46] who derive the Generalized Master Equation from ensemble averaging over microstructures the master equation defined on a particular realization (for more on the relationship between GME and CTRW see [43]); (ii) Sahimi [76] who develops an Effective Medium approach, which also is a type of homogenization of structure (i.e., replace inhomogeneous, position dependent diffusion constant with a transitionally invariant) and leads to memory (i.e., time dependence in the material properties); and (iii) Chaudhuri et al. [13], who as alluded to above, claim a "universal" phenomenology for mass transport in dense random particle-based systems – random exploration of local cage and random jumps between cages leading to dynamical heterogeneity (i.e., "particles that are substantially faster or slower than the average").

As the name suggests, the MSD is a second moment of the distribution of displacements in the system and therefore characterizes just an aspect of the probability distribution of the location of walkers. If this distribution is Gaussian, then the first and second moments are sufficient to fully characterize it as the rest of the moments can be related to them. As noted above, non-Fickian behavior of the second moment is often related to a non-Gaussian nature of the underlying distribution [13, 92, 93]. This is indeed the case here as can be seen in figure 6.7.

Plotted in Figure 6.7 are the jump distributions for the random walkers in the particle

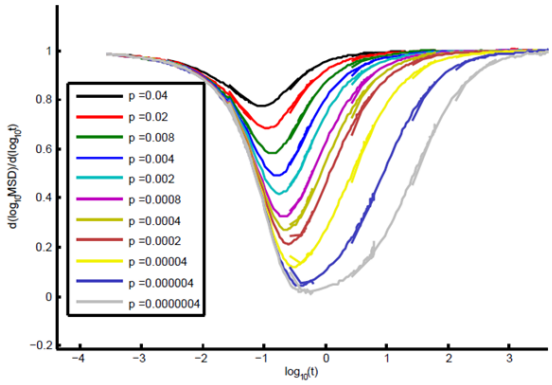

Figure 6.6. non-Fickian parameter $\beta(t)$ (MSD $\sim t^{\beta(t)}$) for various pressures.

pack created with a pressure $p = 0.0004$. The different colors of the data are for different times and are grouped into four classes for ease of comparison and to highlight certain qualitative features of the evolution. For each walker the displacement from its starting position is calculated at a given time and all walkers, regardless of where they start, are used to determine the probability of a given displacement as plotted in the figure. This is effectively an ensemble averaged approach where it is implicitly assumed that grouping the random walker data over the simulation volume is representative of the entire ensemble of possible configurations that the random walkers might see. As can be seen in Figure 6.7(a), the early-time evolution of the displacement distribution follows a Gaussian-like profile corresponding to conduction in the homogeneous, isotropic material that makes up the particles. However, by the end of the time segment represented by the early-time data, the spread of the walkers is starting to slow relative to the spread in a homogeneous, isotropic media. This is an indication that the walkers are interacting with the reflecting boundaries of the particles and are thereby constrained on average. For the second segment of time represented by the data in Figure 6.7(b) (dubbed "early-intermediate"), a shoulder can be seen to develop in the jump distributions that travels up as time progresses. By late-intermediate times, as shown in Figure 6.7(c), the tails of the distributions below the shoulder can be seen to stretch out into an exponential form, indicating a broad range of walkers motions, while the inner "core" of the distribution remains Gaussian in shape. Finally, as time progress to the late stage the shoulder disappears and the tails, indeed the entire distribution, begins to recover a more-or-less Gaussian shape, but with a width that spreads according to a different value than that which characterized the early-time spread in the homogeneous, isotropic material making up the particles. This phenomenology is generic to all of the relatively low pressure systems (cf. Figure 6.9) where walkers are confined relative to a homogeneous, isotropic media and represents the process by which the transition from transport on the sub-particle scale through the particle-particle mesoscale to the bulk homogenized scale.

As noted, the distributions in Figure 6.7 clearly deviate from Gaussian form during intermediate times. To quantify this deviation, the normalized excess kurtosis is commonly

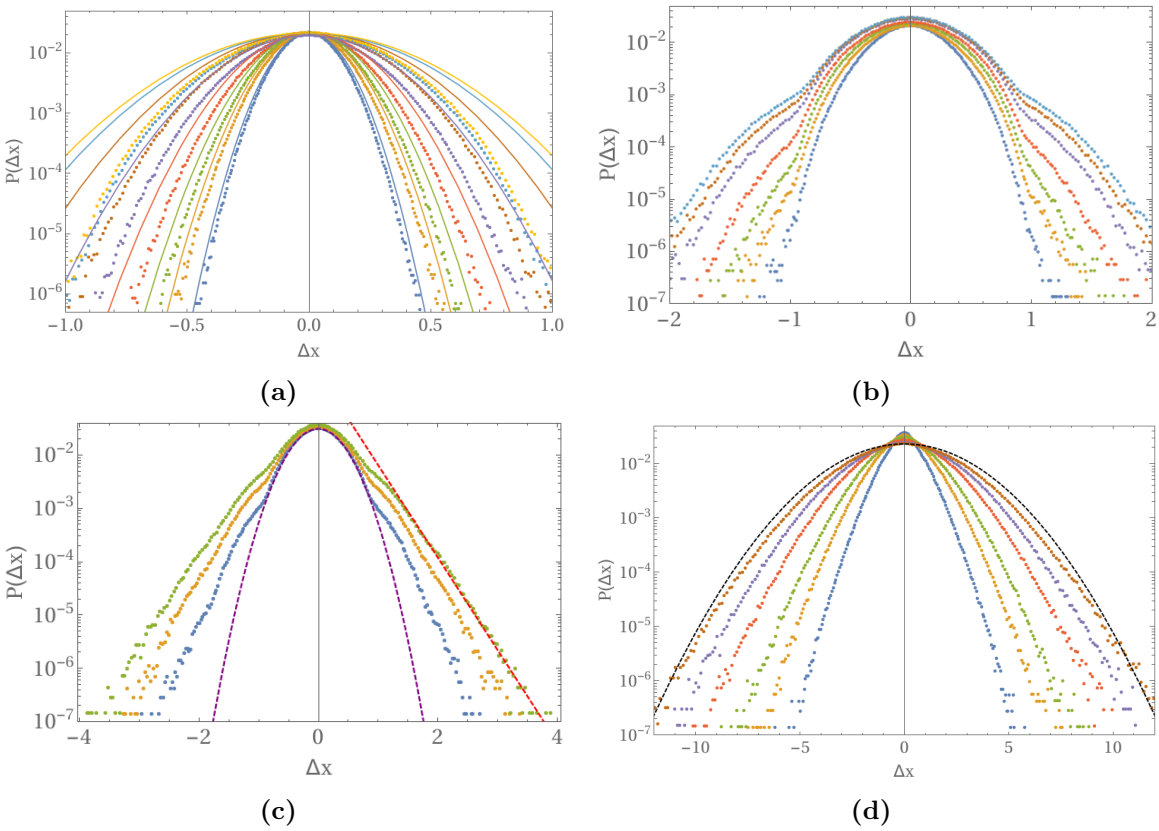

Figure 6.7. Jump distributions for walkers in jammed particle pack prepared at $p = 0.0004$. (a) Early-time jump distributions where effect of sphere boundaries can be seen. Solid lines show Gaussian spread of walkers in homogeneous, isotropic materials with diffusion coefficient D_0, random walkers in particle pack spread relatively slower; (b) early-intermediate time showing development of "shoulder" in jump distribution; (c) late-intermediate time showing Gaussian inner region (dashed lined) and development of exponential tail (dotted line) in jump distributions; (d) Late-time jump distributions showing return to nearly Gaussian distribution of walkers (dashed line).

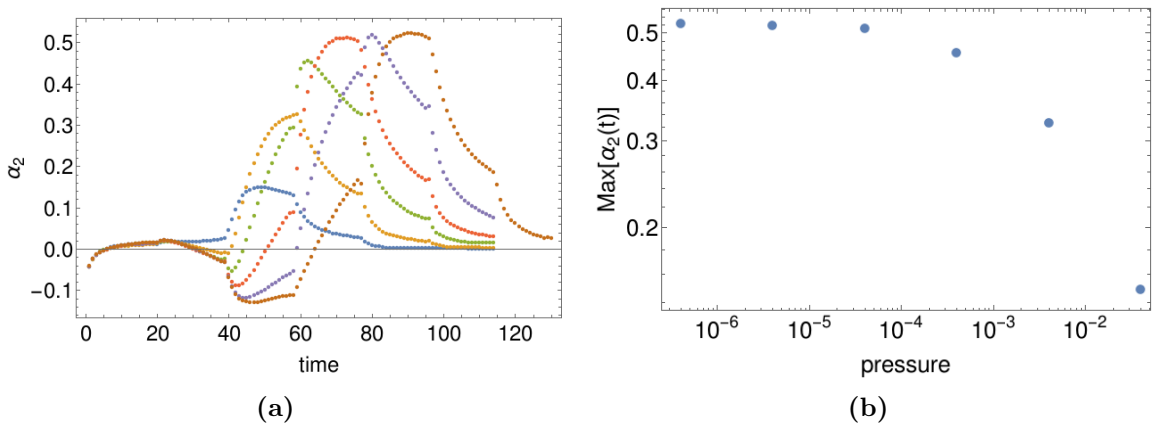

Figure 6.8. Non-Gaussian parameter for packs at various pressures: (a) normalized excess kurtosis; (b) maximum normalized excess kurtosis as a function of pressure.

used. As the odd moments of a symmetric distribution are zero, the ratio of the fourth and square of the second, called the kurtosis, is a convenient metric for determining the form of a distribution relative to a Gaussian, which has gives a well know value of this ratio. The excess, relative to a Gaussian distribution, normalized, by the Gaussian value, kurtosis is given by

$$\alpha_2(t) = \frac{\langle \Delta x(t)^4 \rangle}{3 \langle \Delta x(t)^2 \rangle^2} - 1 \tag{6.0.3}$$

This is plotted in Figure 6.8(a) for walker displacement distribution in packs generated at various pressures. For a given pressure, the variation of this parameter follows the qualitative features of the jump distributions noted above: (i) initially the distribution is zero indicating a Gaussian shape; (ii) this is followed by a negative deviation indicating a decrease in the strength of the tails of the distribution relative to Gaussian – walker confinement effects; (iii) then comes an increasing and decreasing positive deviation from Gaussian, or stretching of the tails; (iv) finally a Gaussian-like normalized excess kurtosis is recovered. It is also interesting to note that as the pressure decreases, the maximum deviation from Gaussian increases until it saturates for the lowest pressures, see Figure 6.8(b).

These two features, non-Fickian dependence of the MSD on time and, more generally, the non-Gaussian shape of the jump distribution form the base-line phenomena that must be model in an effective, homogenized material if the scale-dependence is to be captured. As noted in the introduction to this subsection, these are basic features of so-called Continuous-Time Random walks and Generalized Master Equations. This can be seen in Figure **??** where half (for clarity) of the jump distributions from the $p = 0.00004$ case in Figure 6.9 are compared with those calculated from the CTRW model given in [13].

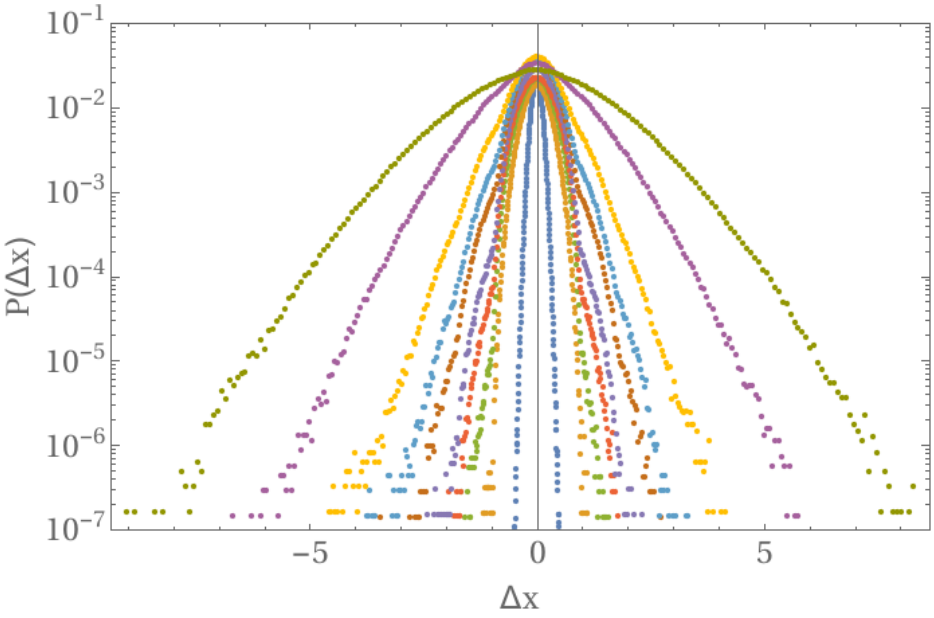

Figure 6.9. Jump distribution for $p = 0.00004$.

The model of [13] is developed for a very different system: glasses and jammed particulate systems. However, the phenomena on which it is based, so-called dynamical heterogeneity – an over-population of particles much faster and/or slower than the average – seems very prevalent when dealing with transport in random, complex materials. In fact, their model is built from a generalization of random walks known as continuous-time random walk (CTRW). It is this modeling framework that is of interest to explore and exploit for application to more general transport (thermal, electrical, momentum) in complex materials. To this end, first note that the model of [13] captures the relative qualitative features as already discussed above (see Figure **??**); viz. the inner Gaussian core, shoulder in the jump distribution, and the exponential stretching of the tail. This is done by convoluting two basic random walk process – Gaussian exploration of local environment and Gaussian hopping between local environments. Initially, this sounds very similar to what might be expected here where a walker explores its local particle until it "hops" into a neighboring particle. However, one discrepancy can be seen at early times in Figure **??** where the shoulder in the jump distribution appears too early for the model as compared with the numerical data (details of the model and parameters used are given below). Nonetheless, from this qualitative comparison, one can become emboldened to attempt to fit this same model to the jump distribution data at hand. This is done following a similar procedure to that out lined in [13]. Following, then, [13] the equation for what has been called here the jump distribution can be written in Fourier-Laplace space as

$$P(q,s) = f_{vib}(q)\Phi_1(s) + f(q)f_{vib}(q)\frac{\phi_1(s)\Phi_2(s)}{s(1-\phi_2(s)f(q))} \tag{6.0.4}$$

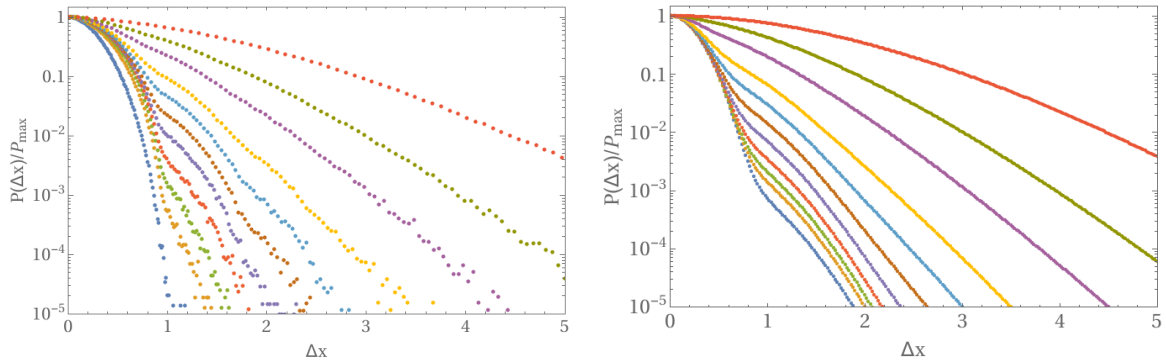

Figure 6.10. Compare data with model. This uses all four parameters following Chaudhuri et al. $l_1 = d$, $l_2 = r$, $\tau_1 =$, and $\tau_2 =$

where $\phi_{1,2} = 1 - s\Phi_{1,2}$, $f(q) = f_{vib}(q)f_{jump}(q)$, $f_{vib} = (2\pi\ell^2)^{-3/2}\exp(-r^2/2\ell^2)$, $f_{jump} = (2\pi d^2)^{-3/2}\exp(-r^2/2d^2)$, $\phi_1 = \tau_1^{-1}\exp(-t/\tau_1)$, and $\phi_2 = \tau_2^{-1}\exp(-t/\tau_2)$. Again, these functional forms represent a very simple model which aims to capture two simple features: (i) random walk (i.e., diffusive) exploration of the local environment; and (ii) diffusive exploration of the global structure through a random walk between local environments. One main difference for the structures here is that they are static and do no relax or diffuse in contrast to what might be expected in glassy structures. In any case the, it was found in [13] that for a number of systems the two length scales in the distribution of hops, ℓ and d, were proportional to each other, $d \approx 2\ell$. Again, this seems to make sense here if we take $\ell = R$, where R is the radius of the particle and $d = D = 1.0$ where D is the particle diameter. Now the walker explores the local environment of its initial particle characterized by a length R and then "hops" between local environments separated by distances $\sim D$. As for the two time scales in equation 6.0.4, the simplest approach is to set them equal to each other $\tau_1 = \tau_2 = 1.0$. These are parameter values for the results in Figure **??**(b). Again, the right qualitative features are present except for the earliest times where the shoulder appears too early in the model. In Figure **??**a, a more direct comparison of the model and simulation data for intermediate to late times is made. Here it can be seen that the inner Gaussian core is slightly narrower than the data; although decent semi-quantitative agreement is still found otherwise. This agreement can be improved by a slight simplification of the model.

In equation 6.0.4 when $\tau_1 = \tau_2$ a simplification results

$$P(q,s) = f_{vib}(q)\left(\frac{1-\phi_2(s)}{s(1-\phi_2(s)f(q))}\right) \tag{6.0.5}$$

If instead of the convolution of the vibration and jump step distribution, $f(q) = f_{vib}(q)f_{jump}(q)$, in the denominator we take $f(q) = f_{jump}(q)$ only, then, with the same values for the param-

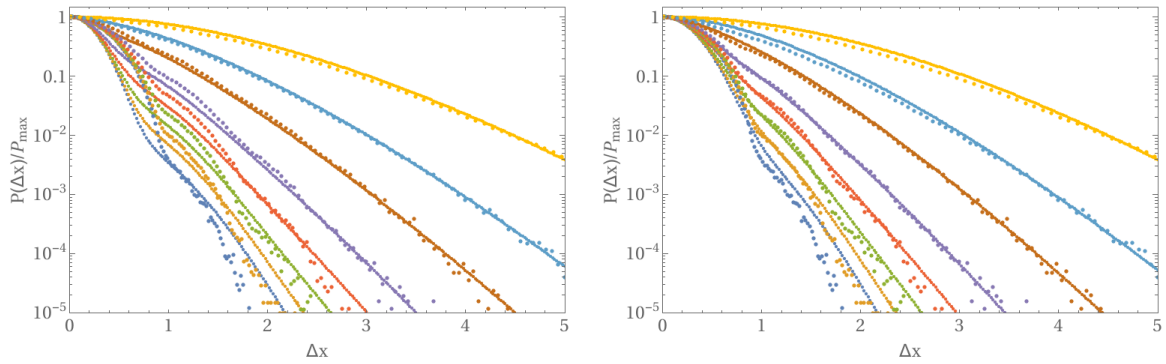

Figure 6.11. Compare model with model. (a) version 1 of model – all four parameters; (b) version 2 of the model – three parameters/Montoll-Wiess CTRW with Gaussian initial condition.

eters as above, the model fits the data even better. This can be seen in Figure 6.10(b). In this case, good quantitative agreement is seen for most of the intermediate to late time data. The change is subtle, and reflects the fact that this particular model doesn't quite capture the short-time exploration of the constrained environment well. In fact, Equation 6.0.4 is a standard CTRW formulation of the classical random walk process, which is due to Montroll and Wiess [62], but with an initial distribution of walkers given by f_{vib}.

Clearly, more work is required to resolve the details here, and the simulations certainly provide the data necessary for this type of detailed analysis; however, to this point the results are encouraging. Reasonable semi-quantitative agreement is found, particularly for intermediate to late times. This suggest that further work based on modeling multi-scale materials via CTRW or, equivalently [43] Generalized Master Equations would be fruitful.

Chapter 7

Time Domain Thermoreflectance (TDTR) Thermal Conductivity and Interface Conductance Measurements

Here we begin to address the issue of transport at the interfacial scale. Up to this point, little has been stated, but much has been assumed about the nature of transport across material interfaces. Most of the aforementioned modeling has assumed "ideal" contact between particles while in the actual phyrotechnic material two very different materials can come into contact. Hence, this Chapter discusses thermal conductivity and interfacial conductance measurements that were performed using the time domain thermoreflectance (TDTR) technique. The TDTR method is briefly introduced and the SNL TDTR capability described. The experimental samples for the measurements in this report consisted of ammonium perchlorate (AP) crystals coated with aluminum. AP is used as a stand in for potassium perchlorate as samples of single crystals were readily available and did not require growing from scratch. The results of the TDTR measurements are presented and discussed. To the best of the author's knowledge, these are the first thermal boundary conductance measurements for an aluminum-ammonium perchlorate interface measured using TDTR.

TDTR Technique

Time domain thermoreflectance (TDTR) is an optical experimental technique in which ultrashort-pulse lasers are used in a pump-probe configuration [10, 11, 34, 35, 9, 95]. A pump-probe thermoreflectance experiment allows the sample to be excited or heated by the pump pulse and the change in the sample reflectance detected by the probe pulse. A schematic of a typical TDTR experiment is shown in Figure 7.1, and a picture of the TDTR experiment in Building 897/Room 2424 is in Figure 7.2. This LDRD supported reconstituting the TDTR capability at Sandia National Laboratories in Albuquerque after a previous TDTR experiment [35] was taken apart due to staff leaving and a facility move.

In the SNL TDTR experiment [34, 35], a Ti:Sapphire femtosecond laser pulse is split into two optical paths: a pump and a probe path. The pump path is directed through an electro-optic modulator that modulates the pump beam at a frequency f and then a bismuth triborate (BiBO) crystal to frequency double the pump laser light. Thus, 800 nm

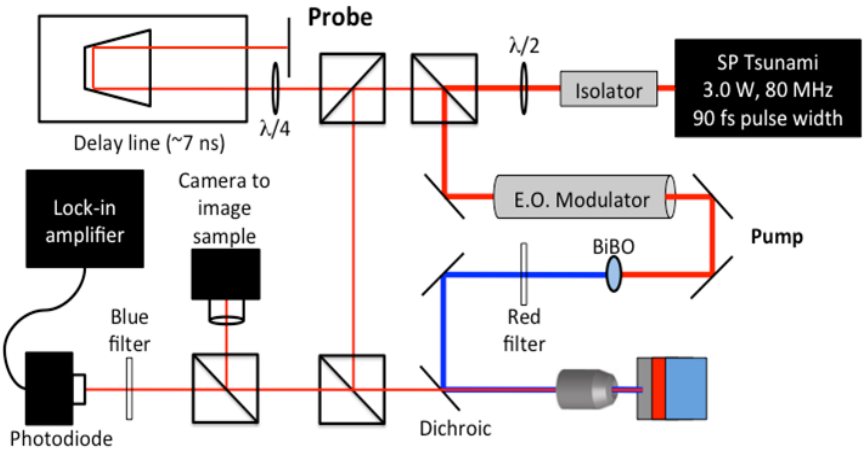

Figure 7.1. Schematic for the time domain thermoreflectance (TDTR) experiment.

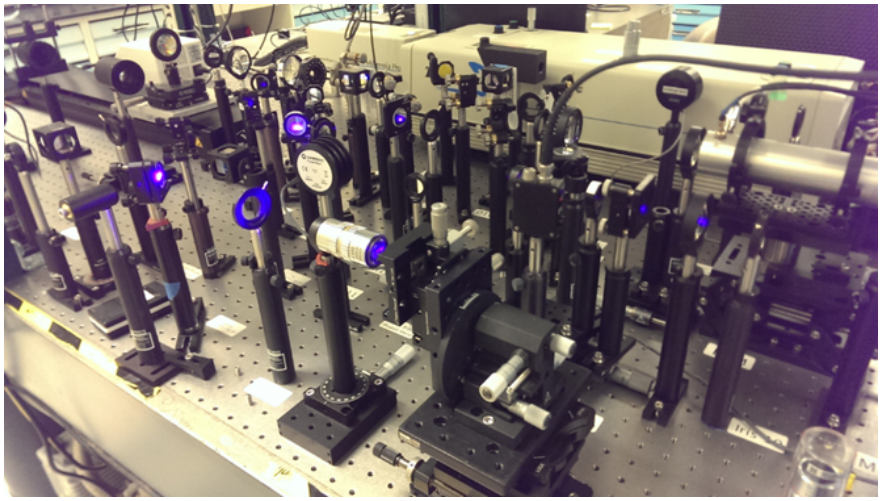

Figure 7.2. Picture of the TDTR experiment in Building 897/Room 2424.

Ti:Sapphire laser pulses are converted into 400 nm pulses. The pump laser pulses are then directed through a microscope objective and focused on the sample. The 800 nm laser energy directed down the probe optical path is sent down a mechanical delay stage and then focused collinearly with the pump laser light onto the sample with the probe laser spot radius being smaller than the pump laser spot radius to maintain one-dimensional heat transfer in the sample perpendicular to the sample surface and reduce error due to probe laser spot movement. The reflected probe laser beam is reflected from the sample back through the objective, polarizing, and filtering optics onto a photodiode. The voltage signal from the photodiode contains both a DC signal and a small AC signal representing the change in the probe beam reflectivity due to pump beam heating at frequency *f*. A lock-in amplifier is used to detect the small AC signal from the probe beam, and the in-phase and out-of-phase components of the AC signal are monitored as a function of the delay between the pump and probe beams created by the delay stage. After the initial increase due to the sample heating from the pump pulse, the ratio of the in-phase to the out-of-phase voltage from the probe pulse decays as a function of time. By fitting the decay curve, the thermal conductivity and thermal boundary conductance for the sample can be determined.

Aluminum Coated Ammonium Perchlorate Samples

A smooth reflective surface is required for adequate signal-to-noise ratios for TDTR measurements. Pressed powder pyrotechnics do not have smooth enough surfaces to be coated with a metal film and have reflective enough surfaces for TDTR measurements. Thus, crystals of representative materials were sought. While potassium perchlorate crystals were not available, aluminum perchlorate (AP) crystals of sufficient size were obtainable. AP pieces 1-3 mm in size were cleaved from parent crystals that were approximately 1 cm^3 in size. The parent crystals were slow grown and had no visible inclusions. The AP pieces were adhered to a glass substrate and then coated with aluminum. Aluminum is a standard transducer material for TDTR, and the change in its reflectance with temperature is known [91]. Typically, an aluminum film of around 100 nm is deposited. Since the thickness of the metal transducer is a key parameter in TDTR analyses, Al was also deposited on a substrate without an AP crystal to use to confirm the Al film thickness. Images of the two AP samples are shown in Figures 7.3 and 7.4 prior to and after Al coating. As observed in these images, the surface for sample A is smoother and less terraced than that for sample B.

Experimental Data Analysis and Results

The two aluminum coated perchlorate samples were inserted into the TDTR experiment and irradiated after the witness sample was used to verify the aluminum film thickness of 117 nm. This film thickness is also consistent with the echoes seen in the TDTR signal. Figure 7.5 shows the decay of the in-phase to out-of-phase TDTR signal for sample A. There are four scans on Figure 7.5 with two of them being at the same location and two more being at other locations on the sample. The scans are very consistent and have echoes spaced at

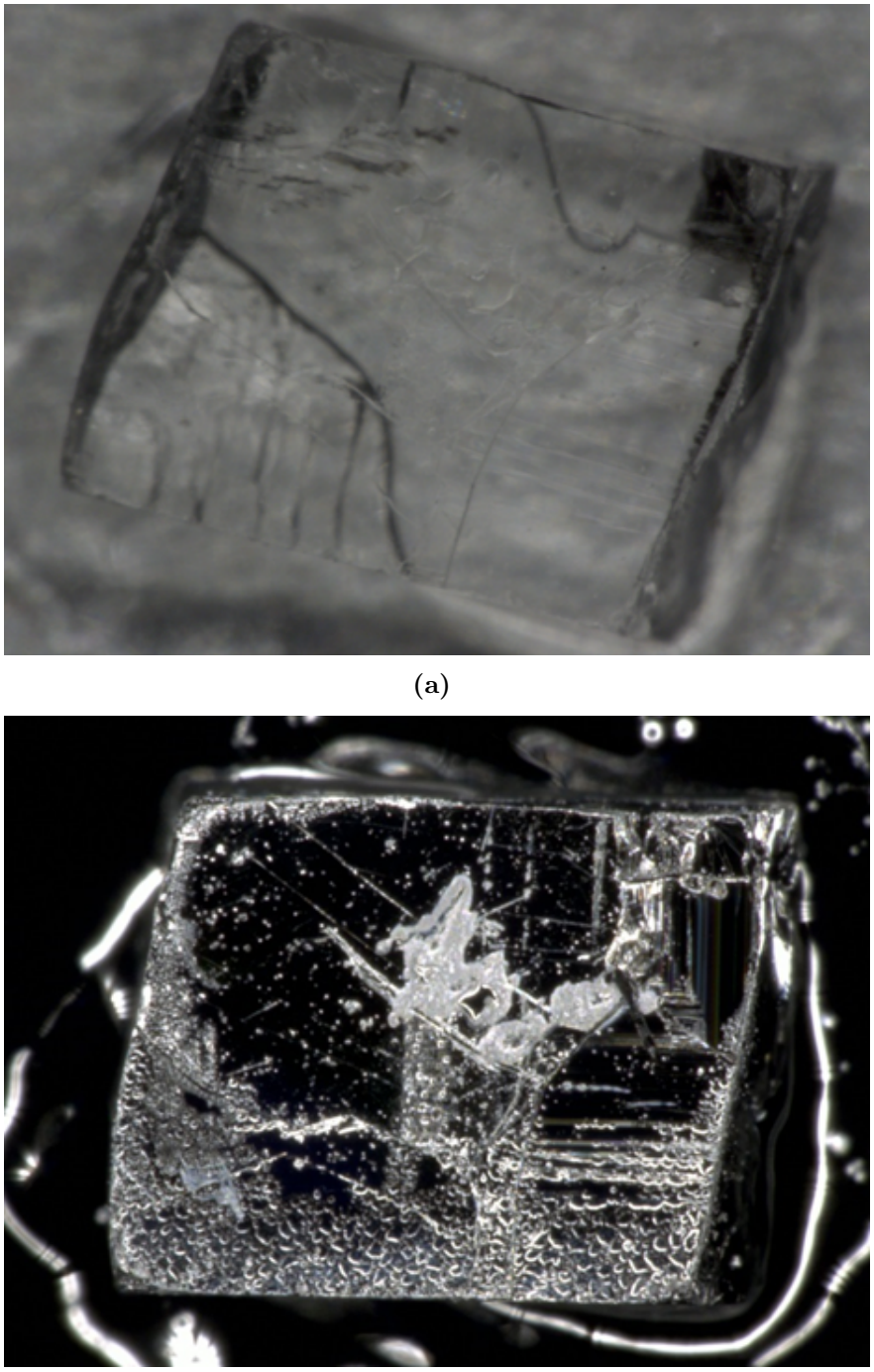

(a)

(b)

Figure 7.3. Microscope images of sample A: (a) prior to and (b) after aluminum coating deposition.

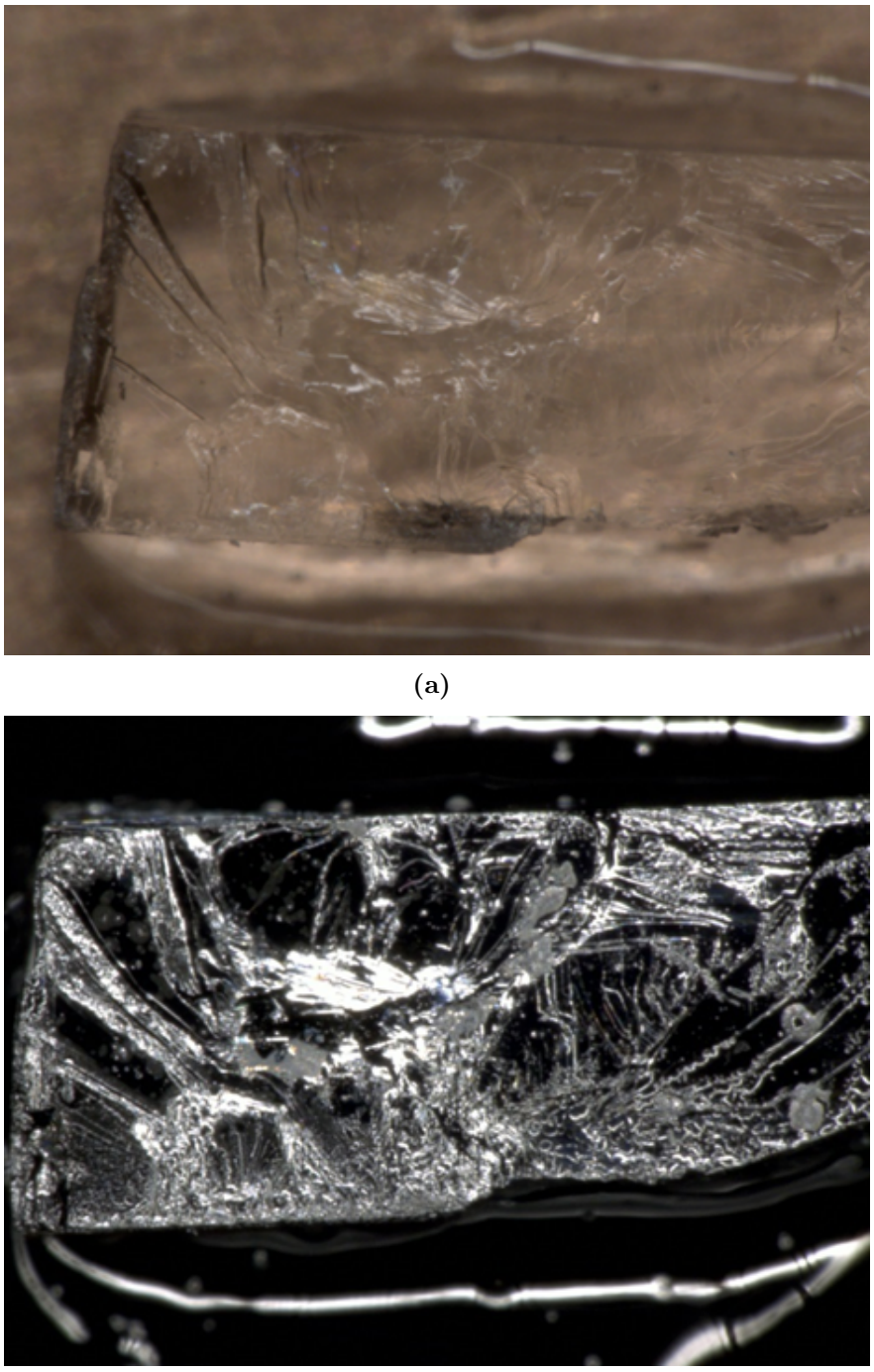

(a)

(b)

Figure 7.4. Microscope images of sample B: (a) prior to and (b) after aluminum coating deposition.

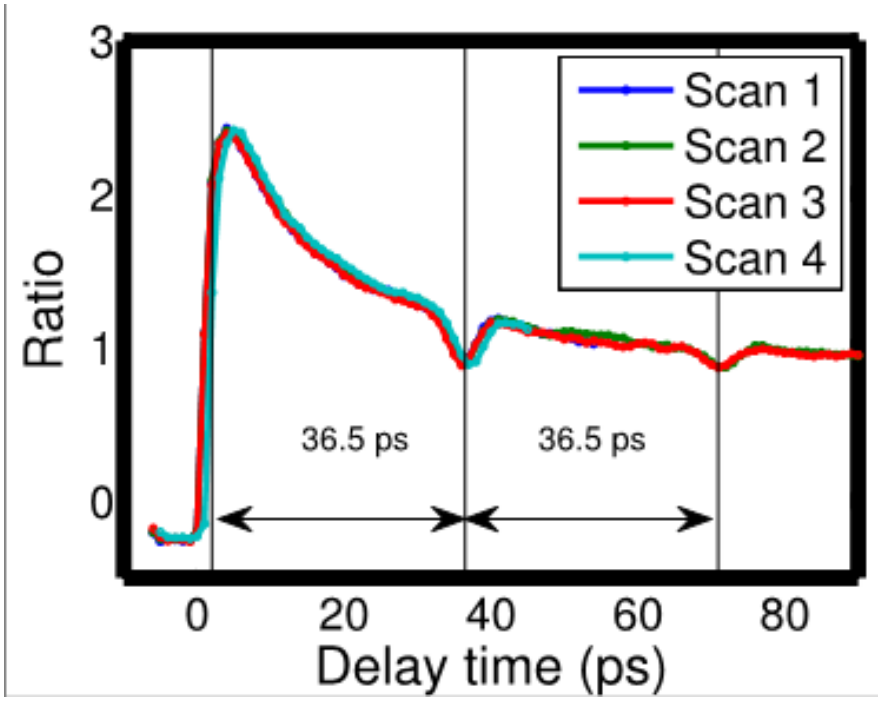

Figure 7.5. Ratio of the in-phase to out-of-phase TDTR signal for four scans on sample A showing the initial increase due to the pump pulse heating and subsequent decay.

36.5 ps, consistent with a 117 nm Al film.

Figure 7.6 shows five scans for sample A with delay times from 500 to 4000 ps. Again the first two scans are collected at a single location and then the sample moved to new locations prior to scans 3-5. The decay for the ratio of the in-phase to out-of-phase ratio of the TDTR signal is fairly consistent. Table 1 lists the modulation and sample frequencies, pump and probe powers, and pump and probe radii for the TDTR experiments that were used to fit the thermal conductivities and thermal boundary conductances. In addition to the Al film thickness of 117 nm, parameters that were specified when fitting the TDTR data are the Al volumetric specific heat of 2.44 J/(cm^{3}K) and Al thermal conductivity of 200 W/(mK) and AP volumetric specific heat of 2.125 J/(cm^{3}K) and an initial value of the AP thermal conductivity of 0.502 W/(mK). Since the decay in the in-phase to out-of-phase voltage is most sensitive to interface thermal conductance at earlier times, the window for the data analysis is varied and the results examined. The data was fit for the AP thermal conductivity and thermal conductance between the Al and AP. For the sample A data shown in Figure 7.6, analyzing the data from 500 to 4000 ps for the thermal conductivity resulted in an AP thermal conductivity of 0.485 $\pm$ 0.024 W/mK. This value was then kept constant and used to fit the decay data from 100 to 4000 ps to yield a thermal conductance value of 52 $\pm$ 17 mW/m^{2}K. The thermal conductivity and interface thermal conductance results are summarized in Table 2.

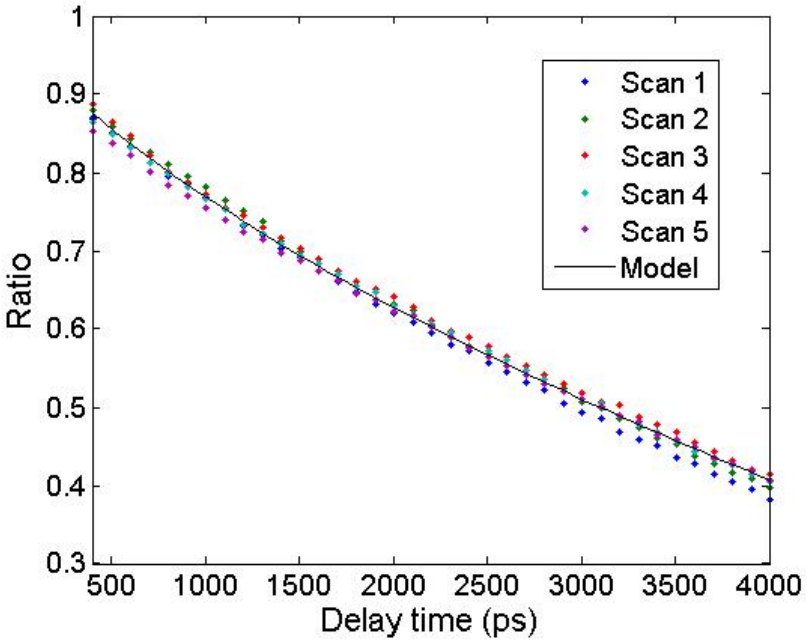

Figure 7.6. Decrease in the ratio of the in-phase to the out-of-phase signal for TDTR for sample A from 500 ps to 4000 ps and the model fit for a thermal conductivity of 0.485 $\pm$ 0.024 W/mK and thermal conductance of 52 $\pm$ 17 mW/m^{2}K

The results from sample B are also listed in Table 2. Note from Table 1 that sample B was tested at both a modulation frequency of 11.3 MHz (scans 1-5) and a lower modulation frequency of 5.89 MHz (scans 6-9). For sample B, scans 1 and 2 are at a set location and the sample was again moved to new locations prior to scans 3-5. Also, scans 6 and 7 were performed at the same location and the sample was moved prior to scans 8 and 9. It was more difficult to find a location on sample B that provided good signal-to-noise than it had been on sample A which was attributed to sample B being less smooth and more terraced than sample A. For the 11.3 MHz modulation frequency experiments, the data was analyzed from 2000 to 4000 ps to obtain an AP thermal conductivity of 0.476 ± 0.041 W/mK and from 100 to 2000 ps to obtain a thermal conductance of 141 ± 63 mW/m^{2}K. For the 5.89 MHz modulation frequency experiments, the data was analyzed from 1000 to 4000 ps to obtain an AP thermal conductivity of 0.564 ± 0.035 W/mK and from 100 to 2000 ps to obtain a thermal conductance of 90 ± 16 mW/m^{2}K.

While the thermal conductivity for sample B is fairly consistent with that for sample A, the thermal interface conductance is significantly higher. During the data analysis, the fits to the sample B data were less satisfactory than those for sample A. Thus, the differences in the interface resistances could indicate a lower quality interface between the Al and AP for sample B compared to sample A. It is also possible that the sample B data was simply of lower quality due to the surface condition. Another explanation is that the Al film thickness varied across the sample and was not constant at 117 nm. The TDTR data analysis is sensitive to the Al film thickness and variations in the Al film thickness would change the results from the data analysis. More experiments are needed to definitively determine the range of values for the interface thermal conductance between Al and AP.

Summary

Thermal conductivity and interface conductance were determined experimentally using time domain thermoreflectance (TDTR) which measures the change in surface reflectance due to a heating pulse and relates the change in the surface reflectance to the thermal properties of the sample. Two ammonium perchlorate crystal pieces were coated with aluminum and investigated using TDTR. The TDTR experiments demonstrate the viability of this technique for materials that are constituents in pyrotechnics and the potential for determining thermal interface conductance between pyrotechnic powder constituents with TDTR. When the TDTR experiment was operated at 11.3 MHz, the thermal conductivities for the two samples were 0.485 ± 0.024 W/mK and 0.476 ± 0.041 W/mK. The thermal interface conductances for the two samples were 52 ± 17 mW/m^{2}K and 141 ± 63 mW/m^{2}K. The sensitivity to the interface thermal conductance was less than that to the thermal conductivities. Future efforts are needed to more definitively establish the thermal boundary conductance between ammonium perchlorate and aluminum although the measured values are on the same order as that predicted numerically in section X.

sample	scan	mod. freq. (MHz)	probe power (mW)	pump power (mW)	sample freq. (MHz)	probe radius (μm)	pump radius (μm)
A	1	11.3	10	20	81.55	5.1	22.5
A	2	11.3	10	20	81.55	5.1	22.5
A	3	11.3	10	20	81.55	5.1	22.5
A	4	11.3	10	20	81.55	5.1	22.5
A	5	11.3	10	20	81.55	5.1	22.5
B	1	11.3	10	20	81.55	2.55	25.4
B	2	11.3	10	20	81.55	2.55	25.4
B	3	11.3	10	20	81.55	2.55	25.4
B	4	11.3	10	20	81.55	2.55	25.4
B	5	11.3	10	20	81.55	2.55	25.4
B	6	5.89	8.6	19	81.55	2.55	25.4
B	7	5.89	8	18	81.55	2.55	25.4
B	8	5.89	8	17	81.55	2.55	25.4
B	9	5.89	8	17	81.55	2.55	25.4

Table 7.1. Table 1: Experimental Conditions for the sample A and sample B TDTR measurements

sample	mod. freq. (MHz)	thermal conductivity (W/mK)	thermal boundary conductance (mW/m^2K)
A	11.3	0.485 ± 0.024	52 ± 17
B	11.3	0.476 ± 0.041	141 ± 63
B	5.89	0.564 ± 0.035	90 ± 16

Table 7.2. Table 2: AP Thermal Conductivity and Al/AP Thermal Boundary Conductance

Chapter 8

Thermal Boundary Conductance Modeling

The existence of a finite thermal boundary conductance (TBC) between materials, even at a structurally perfect interface, has been known since the work of Kapitza in 1941 [42]. In recent years, interest in predicting this quantity has increased because device miniaturization and integration often increases the relative importance of interface conductance compared to its bulk counterpart.

In this work, the high heat fluxes created by burning pyrotechnic materials makes the temperature field very sensitive to the interface conductance. A modeling effort was therefore undertaken to predict the TBC between potassium perchlorate and titanium.

The diffuse mismatch model (DMM) [83] for predicting thermal boundary conductance requires phonon information from both interacting materials. Various simplifying assumptions have been used in the past to make this model mathematically tractable. In contrast, for this work, dispersion relations over the entire Brillouin zone are recovered from density functional theory (DFT) calculations. This information is then used in the DMM to compute thermal boundary conductance.

DFT Calculations

The calculations of the force constants are based on supercell approach with finite displacements with the forces and energies obtained from electronic DFT calculations. In the supercell approach [70], a periodic extension of the crystal structure is used. Finite displacements of particular atoms are made and the resulting force on all of the atoms in the supercell is determined. This provides the data for the determination of the force constants. Crystal symmetry is used to limit the number of calculations. The use of periodic boundary conditions is a computational convenience since most electronic structure codes assume periodic systems, but it does introduce approximations. The supercell approach would be exact to within numerical errors if performed on an infinite system. The periodic system implies that all the periodic images of the displaced atom are also displaced. The effect of the periodic boundary conditions can be systematically reduced by the use of larger supercells. Further,

it can be shown [70] that the phonon properties computed at the reciprocal lattice vectors of the supercell will be correct. The evaluation of the force constants and the subsequent computation of the phonon properties was performed using the code PHONOPY [85, 84].

The calculation of the energy and forces is performed with the Vienna Ab Initio Simulation Package (VASP) [48]. This is a plane-wave code pseudopotential code. The pseudopotentials employed here are of the projector augmented-wave (PAW) form and are taken from the VASP pseudopotential database [49]. The k-space integrations are performed using a Monkhorst-Pack (MP) [61] mesh. The mesh size was varied to obtain convergence of the energy, forces and stresses. The computational details for each material will be described below.

Phonon predictions were performed for Al, Si, Ti, and potassium perchlorate ($KClO_4$). Calculations were also attempted for ammonium perchlorate (NH_4ClO_4) but, as discussed below, these calculations were not successful. The Al and Si calculations were performed to facilitate the calculation of the conductivity at the well-studied Al-Si interface. The Ti and potassium perchlorate calculations facilitate the determination of the phonon transport between these two components of energetic materials.

Aluminum

The aluminum calculations were performed using the PAW pseudopotential from the standard VASP library. This pseudopotential includes the outer three s- and p-electrons as valence with the remaining electrons in the core. The plane wave cut-off energy employed was 300 eV. The computational supercell is a 5x5x5 repeat of the cubic face-centered-cubic (FCC) unit cell for a total of 256 atoms. The calculations employed a 12x12x12 MP k-space mesh. The predicted lattice constant was 4.04 Å which agrees well with the experimental lattice constant of 4.05 Å. The phonon calculations were performed at the experimental lattice constant. The predicted total phonon density of states is shown in Figure 8.1 and displays the typical shape for an FCC metal.

Silicon

The silicon calculations employed the PAW pseudopotential from the standard VASP library. This pseudopotential includes the outer four s- and p-electrons as valence with the remaining electrons in the core. The plane wave cut-off energy used in the calculations was 307 eV. The computational supercell is a 4x4x4 repeat of the cubic cell of the diamond structure for a total of 512 atoms along with a 6x6x6 MP k-space mesh. The predicted lattice constant from the DFT calculations was 5.47 Å compared to the experimental lattice constant of 5.43 Å. The phonon calculations were performed for the experimental lattice constants. The predicted total phonon density of states is shown in Figure 8.2.

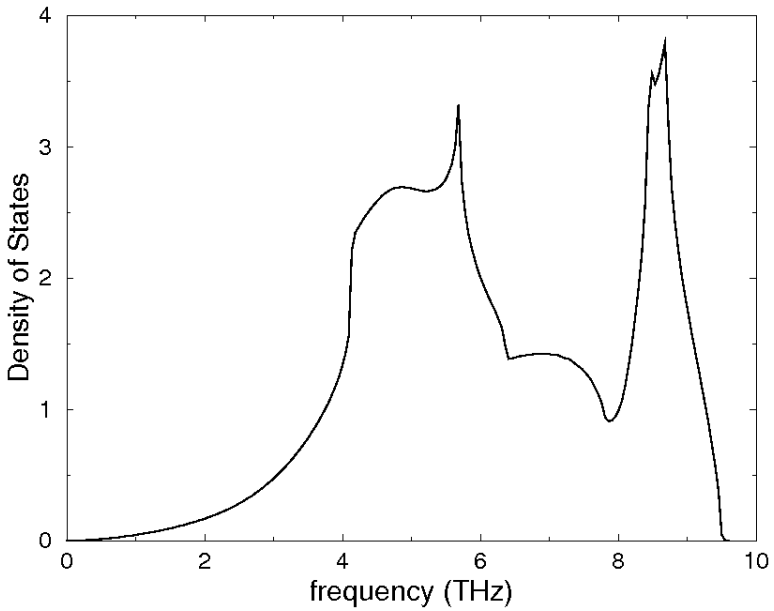

Figure 8.1. Predicted phonon density of states for aluminum.

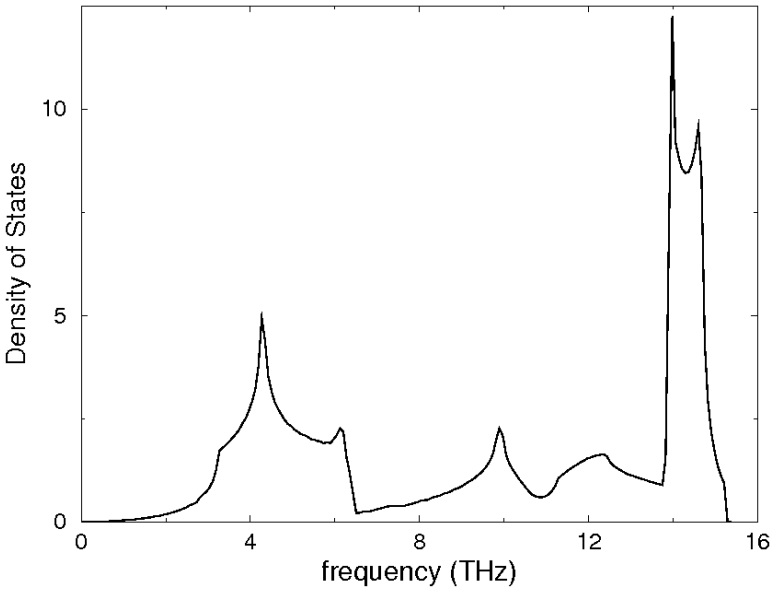

Figure 8.2. Predicted phonon density of states for silicon.

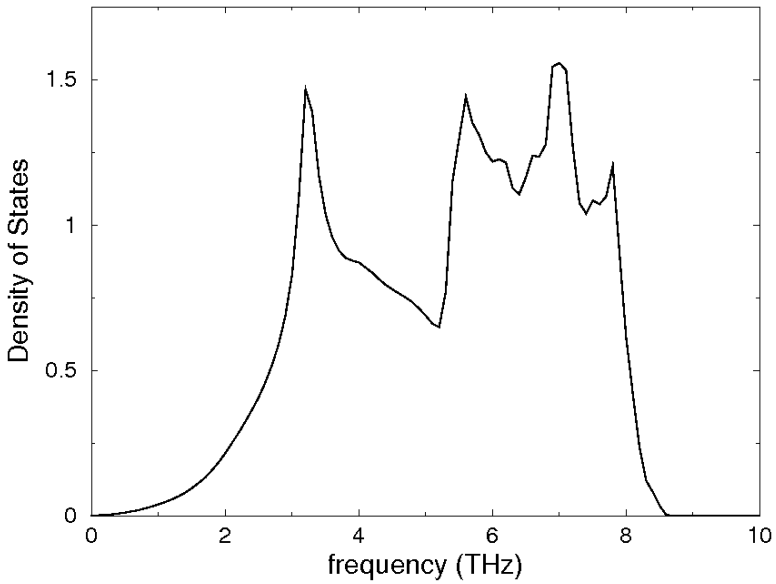

Figure 8.3. Predicted phonon density of states for titanium.

Titanium

The pseudopotential for the Ti calculations was of the PAW form and taken from the standard VASP library. These pseudopotentials treat the four s- and d-electrons as valence and the remaining electrons in the K core. The plane wave cut-off employed was 222 eV. The computational supercell is a 6x6x6 repeat of the hexagonal-close-packed (HCP) cell for a total of 432 atoms. The k-space integration was performed with a gamma-centered 3x3x1 MP mesh. The predicted lattice constant is a = 2.92 Å with c/a = 1.58. This compares to the experimental lattice constant of a = 2.95 Å with c/a = 1.59. The phonon calculations were performed for the DFT predicted lattice constants. The predicted total phonon density of states is shown in Figure 8.3.

Potassium perchlorate

The pseudopotentials employed in these calculations are the PAW potentials taken from the standard VASP library with 9, 7 and 6 valence electrons for K, Cl and O, respectively. The plane-wave cut-off employed was 500 eV and is dictated by the O pseudopotential. The structure was determined using a 24 atom orthorhombic unit cell and a 4x6x4 MP k-space mesh. The phonon calculations employed a 2x3x2 repeat of the orthorhombic cell with 288 atoms and a 2x2x2 MP k-space mesh.

The structure of $KClO_4$ has been determined experimentally by Mani [54] and by Jo-

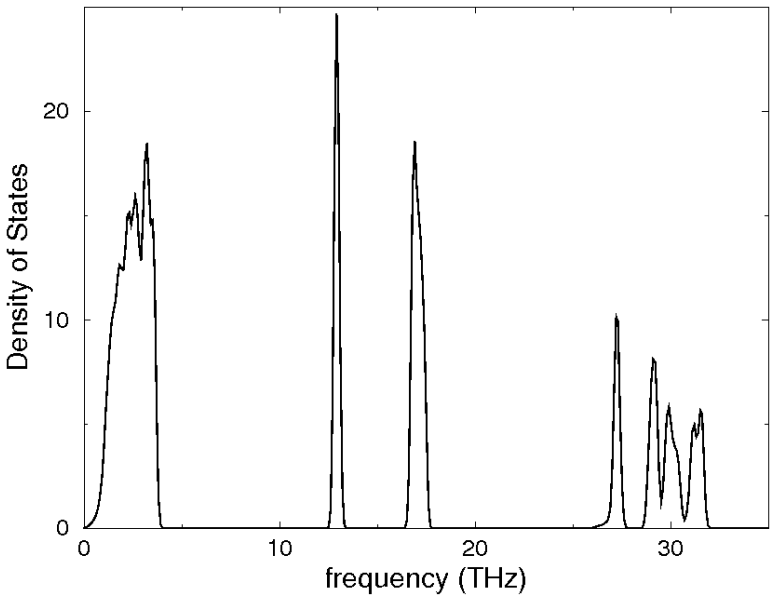

Figure 8.4. Predicted phonon density of states for potassium perchlorate.

hansson and Lindqvist (JL) [40]. It is an orthorhombic crystal with four molecular units per cell and *Pnma* symmetry. The experimental lattice constants are reported to be a = 8.83 Å, b = 5.65 Å and c = 7.24 Å by Mani and as a = 8.866 Å, b = 5.666 Å and c = 7.254 Å by JL. The present DFT predictions are a = 9.05 Å, b = 5.77 Å and c = 7.40 Å. The DFT predicts a larger lattice constants but the agreement is reasonable. The internal relaxation parameters have also been measured and are obtained in the DFT structural optimization. The results are compared in Table 8.1 where the positions are reported as fractions of the relevant lattice constants. The agreement is good especially with the more recent results of JL.

The predicted phonon density of states in shown in Figure 8.4. Note that the density of states has a low frequency branch and several distinct higher frequency portions. The partial density of states associated with each element is shown in Figure 8.5. The vibrations associated with the K atoms are essentially restricted to the low frequency branch. The higher frequency modes are associated with just O and Cl motion. This indicates that the higher frequency modes are associated with internal vibrations of the perchlorate ion. As such, they will have specific heat, but will not contribute to thermal transport.

Ammonium perchlorate

The crystal structure of ammonium perchlorate, NH_4ClO_4 is believed to be similar to that of potassium perchlorate with the replacement of the potassium ion with an ammonia

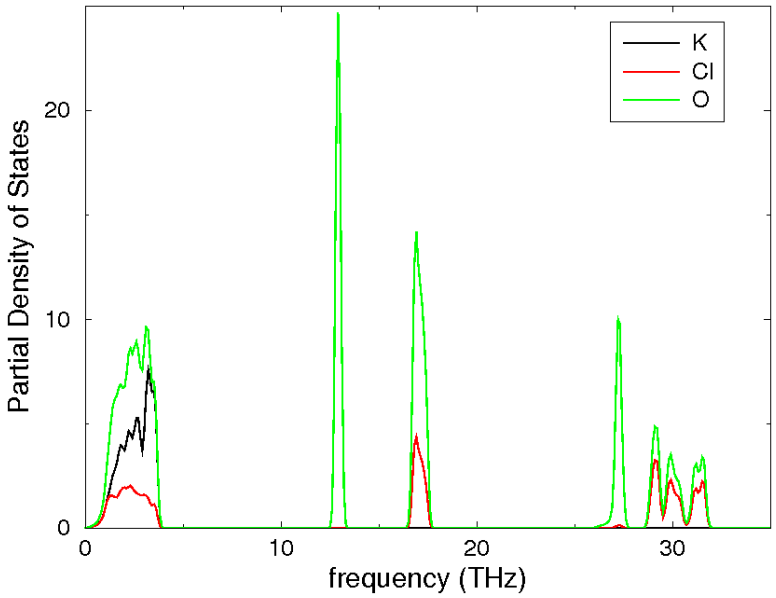

Figure 8.5. Predicted partial phonon density of states for potassium perchlorate.

Atom	DFT (present)			JL (1977)			Mani (1957)		
	X	Y	Z	X	Y	Z	X	Y	Z
K	0.182	0.75	0.161	0.181	0.75	0.163	0.183	0.75	0.167
Cl	0.434	0.25	0.190	0.432	0.25	0.190	0.425	0.25	0.189
O_1	0.315	0.25	0.056	0.312	0.25	0.058	0.325	0.25	0.050
O_2	0.577	0.25	0.102	0.575	0.25	0.098	0.578	0.25	0.106
O_3	0.420	0.043	0.305	0.420	0.044	0.305	0.417	0.042	0.319
O_4	0.420	0.457	0.305	0.420	0.456	0.305	0.417	0.458	0.319

Table 8.1. Comparison of internal relaxation parameters for potassium perchlorate computed via DFT with previous measurements.

group [90]. Subsequent studies have examined the temperature dependence of the structure at low temperatures [15, 72, 31]. These studies indicate that the rotational modes of the ammonia ion are very easy and are significant at temperatures as low as 20 K. There is disagreement about the presence of a low temperature phase transition. Prask and coworkers [15, 72] assert that there is no change in the structure down to 10 K. Stammler, et al. [81] suggest that there is a phase transition at 83 K based on changes observed in x-ray diffraction with temperature. Hamada, et al. [31] note that there are anomalous changes in the temperature dependence of the lattice constants around 80 K and that their x-ray diffraction data at 80 K cannot distinguish between the centrosymmetric *Pnma* symmetry observed at room temperatures and a noncentrosymmetric $Pn2_1a$ symmetry. Thus the low temperature structure of ammonium perchlorate is uncertain.

DFT structural optimizations were attempted based on the various experimental structure determinations. The structural optimizations algorithms in VASP had difficulty obtaining minimum energy structures. This is consistent with the easy rotation of the ammonia groups that was observed experimentally. Ultimately, apparent minimum energy structures were obtained and the phonon analysis was performed. In each case, the phonon analysis indicated negative frequency modes, in other words that the predicted structure was not true minimum but probably a saddle point. This inability to obtain the true DFT minimum energy structure prevented the determination of the phonon spectra. This failure could have multiple causes. First, the initial structural guesses may not be sufficiently close to the minimum to converge. Second, the calculations assumed *Pnma* symmetry which experiment suggests might not be correct at low temperatures. Of course, if the zero temperature structure is not the room temperature structure, the phonon properties of the zero temperature structure are not appropriate for the thermal transport at room temperature. This failure suggests that current DFT calculation techniques are not sufficiently robust to predict phonon properties of complex crystal structures in some cases.

Diffuse Mismatch Model Calculations

Previous DMM calculations all simplified the dispersion relation in some way. In the original DMM [83], the Debye approximation was used to replace all phonon polarization with a single linear branch. Subsequent calculations used linear fits to the transverse and longitudinal acoustic branches, then polynomial fits [21] to capture dispersion. Polynomial fits to the optical branches were then added [4].

In all these calculations, the Brillouin zone was considered spherical, with the dispersion relation in one direction applied to all directions. In the case of silicon, which has cubic symmetry, this is a good approximation. Hopkins et al. [36], however, showed that a spherical Brillouin zone is not a good assumption for sapphire, which has a Brillouin zone that is better approximated by a cylinder. Supporting the theoretical result, Hopkins et al. showed a measurable dependence of TBC on substrate crystallographic orientation for aluminum on sapphire but not for aluminum on silicon.

Breaking from these previous efforts, Reddy et al.[74] used a dispersion relation derived from the Born-von Karman (BKM) lattice dynamical model to compute the TBC of metal-semiconductor pairings of Al, Cu, Si, and Ge. In their case, the integrals usually employed in DMM calculations were replaced by discrete sums, each taken over the discretized cells in the k-space used in their BKM model.

The current work extends this effort by using the VASP calculations discussed in the previous section to provide a detailed description of the phonon spectrum in the complex materials of interest. This information is then processed using PHONOPY, which provides a convenient means for extracting phonon information from VASP output. In particular, it was used in this work to compute group velocities and the location and weights of "special" points [61] in the Brillouin zone. These special points were then used to replace integration over wavevector space with a sum. The relevant equations are therefore identical to those employed by Reddy et al.[74] except that the (constant) discrete volume in k-space is replaced by the special point weights.

The thermal boundary conductance, h is therefore given by:

$$h = \frac{N_a k_B}{2 f V_m} \sum_{\mathbf{k},j} W \mid \mathbf{v} \cdot \mathbf{n} \mid \zeta x^2 \frac{e^x}{e^x - 1} \tag{8.0.1}$$

where the sums are taken over all wavevectors ($\mathbf{k}$) and polarizations (j). $\mathbf{v}$ is the group velocity, $\mathbf{n}$ is the normal to the interface, W is the weight of the special point, N_a is Avogadro's constant, V_m is the molar volume and f is the number of formula units per unit cell, which is required because PHONOPY calculates on a per unit cell basis. For convenience, x is defined as $\frac{\hbar\omega}{k_B T}$, where $\hbar$ is Planck's constant divided by 2π, ω is the frequency, k_B is Boltzmann's constant, and T is the temperature. All variables within the summation are functions of wavevector and polarization, with the exception of W, which depends only on wavevector.

Due to energy conservation, all quantities in Equation 8.0.1 except the transmission coefficient, ζ, refer to only one of the two materials that make up the interface [83]. Subscripting this material's properties with a 1 and its partner's properties with a 2, the transmission coefficient is given by:

$$\zeta(\omega) = \frac{\sum_{\mathbf{k},j} \mid \mathbf{v}_2 \cdot \mathbf{n} \mid W_2(\mathbf{k}) \delta_{\omega'(\mathbf{k},j),\omega}}{\frac{V_{m_2} f_2}{V_{m_1} f_1} \sum_{\mathbf{k},j} \mid \mathbf{v}_1 \cdot \mathbf{n} \mid W_1(\mathbf{k}) \delta_{\omega'(\mathbf{k},j),\omega} + \sum_{\mathbf{k},j} \mid \mathbf{v}_2 \cdot \mathbf{n} \mid W_2(\mathbf{k}) \delta_{\omega'(\mathbf{k},j),\omega}} \tag{8.0.2}$$

where the delta functions enforce energy conservation on a per-frequency basis by requiring the incoming and outgoing modes to have identical frequencies. This constraint is known as elastic scattering and its implications are explored elsewhere [37, 23].

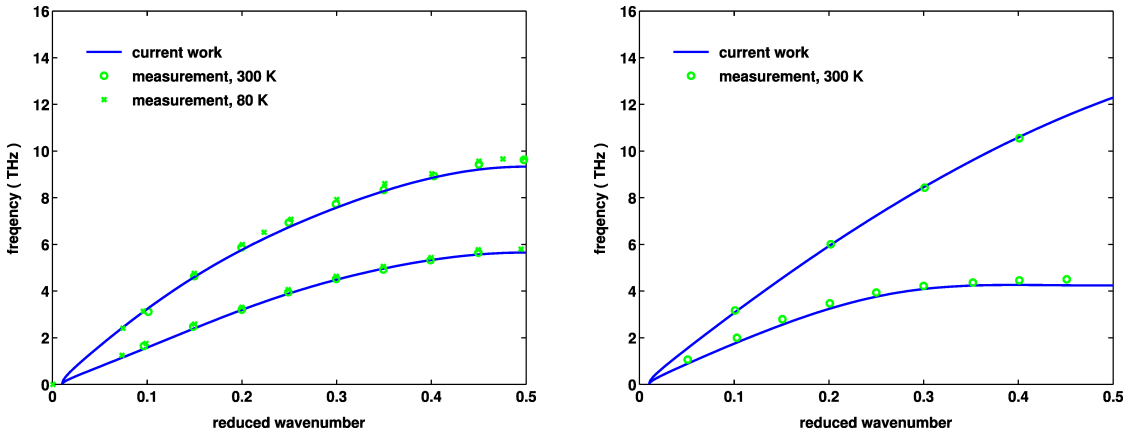

(a) aluminum **(b)** silicon

Figure 8.6. Comparison of computed and measured acoustic phonon dispersion for aluminum and silicon in the (100) direction.

Aluminum - Silicon

The aluminum-silicon material pair was chosen for testing the current computational strategy because several previous authors [36, 74, 39, 38, 60, 22] have measured and/or computed TBC for this pair.

Because the phonon wavevector-frequency relationship, or dispersion relation, is the basis for computation under the DMM, these relations were first checked against their measured counterparts using neutron scattering data from Stedman and Nilsson [82] and Dolling [20] (as reported by Giannozzi et al.[27]) for aluminum and silicon, respectively.

Overall, good agreement between the computed and measured frequencies are evident. For silicon, the relationship between computed and measured data follows the same trend observed in earlier work by Giannozzi et al.[27], particularly the slight underprediction of frequencies for the transverse acoustic (lower) branch.

These dispersion relations are then used to compute the transmission coefficient, ζ, using Equation 8.0.2. The resulting transmission coefficient as a function of frequency is shown in Figure 8.7 with the dispersion relations for reference. It may be observed that the optical modes in silicon do not participate in energy transfer across the interface under the elastic formulation expressed in Equation 8.0.2 because aluminum has no modes available in their frequency range.

Computing the TBC for this material pair from Equation 8.0.1, the results are compared to previous DMM calculations, as well as to measured data in Figure 8.8. The previous DMM calculations use a polynomial fit to measured dispersion relations in one direction (Duda et al. [22]) and an integration over a discretized full Brillouin zone derived from a Born-von

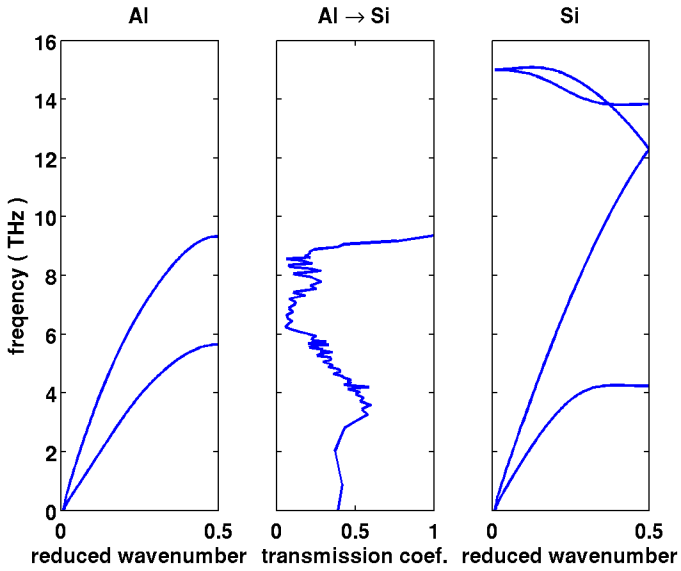

Figure 8.7. Dispersion relations in the (100) direction for silicon and aluminum, with the transmission coefficient for an Al-Si interface between them.

Karman model (Reddy et al. [74]). The measurements were performed on an interface in which steps were taken to remove the native oxide that is usually present on a silicon surface before depositing the aluminum. The resulting interface is therefore a reasonable approximation of the atomically sharp interface assumed in the model.

The agreement between the models and to the data is reasonable. While previous models have underpredicted the TBC for this material pair, the current model overpredicts it. From a physical standpoint, for a perfect model, overprediction is more reasonable because a real interface will tend to have a lower conductance due to the presence of oxide, defects, and atomic intermixing. Less than 1 nm of oxide would, for example, close the gap between the current work and the data.

While it is tempting to declare victory at this result, it should be pointed out that the DMM is not a perfect model and also that Duda et al. worked from measured dispersion relations, which are reasonably simple and nearly direction-independent. A large difference between their work and the current work is therefore not expected. (Reddy et al. did not show a comparison between their dispersion relation and measured values, so it is difficult to assess the accuracy of their lattice dynamics model.) Nonetheless, because the agreement is certainly within the error bars imparted by uncertainties introduced by the physical system, it provides sufficient confidence in the model to move on to the more complex materials of interest, where previous models would be difficult to implement.

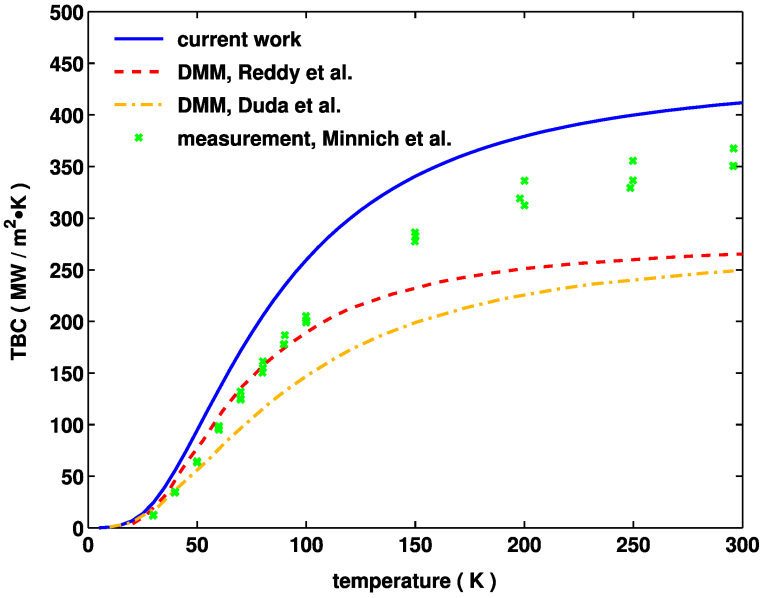

Figure 8.8. Comparison of thermal boundary conductance computed in the current work to previous DMM computations and measured values.

Aluminum - Potassium Perchlorate

The aluminum-potassium perchlorate system was modeled as a stand-in for the aluminum-ammonium perchlorate system measured with TDTR, as described in Section 7. Due to the difficulties in obtaining VASP results for ammonium perchlorate described in Section 8, as well as a lack of neutron scattering data, a dispersion relation for ammonium perchlorate is unavailable. It can be argued that its phonon spectrum should be at least somewhat similar to that of potassium perchlorate.

The transmission coefficient for an aluminum-potassium perchlorate interface is shown in Figure 8.9, along with the dispersion relations for each material. Unlike the Al-Si pair, optical phonons are very important for transport in the Al-$KClO_4$ pair, due to the very low acoustic frequencies and the large number of optical modes in $KClO_4$.

The computed TBC is shown in Figure 8.10. Given the large acoustic mismatch between these materials, it is not surprising that the TBC is much lower than that observed for the Al-Si pair. Reassuringly, the value at 300 K is within the range of measured values for the aluminum-ammonium perchlorate pair presented in Section 7.

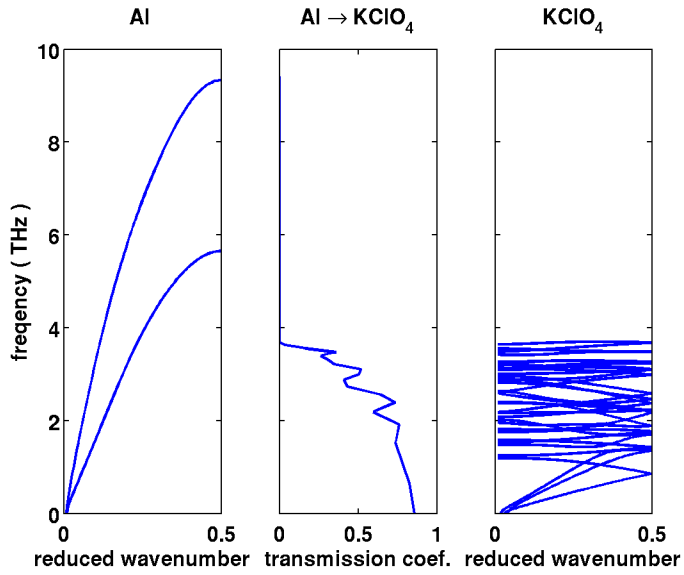

Figure 8.9. Dispersion relations for aluminum and potassium perchlorate with the transmission coefficient for an Al-$KClO_4$ interface between them. The potassium perchlorate dispersion relation is truncated; It actually extends to nearly 32 THz.

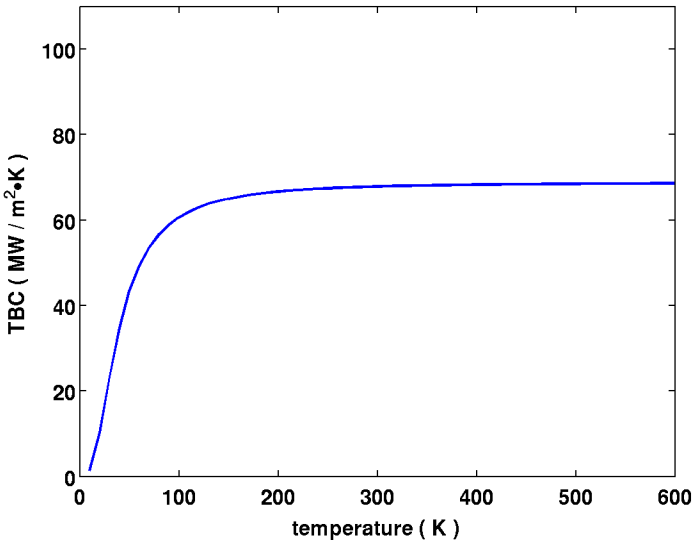

Figure 8.10. Computed thermal boundary conductance for aluminum on potassium perchlorate.

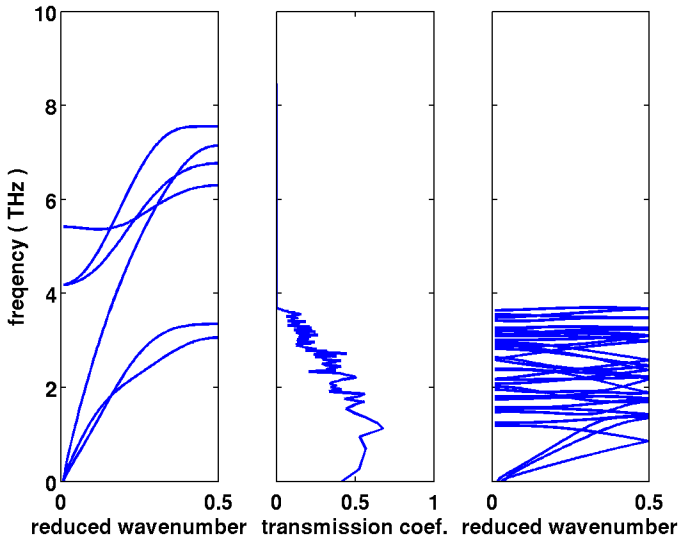

Figure 8.11. Computed thermal boundary conductance for titanium on potassium perchlorate.

Titanium - Potassium Perchlorate

The titanium-potassium perchlorate system was modeled because these interfaces are present in the pyrotechnic devices of interest in the current work.

Following the template established in previous sections, the dispersion relations are paired with the transmission coefficient in Figure 8.11. It may be noted from this figure that titanium has optical modes with appreciable group velocities. Comparing its dispersion relation to that of $KClO_4$, however, it can be seen that these modes are unable to participate in transport across the interface under the elastic assumption because their frequencies fall entirely within one of the $KClO_4$ bandgaps.

The computed TBC is shown in Figure 8.12. Comparing this figure to Figure 8.10, it can be seen that titanium has a much larger TBC than aluminum when paired with potassium perchlorate. This is somewhat surprising, given the slightly lower transmission coefficient and titanium's somewhat lower group velocity. The explanation may be found be comparing the density of states for aluminum in Figure 8.1 to that of titanium in Figure 8.3. While both materials have a similar structure to their density of states, titanium has a peak within the $KClO_4$ frequency range while aluminum does not. Titanium therefore has more carriers available for transport across the interface.

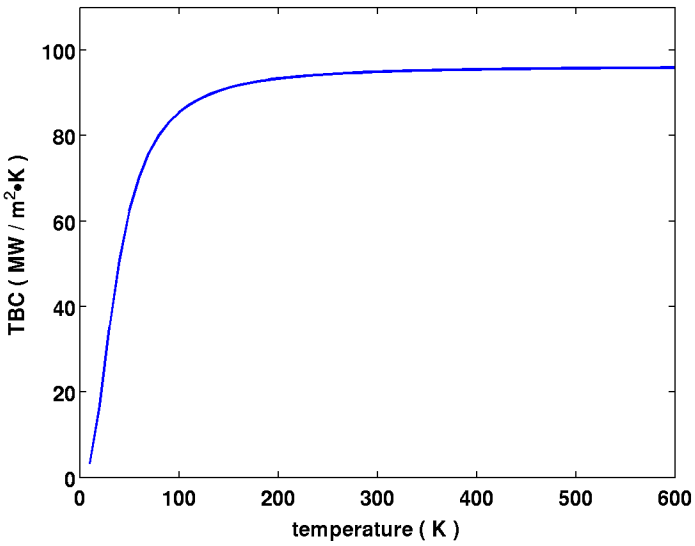

Figure 8.12. Computed thermal boundary conductance for titanium on potassium perchlorate.

Chapter 9

Summary and Conclusions

The goal of the project was to develop and apply a novel scale-consistent modeling framework to couple spatial and temporal correlations from micro through meso to macro scales for thermal transport in a particle-based composite material. Initially, we sought to address the scale dependence of the temporal aspects of heat transport into powder (i.e., non-Fickian, sub-diffusive behavior). Ultimately, success amounts to relating measures of spatial inhomogeneity (e.g., microstructural correlation functions) to temporal response in order to model time dependent bulk thermal conductivity. Moreover, success entails demonstration of the models ability to capture spatial inhomogeneity as a function of resolution and account for variability of effective properties.

Two related issues made full achievement of the goal a significant challenge. First, it must be noted that above metric is poorly formed as stated in that it takes for granted the rest of the significant work detailed in Chapters 2, 4 and 7 – experimental characterization and discovery. Much was accomplished in these efforts. Chapter 7 summarizes the first ever (as far as the authors know) application of TDTR to actual pyrotechnic materials. This is the first attempt to actually characterize these materials at the interfacial scale. Chapter 4 describes sucess, although preliminary, in resolving thermal fields at speeds and spatial scales relevant to energetic components, for the first time. Likewise, the FIB-SEM imaging referred to in Chapter 5 is a first of its kind for these particular materials. As summarized in Chapter 2 a flash diffusivity capability for measuring homogeneous thermal conductivity of pyrotechnic powders (and beyond) was advanced; leading to enhanced characterization of pyrotechnic materials and properties impacting component development. In addition, modeling work described in Chapter 8 led to improved prediction of interface thermal conductance from first principles calculations, while advances were also made in image processing, meshing, and direct numerical simulation of complex structures (see Chapters 3 and 5). Thus, the original goal was too narrowly focussed on the modeling effort before allowing for the forming of a clear multi-scale picture.

Second, as a result of the first point, in hindsight this metric was overly ambitious when combined with the programmatic details of the project, particularly the short time line. The breadth of the work described in the original technical approach seems accurate, but the impact of the shortened timeline was to limit the integration of the various efforts; tying them all back together after their initial parallel, shotgun start. Nonetheless, for a model system of packed particles, significant headway was made in implementing numerical

algorithms and collecting data to justify the approach in terms of highlighting the phenomena at play and pointing the way forward (see Chapter 6) in developing and informing the kind of modeling approach envisioned here.

References

[1] American Society of Testing and Materials. *Standard Test Method for Thermal Diffusivity by the Flash Method: E1461-13*, 2013.

[2] T. Azumi and Y. Takahashi. Novel finite pulse-width correction in flash thermal diffusivity measurement. *Review of Scientific Instruments*, 52(9):1411, 1981.

[3] Isaac Balberg. Continuum percolationpercolation. In Robert A. Meyers, editor, *Encyclopedia of Complexity and Systems Science*, pages 1443–1475. Springer New York, 2009.

[4] T. Beechem, J.C. Duda, P.E. Hopkins, and P.M. Norris. Contribution of optical phonons to thermal boundary conductance. *Applied Physics Letters*, 97(6), Aug 2010.

[5] Y. Beers. *Introduction to the Theory of Error*. Addison-Wesley, Cambridge Mass., 1953.

[6] J.-P. Bouchaud and A. Georges. Anomalous diffusion in disordered media: Statistical mechanisms, models and physical applications. *Physics Reports*, 195(4–5):127–293, 1990.

[7] G. Bradski. *Dr. Dobb's Journal of Software Tools*.

[8] Von DAG Bruggeman. Berechnung verschiedener physikalischer konstanten von heterogenen substanzen. i. dielektrizitätskonstanten und leitfähigkeiten der mischkörper aus isotropen substanzen. *Annalen der physik*, 416(7):636–664, 1935.

[9] D. G. Cahill. Analysis of heat flow in layered structures for time-domain thermoreflectance. *Review of Scientific Instruments*, 75:5119–5122, 2004.

[10] D. G. Cahill, W. K. Ford, K. E. Goodson, G. D. Mahan, A. Majumdar, H. J. Maris, R. Merlin, and S. R. Phillpot. Nanoscale thermal transport. *Journal of Applied Physics*, 93:793–818, 2003.

[11] D. G. Cahill, K. E. Goodson, and A. Majumdar. Thermometry and thermal transport in micro/nanoscale solid-state devices and structures. *Journal of Heat Transfer*, 124:223–241, 2002.

[12] H. S. Carslaw and J. C. Jaeger. *Conduction of Heat in Solids, 2nd Edition*. Oxford University Press, 1959.

[13] P. Chaudhuri, L. Bertheir, and W. Kob. Universal nature of particle displacements close to glass and jamming transition. *Physical Review Letters*, 99:060604, 2007.

[14] Alexei F Cheviakov, Michael J Ward, and Ronny Straube. An asymptotic analysis of the mean first passage time for narrow escape problems: Part ii: The sphere. *Multiscale Modeling & Simulation*, 8(3):836–870, 2010.

[15] C.S. Choi, H.J. Prask, and E. Prince. Crystal structure of NH_4ClO_4 at 298, 78 and 10 K by neutron diffraction. *Journal of Chemical Physics*, 61(9):3523–3529, 1974.

[16] Marcia A. Cooper. Flash diffusivity measurements on pyrotechnics. Sandia National Laboratories Work Authorization Form (WAF) #55-0205B, March 2014.

[17] Eric I Corwin, Heinrich M Jaeger, and Sidney R Nagel. Structural signature of jamming in granular media. *Nature*, 435(7045):1075–1078, 2005.

[18] R.D. Cowan. Propsed method of measuring thermal diffusivity at high temperatures. *Journal of Applied Physics*, 32(7):1363, 1961.

[19] R.D. Cowan. Pulse method of measuring thermal diffusivity at high temperatures. *Journal of Applied Physics*, 34(4):926, 1963.

[20] G. Dolling. *Inelastic Scattering of Neutrons in Solids and Liquids*, volume II, page 37. IAEA, Vienna, 1963.

[21] J.C. Duda, T.E. Beechem, J.L. Smoyer, P.M. Norris, and P.E. Hopkins. Role of dispersion on phononic thermal boundary conductance. *Journal of Applied Physics*, 108(7):–, 2010.

[22] J.C. Duda and P.E. Hopkins. Systematically controlling Kapitza conductance via chemical etching. *Applied Physics Letters*, 100(11):111602, Mar 2012.

[23] J.C. Duda, P.E. Hopkins, J.L. Smoyer, M.L. Bauer, T.S. English, C.B. Saltonstall, and P.M. Norris. On the assumption of detailed balance in prediction of diffusive transmission probability during interfacial transport. *Nanoscale and Microscale Thermophysical Engineering*, 14(1):21–33, 2010.

[24] W. W. Erikson, M. A. Cooper, M. L. Hobbs, M. J. Kaneshige, Oliver M. S., and S. Snedigar. Determination of thermal diffusivity, conductivity, and energy release from the internal temperature profiles of energetic materials. *International Journal of Heat and Mass Transfer*, 79:676–688, 2014.

[25] D. Fournier and A. C. Boccara. Heterogeneous media and rough surfaces: A fractal approach for heat diffusion studies. *Physica A*, 157:587–592, 1989.

[26] Y. Gefen, A. Aharony, and S. Alexander. Anomalous diffusion on percolating clusters. *Physical Review Letters*, 50:77, 1983.

[27] P. Giannozzi, S. de Gironcoli, P. Pavone, and S. Baroni. *Ab initio* calculation of phonon dispersions in semiconductors. *Physical Review B*, 43(9):7231–7242, 1991.

[28] Michael Groeber, Somnath Ghosh, Michael D Uchic, and Dennis M Dimiduk. A framework for automated analysis and simulation of 3d polycrystalline microstructures.: Part 1: Statistical characterization. *Acta Materialia*, 56(6):1257–1273, 2008.

[29] Michael Groeber, Somnath Ghosh, Michael D Uchic, and Dennis M Dimiduk. A framework for automated analysis and simulation of 3d polycrystalline microstructures. part 2: Synthetic structure generation. *Acta Materialia*, 56(6):1274–1287, 2008.

[30] Michael A Groeber and Michael A Jackson. Dream. 3d: A digital representation environment for the analysis of microstructure in 3d. *Integrating Materials and Manufacturing Innovation*, 3(1):5, 2014.

[31] A. Hamada, S. Yamamoto, and O. Fujiyoshi. Crystal structure of NH_4ClO_4 in low temperature phase. *Journal of the Korean Physical Society*, 32(1, S):S152–S155, Feb 1998.

[32] E. A. Holm and C. C. Battaile. The computer simulation of microstructural evolution. *JOM*, 53:20–23, 2001.

[33] D. C. Hong, H. E. Stanley, A. Coniglio, and A. Bunde. Random-walk approach to the two-component random-conductor mixture: Perturbing away from the perfect random resistor network and random superconducting-network limits. *Phys. Rev. B*, 33:4564–4573, Apr 1986.

[34] P. E. Hopkins. Thermal transport across solid interfaces with nanoscale imperfections: Effects of roughness, disorder, dislocations, and bonding on thermal boundary conductance. *ISRN Mechanical Engineering*, 2013:682586, 2013.

[35] P.E. Hopkins. Interfacial electron and phonon scattering processes in high-powered nanoscale applications. Technical Report SAND2011-6936, Sandia National Labs., Albuquerque, NM (United States), Oct 2011.

[36] P.E. Hopkins, T.E. Beechem, J.C. Duda, K. Hattar, J.F. Ihlefeld, M.A. Rodriguez, and E.S. Piekos. Influence of anisotropy on thermal boundary conductance at solid interfaces. *Physical Review B*, 84:125408, Sep 2011.

[37] P.E. Hopkins and P.M. Norris. Relative contributions of inelastic and elastic diffuse phonon scattering to thermal boundary conductance across solid interfaces. *Journal of Heat Transfer-Transactions of the ASME*, 131(2), Feb 2009.

[38] P.E. Hopkins, L.M. Phinney, J.R. Serrano, and T.E. Beechem. Effects of surface roughness and oxide layer on the thermal boundary conductance at aluminum/silicon interfaces. *Physical Review B*, 82:085307, Aug 2010.

[39] W. Ih Choi, K. Kim, and S. Narumanchi. Thermal conductance at atomically clean and disordered silicon/aluminum interfaces: A molecular dynamics simulation study. *Journal of Applied Physics*, 112(5):–, 2012.

[40] G.B. Johansson and O. Lindqvist. Potassium perchlorate. *Acta Crystallography*, B33:2918–2919, 1977.

[41] M. W. Chase Jr. *NIST-JANAF Thermochemical Tables*. American Institute of Physics for the National Institute of Standards and Technology, New York, 4 edition, 1998.

[42] P.L. Kapitza. The study of heat transfer in helium II. *J. Phys. USSR*, 4:181, 1941.

[43] V. Kenkre, E. W. Montroll, and M. F. Shlesinger. Generalized master equations for continuous-time random walks. *Journal of Statistical Physics*, 9:45, 1973.

[44] In Chan Kim and S Torquato. Determination of the effective conductivity of heterogeneous media by brownian motion simulation. *Journal of applied physics*, 68(8):3892–3903, 1990.

[45] In Chan Kim and S Torquato. Effective conductivity of suspensions of hard spheres by brownian motion simulation. *Journal of applied physics*, 69(4):2280–2289, 1991.

[46] J. Klafter and R. Silbey. Derivation of the continuous-time random-walk equation. *Phys. Rev. Lett.*, 44:55–58, Jan 1980.

[47] Ann Krach and Suresh G Advani. Influence of void shape, void volume and matrix anisotropy on effective thermal conductivity of a three-phase composite. *Journal of composite materials*, 30(8):933–946, 1996.

[48] G. Kresse and J. Furthmüller. Efficient iterative schemes for ab initio total-energy calculations using a plane-wave basis set. *Physical Review B*, 54(16):11169–11186, 1996.

[49] G. Kresse and D. Joubert. From ultrasoft pseudopotentials to the projector augmented-wave method. *Physical Review B*, 59(3):1758–1775, 1999.

[50] Rolf Landauer. The electrical resistance of binary metallic mixtures. *Journal of Applied Physics*, 23(7):779–784, 1952.

[51] K. Levenberg. A method for the solution of certain nonlinear problems in least squares. *Quarterly of Applied Mathematics*, 2:164, 1944.

[52] Andrea J Liu and Sidney R Nagel. Nonlinear dynamics: Jamming is not just cool any more. *Nature*, 396(6706):21–22, 1998.

[53] William E Lorensen and Harvey E Cline. Marching cubes: A high resolution 3d surface construction algorithm. In *ACM Siggraph Computer Graphics*, volume 21, pages 163–169. ACM, 1987.

[54] N.V. Mani. The crystal structure of potassium perchlorate - $KClO_4$. *Proceedings of the Indian Academy of Sciences - Section A*, 46(2):143–151, 1957.

[55] D.W. Marquardt. An algorithm for least-squares estimations of nonlinear inequalities. *SIAM: Society for Industrial and Applied Mathematics*, 11(2):431, 1963.

[56] MathWorks. Matlab® help: Fit command. http://www.mathworks.com/help/curvefit/fit.html.

[57] MathWorks. *MATLAB® v2013b*, 2013.

[58] James Clerk Maxwell. *A treatise on electricity and magnetism*, volume 1. Clarendon press, 1881.

[59] JC Michel, H Moulinec, and P Suquet. Effective properties of composite materials with periodic microstructure: a computational approach. *Computer methods in applied mechanics and engineering*, 172(1):109–143, 1999.

[60] A. J. Minnich, J. A. Johnson, A. J. Schmidt, K. Esfarjani, M. S. Dresselhaus, K. A. Nelson, and G. Chen. Thermal conductivity spectroscopy technique to measure phonon mean free paths. *Phys. Rev. Lett.*, 107:095901, Aug 2011.

[61] H.J. Monkhorst and J.D. Pack. Special points for Brillouin-zone integrations. *Physical Review B*, 13(12):5188–5192, 1976.

[62] E. W. Montroll and G. H. Weiss. *Journal of Mathematical Physics*, 6:167, 1965.

[63] K. R. Naqvi and S. Waldenstrø m. Brownian motion description of heat conduction by phonons. *Physical Review Letters*, 95:065901, 2005.

[64] Netzsch. *LFA 447 NanoFlash® Operators Manual*, 2005. Appendix: Technical Data.

[65] Netzsch. *Proteus LFA Analysis Program V 6.0.0*, 2012.

[66] Corey S O'Hern, Leonardo E Silbert, Andrea J Liu, and Sidney R Nagel. Jamming at zero temperature and zero applied stress: The epitome of disorder. *Physical Review E*, 68(1):011306, 2003.

[67] M. Ostoja-Starzewski. Random field models of heterogeneous materials. *International Journal of Solids and Structures*, 35(19):2429–2455, 1998.

[68] Nobuyuki Otsu. A threshold selection method from gray-level histograms. *Automatica*, 11(285-296):23–27, 1975.

[69] W.J. Parker, R. J. Jenkins, C.P. Butler, and G.L. Abbott. Flash method of determining thermal diffusivity, heat capacity, and thermal conductivity. *Journal of Applied Physics*, 32(9):1679, 1961.

[70] K. Parlinski, Z.Q. Li, and Y. Kawazoe. First-principles determination of the soft mode in cubic ZrO_2. *Physical Review Letters*, 78(21):4063–4066, May 1997.

[71] L. M. Phinney, W. W. Erikson, and J. B. Lechman. Uncertainty quantification for multiscale thermal transport simulations. In *11th AIAA/ASME Joint Thermophysics and Heat Transfer Conference*. AIAA/ASME, 2014.

[72] H.J. Prask, C.S. Choi, N.J. Chesser, and G.J. Rosasco. Ammonium perchlorate structure and dynamics at low temperatures. *Journal of Chemical Physics*, 88(8):5106–5122, Apr 1988.

[73] Karthik Ramani and Aparna Vaidyanathan. Finite element analysis of effective thermal conductivity of filled polymeric composites. *Journal of Composite Materials*, 29(13):1725–1740, 1995.

[74] P. Reddy, K. Castelino, and A. Majumdar. Diffuse mismatch model of thermal boundary conductance using exact phonon dispersion. *Applied Physics Letters*, 87(21):–, 2005.

[75] Sidney Redner. *A guide to first-passage processes*. Cambridge University Press, 2001.

[76] Muhammad Sahimi. *Heterogeneous Materials I: Linear transport and optical properties*, volume 1. Springer, 2003.

[77] PR Schunk, PA Sackinger, and RR Rao. Goma-a full-newton finite element program for free and moving boundary problems with coupled fluid/solid momentum, energy, mass, and chemical species transport: User's guide. Technical report, Sandia National Labs., Albuquerque, NM (United States), 1996.

[78] PR Schunk, PA Sackinger, RR Rao, KS Chen, TA Baer, DA Labreche, AC Sun, MM Hopkins, SR Subia, HK Moffat, RB Secor, RA Roach, ED Wilkes, DR Noble, PL Hopkins, PK Notz, and SA Roberts. Goma 6.0 - a full-newton finite element program for free and moving boundary problems with coupled fluid/solid momentum, energy, mass, and chemical species transport: User's guide. Technical report, Sandia National Labs., Albuquerque, NM (United States), 2013.

[79] Leonardo E Silbert. Jamming of frictional spheres and random loose packing. *Soft Matter*, 6(13):2918–2924, 2010.

[80] G Spanos, DJ Rowenhorst, AC Lewis, and AB Geltmacher. Combining serial sectioning, ebsd analysis, and image-based finite element modeling. *MRS bulletin*, 33(06):597–602, 2008.

[81] M. Stammler, D. Orcutt, and P.C. Colodny. Low-temperature transitions of some ammonium salts. *Advances in X-Ray Analysis*, 6:202 – 209, 1963.

[82] R. Stedman and G. Nilsson. Dispersion relations for phonons in aluminum at 80 and 300 K. *Phys. Rev.*, 145:492–500, May 1966.

[83] E.T. Swartz and R.O. Pohl. Thermal-boundary resistance. *Reviews of Modern Physics*, 61(3):605–668, Jul 1989.

[84] A. Togo. Phonopy, 2013.

[85] A. Togo, F. Oba, and I. Tanaka. First-principles calculations of the ferroelastic transition between rutile-type and $CaCl_2$-type SiO_2 at high pressures. *Phys. Rev. B*, 78:134106, Oct 2008.

[86] Carlo Tomasi and Roberto Manduchi. Bilateral filtering for gray and color images. In *Computer Vision, 1998. Sixth International Conference on*, pages 839–846. IEEE, 1998.

[87] S Torquato. Effective electrical conductivity of two-phase disordered composite media. *Journal of Applied Physics*, 58(10):3790–3797, 1985.

[88] S Torquato and In Chan Kim. Efficient simulation technique to compute effective properties of heterogeneous media. *Applied physics letters*, 55(18):1847–1849, 1989.

[89] Salvatore Torquato. *Random heterogeneous materials: microstructure and macroscopic properties*, volume 16. Springer, 2002.

[90] K. Venkatesan. The crystal structure of ammonium perchlorate. *Proceedings of the Indian Academy of Sciences - Section A*, 46(2):134–142, 1957.

[91] Y. Wang, J. Y. Park, Y. K. Koh, and D. G. Cahill. "thermoreflectance of metal transducers for time-domain thermoreflectance. *Journal of Applied Physics*, 108:043507, 2010.

[92] E. R. Weeks and D. A. Weitz. Three-dimensional direct imaging of structural relaxation near the colloidal glass transition. *Science*, 287:627–630, 2000.

[93] E. R. Weeks and D. A. Weitz. Subdiffusion and the cage effect studied near the colloidal glass transition. *Chemical Physics*, 284:361–367, 2002.

[94] M. Xu and H. Hu. A ballistic-diffusive heat conduction model extracted from boltzmann transport equation. *Proceedings of Royal the Society A*, 467:1851–1864, 2011.

[95] J. Zhu, D. Tang, W. Wang, J. Liu, K. W. Holub, and R. Yang. Ultrafast thermoreflectance techniques for measuring thermal conductivity and interface thermal conductance of thin films. *Journal of Applied Physics*, 108:094315, 2010.

Appendix A

Table A.1. NanoFlash® Machine Parameters for Each TKP and THKP Pellet.

Pellet Label	Energetic Material	Temperature (C)	Shots	Volts (V)	Flash Duration (μs)	Preamp Gain	Main Gain	Recording Time (ms)
IP-V-1-68-1	TKP-IP (Ventron)	24.58 ± 0.26	5	270	250	10	2520	4920
IP-V-1-68-2	TKP-IP (Ventron)	25.16 ± 0.43	5	270	250	10	2520	4920
IP-V-1-68-3	TKP-IP (Ventron)	25.18 ± 0.36	5	270	250	10	2520	4920
IP-V-1-71-1	TKP-IP (Ventron)	24.56 ± 0.28	5	270	250	10	2520	5376
IP-V-1-71-1	TKP-IP (Ventron)	49.92 ± 0.18	5	270	250	10	1260	5966
IP-V-1-71-1	TKP-IP (Ventron)	100.02 ± 0.18	5	270	250	10	623	5966
IP-V-1-71-1	TKP-IP (Ventron)	150.02 ± 0.18	5	270	250	10	315	7248
IP-V-1-71-1	TKP-IP (Ventron)	199.74 ± 0.42	5	270	250	10	155	8130
IP-V-1-71-1	TKP-IP (Ventron)	250.24 ± 0.30	5	270	250	10	155	8130
IP-V-1-71-2	TKP-IP (Ventron)	25.18 ± 0.36	5	270	250	10	2520	5376
IP-V-1-71-2	TKP-IP (Ventron)	49.96 ± 0.21	5	270	250	10	1260	6424
IP-V-1-71-2	TKP-IP (Ventron)	100.02 ± 0.19	5	270	250	10	623	6424
IP-V-1-71-2	TKP-IP (Ventron)	150.02 ± 0.19	5	270	250	10	315	6424
IP-V-1-71-2	TKP-IP (Ventron)	200.26 ± 0.51	5	270	250	10	155	8130
IP-V-1-71-2	TKP-IP (Ventron)	250.14 ± 0.32	5	270	250	10	78.8	8130
IP-V-1-71-3	TKP-IP (Ventron)	25.20 ± 0.64	5	270	250	10	2520	5376
IP-V-1-76-1	TKP-IP (Ventron)	25.38 ± 0.19	5	270	250	10	2520	4452
IP-V-1-76-2	TKP-IP (Ventron)	24.82 ± 0.88	5	270	250	10	2520	4452
IP-V-1-76-3	TKP-IP (Ventron)	24.82 ± 0.69	5	270	250	10	2520	4452
IP-V-1-79-1	TKP-IP (Ventron)	25.04 ± 0.57	5	270	250	10	2520	5186
IP-V-1-79-2	TKP-IP (Ventron)	24.84 ± 0.80	5	270	250	10	2520	5186
IP-V-1-79-3	TKP-IP (Ventron)	25.26 ± 0.28	5	270	250	10	2520	4668
IP-A-1-71-1	TKP-IP (ATK)	24.76 ± 0.35	7	270	250	10	2520	6048
IP-A-3-71-1	TKP-IP (ATK)	24.90 ± 0.30	5	292	450	10	5002	55672
IP-A-3-71-2	TKP-IP (ATK)	25.12 ± 0.36	5	292	450	10	5002	55672
IP-A-3-71-3	TKP-IP (ATK)	25.08 ± 1.30	5	292	450	10	5002	55672
OP-1-80-1	TKP-OP	25.08 ± 0.48	5	270	250	10	2520	5376
OP-1-80-2	TKP-OP	25.38 ± 0.39	5	270	250	10	2520	5376
OP-1-80-3	TKP-OP	25.30 ± 0.41	5	270	250	10	2520	4892
THKP-1-80-1	THKP	24.88 ± 0.26	5	270	250	10	2520	5478
THKP-1-80-2	THKP	25.12 ± 1.37	5	270	250	10	2520	5478
THKP-1-80-3	THKP	25.14 ± 0.40	5	270	250	10	2520	5478

Table A.2. Measured Thermal Diffusivity in mm^2/s of the TKP and THKP Pellets.

Pellet Label	Temperature (C)	Shot #1	Shot #2	Shot #3	Shot #4	Shot #5	Shot #6	Shot #7
IP-V-1-68-1	24.58 ± 0.26	0.3085 ± 0.0015	0.3083 ± 0.0016	0.3060 ± 0.0015	0.3052 ± 0.0015	0.3101 ± 0.0017	-	-
IP-V-1-68-2	25.16 ± 0.43	0.3007 ± 0.0013	0.2997 ± 0.0014	0.3038 ± 0.0011	0.3009 ± 0.0014	0.3004 ± 0.0015	-	-
IP-V-1-68-3	25.18 ± 0.36	0.3058 ± 0.0016	0.3002 ± 0.0015	0.3024 ± 0.0016	0.3001 ± 0.0016	0.2989 ± 0.0015	-	-
IP-V-1-71-1	24.56 ± 0.28	0.3050 ± 0.0017	0.3043 ± 0.0018	0.3022 ± 0.0017	0.3036 ± 0.0017	0.3054 ± 0.0017	-	-
IP-V-1-71-1	49.92 ± 0.18	0.2653 ± 0.0013	0.2710 ± 0.0015	0.2692 ± 0.0014	0.2705 ± 0.0015	0.2719 ± 0.0015	-	-
IP-V-1-71-1	100.02 ± 0.18	0.2439 ± 0.0014	0.2419 ± 0.0014	0.2422 ± 0.0013	0.2409 ± 0.0013	0.2433 ± 0.0013	-	-
IP-V-1-71-1	150.02 ± 0.18	0.2121 ± 0.0011	0.2110 ± 0.0010	0.2113 ± 0.0011	0.2102 ± 0.0011	0.2113 ± 0.0011	-	-
IP-V-1-71-1	199.74 ± 0.42	0.1883 ± 0.0009	0.1886 ± 0.0009	0.1873 ± 0.0010	0.1884 ± 0.0008	0.1872 ± 0.0008	-	-
IP-V-1-71-1	250.24 ± 0.30	0.1775 ± 0.0009	0.1785 ± 0.0010	0.1796 ± 0.0009	0.1779 ± 0.0009	0.1762 ± 0.0009	-	-
IP-V-1-71-2	25.18 ± 0.36	0.2967 ± 0.0013	0.2890 ± 0.0012	0.2912 ± 0.0014	0.2912 ± 0.0014	0.2981 ± 0.0013	-	-
IP-V-1-71-2	49.96 ± 0.21	0.2610 ± 0.0010	0.2606 ± 0.0010	0.2582 ± 0.0010	0.2620 ± 0.0010	0.2594 ± 0.0011	-	-
IP-V-1-71-2	100.02 ± 0.19	0.2318 ± 0.0009	0.2331 ± 0.0010	0.2330 ± 0.0011	0.2323 ± 0.0011	0.2321 ± 0.0010	-	-
IP-V-1-71-2	150.02 ± 0.19	0.2127 ± 0.0007	0.2118 ± 0.0008	0.2132 ± 0.0008	0.2130 ± 0.0010	0.2133 ± 0.0008	-	-
IP-V-1-71-2	200.26 ± 0.51	0.1887 ± 0.0008	0.1859 ± 0.0007	0.1862 ± 0.0008	0.1855 ± 0.0008	0.1869 ± 0.0007	-	-
IP-V-1-71-2	250.14 ± 0.32	0.1761 ± 0.0007	0.1765 ± 0.0008	0.1771 ± 0.0008	0.1756 ± 0.0007	0.1778 ± 0.0007	-	-
IP-V-1-71-3	25.20 ± 0.64	0.3009 ± 0.0017	0.3029 ± 0.0017	0.3016 ± 0.0016	0.3051 ± 0.0018	0.2991 ± 0.0016	-	-
IP-V-1-76-1	25.38 ± 0.19	0.3675 ± 0.0017	0.3740 ± 0.0018	0.3801 ± 0.0019	0.3803 ± 0.0019	0.3748 ± 0.0019	-	-
IP-V-1-76-2	24.82 ± 0.88	0.3749 ± 0.0020	0.3795 ± 0.0020	0.3691 ± 0.0017	0.3688 ± 0.0018	0.3721 ± 0.0019	-	-
IP-V-1-76-3	24.82 ± 0.69	0.3625 ± 0.0017	0.3664 ± 0.0019	0.3679 ± 0.0018	0.3620 ± 0.0018	0.3714 ± 0.0019	-	-
IP-V-1-79-1	25.04 ± 0.57	0.4281 ± 0.0019	0.4304 ± 0.0019	0.4306 ± 0.0015	0.4351 ± 0.0020	0.4319 ± 0.0019	-	-
IP-V-1-79-2	24.84 ± 0.80	0.4426 ± 0.0020	0.4449 ± 0.0021	0.4523 ± 0.0021	0.4532 ± 0.0023	0.4541 ± 0.0021	-	-
IP-V-1-79-3	25.26 ± 0.28	0.4552 ± 0.0026	0.4443 ± 0.0024	0.4468 ± 0.0025	0.4480 ± 0.0027	0.4481 ± 0.0027	-	-
IP-A-1-71-1	24.76 ± 0.35	0.2430 ± 0.0013	0.2443 ± 0.0013	0.2466 ± 0.0012	0.2472 ± 0.0013	0.2459 ± 0.0014	0.2474 ± 0.0013	0.2457 ± 0.0013
IP-A-3-71-1	24.90 ± 0.30	0.2270 ± 0.0019	0.2233 ± 0.0018	0.2283 ± 0.0020	0.2188 ± 0.0019	0.2220 ± 0.0016	-	-
IP-A-3-71-2	25.12 ± 0.36	0.2178 ± 0.0021	0.2161 ± 0.0027	0.2044 ± 0.0021	0.2158 ± 0.0021	0.2215 ± 0.0019	-	-
IP-A-3-71-3	25.08 ± 1.30	0.1947 ± 0.0024	0.2055 ± 0.0019	0.2125 ± 0.0018	0.2129 ± 0.0017	0.2114 ± 0.0018	-	-
OP-1-80-1	25.08 ± 0.48	0.3032 ± 0.0014	0.3071 ± 0.0014	0.3062 ± 0.0015	0.3040 ± 0.0014	0.3044 ± 0.0015	-	-
OP-1-80-2	25.38 ± 0.39	0.3324 ± 0.0016	0.3332 ± 0.0015	0.3256 ± 0.0015	0.3233 ± 0.0016	0.3307 ± 0.0017	-	-
OP-1-80-3	25.30 ± 0.41	0.3340 ± 0.0018	0.3359 ± 0.0017	0.3413 ± 0.0020	0.3331 ± 0.0019	0.3401 ± 0.0019	-	-
THKP-1-80-1	24.88 ± 0.26	0.2980 ± 0.0013	0.3012 ± 0.0014	0.2919 ± 0.0012	0.2980 ± 0.0013	0.2927 ± 0.0012	-	-
THKP-1-80-2	25.12 ± 1.37	0.3014 ± 0.0016	0.3029 ± 0.0013	0.3034 ± 0.0016	0.3099 ± 0.0017	0.3065 ± 0.0017	-	-
THKP-1-80-3	25.14 ± 0.40	0.3156 ± 0.0014	0.3171 ± 0.0012	0.3158 ± 0.0013	0.3184 ± 0.0014	0.3125 ± 0.0013	-	-

Table A.3. Measured Specific Heat in J/gK of the TKP and THKP Pellets Found with the Pocographite Reference.

Pellet Label	Temperature (C)	Shot #1	Shot #2	Shot #3	Shot #4	Shot #5	Shot #6	Shot #7
IP-V-1-68-1	24.58 ± 0.26	0.7375 ± 0.0277	0.7316 ± 0.0278	0.7145 ± 0.0268	0.7177 ± 0.0271	0.7473 ± 0.0282	-	-
IP-V-1-68-2	25.16 ± 0.43	0.7853 ± 0.0257	0.7882 ± 0.0260	0.7915 ± 0.0254	0.7746 ± 0.0253	0.7668 ± 0.0255	-	-
IP-V-1-68-3	25.18 ± 0.36	0.7572 ± 0.0281	0.7232 ± 0.0270	0.7267 ± 0.0270	0.7273 ± 0.0274	0.7092 ± 0.0266	-	-
IP-V-1-71-1	24.56 ± 0.28	0.8672 ± 0.0421	0.8493 ± 0.0414	0.8298 ± 0.0405	0.8158 ± 0.0397	0.8558 ± 0.0414	-	-
IP-V-1-71-1	49.92 ± 0.18	0.9843 ± 0.0469	0.9928 ± 0.0477	1.0093 ± 0.0487	1.0169 ± 0.0491	0.9671 ± 0.0461	-	-
IP-V-1-71-1	100.02 ± 0.18	0.9897 ± 0.0469	0.9908 ± 0.0473	1.0176 ± 0.0481	0.9716 ± 0.0462	0.9620 ± 0.0451	-	-
IP-V-1-71-1	150.02 ± 0.18	1.0779 ± 0.0518	1.0764 ± 0.0511	1.0912 ± 0.0528	1.0948 ± 0.0532	1.1137 ± 0.0534	-	-
IP-V-1-71-1	199.74 ± 0.42	1.1515 ± 0.0554	1.1483 ± 0.0555	1.1258 ± 0.0548	1.1731 ± 0.0557	1.1045 ± 0.0530	-	-
IP-V-1-71-1	250.74 ± 0.30	1.3124 ± 0.0633	1.2720 ± 0.0616	1.2966 ± 0.0620	1.3014 ± 0.0629	1.2466 ± 0.0607	-	-
IP-V-1-71-2	25.18 ± 0.36	0.8066 ± 0.0246	0.7672 ± 0.0238	0.7512 ± 0.0231	0.7561 ± 0.0234	0.7740 ± 0.0237	-	-
IP-V-1-71-2	49.96 ± 0.21	0.8219 ± 0.0238	0.8022 ± 0.0231	0.7614 ± 0.0223	0.8011 ± 0.0229	0.8071 ± 0.0238	-	-
IP-V-1-71-2	100.02 ± 0.19	0.8885 ± 0.0260	0.9158 ± 0.0270	0.8971 ± 0.0265	0.8989 ± 0.0266	0.9034 ± 0.0266	-	-
IP-V-1-71-2	150.02 ± 0.19	1.0208 ± 0.0293	1.0416 ± 0.0304	1.0130 ± 0.0297	0.9921 ± 0.0296	1.0286 ± 0.0300	-	-
IP-V-1-71-2	200.26 ± 0.51	1.0364 ± 0.0307	1.0515 ± 0.0309	1.0325 ± 0.0307	1.0322 ± 0.0310	1.0288 ± 0.0301	-	-
IP-V-1-71-2	250.14 ± 0.32	1.1417 ± 0.0337	1.1209 ± 0.0335	1.1628 ± 0.0346	1.1314 ± 0.0337	1.1403 ± 0.0335	-	-
IP-V-1-71-3	25.20 ± 0.64	0.8368 ± 0.0412	0.8178 ± 0.0401	0.8114 ± 0.0395	0.8442 ± 0.0414	0.8023 ± 0.0395	-	-
IP-V-1-76-1	25.38 ± 0.19	0.7278 ± 0.0285	0.7324 ± 0.0281	0.7645 ± 0.0293	0.7612 ± 0.0292	0.7491 ± 0.0290	-	-
IP-V-1-76-2	24.82 ± 0.88	0.7570 ± 0.0281	0.7785 ± 0.0282	0.7409 ± 0.0269	0.7437 ± 0.0271	0.7407 ± 0.0271	-	-
IP-V-1-76-3	24.82 ± 0.69	0.7400 ± 0.0271	0.7595 ± 0.0281	0.7311 ± 0.0265	0.7211 ± 0.0266	0.7363 ± 0.0269	-	-
IP-V-1-79-1	25.04 ± 0.57	0.7971 ± 0.0241	0.7715 ± 0.0230	0.7773 ± 0.0230	0.8166 ± 0.0248	0.7921 ± 0.0238	-	-
IP-V-1-79-2	24.84 ± 0.80	0.7856 ± 0.0292	0.7878 ± 0.0294	0.7784 ± 0.0286	0.7748 ± 0.0287	0.7701 ± 0.0282	-	-
IP-V-1-79-3	25.26 ± 0.28	0.7444 ± 0.0375	0.7327 ± 0.0374	0.7366 ± 0.0377	0.7446 ± 0.0382	0.7380 ± 0.0377	-	-
IP-A-1-71-1	24.76 ± 0.35	0.7092 ± 0.0314	0.7357 ± 0.0322	0.7452 ± 0.0321	0.7529 ± 0.0327	0.7513 ± 0.0332	0.7438 ± 0.0324	0.7390 ± 0.0321
IP-A-3-71-1	24.90 ± 0.30	0.9546 ± 0.0669	0.9218 ± 0.0622	0.8786 ± 0.0629	0.8165 ± 0.0579	0.8307 ± 0.0538	-	-
IP-A-3-71-2	25.12 ± 0.36	1.0292 ± 0.0729	1.0721 ± 0.0949	0.9402 ± 0.0758	1.0087 ± 0.0724	0.9238 ± 0.0592	-	-
IP-A-3-71-3	25.08 ± 1.30	0.8748 ± 0.3713	0.9950 ± 0.0719	0.9716 ± 0.0621	0.8474 ± 0.0512	0.8542 ± 0.0550	-	-
OP-1-80-1	25.08 ± 0.48	0.6583 ± 0.0243	0.6613 ± 0.0242	0.6513 ± 0.0239	0.6533 ± 0.0241	0.6407 ± 0.0239	-	-
OP-1-80-2	25.38 ± 0.39	0.6554 ± 0.0258	0.6537 ± 0.0254	0.6264 ± 0.0249	0.6327 ± 0.0253	0.6544 ± 0.0257	-	-
OP-1-80-3	25.30 ± 0.41	0.6499 ± 0.0350	0.6419 ± 0.0347	0.6648 ± 0.0356	0.6335 ± 0.0345	0.6591 ± 0.0353	-	-
THKP-1-80-1	24.88 ± 0.26	0.7229 ± 0.0232	0.7222 ± 0.0230	0.6999 ± 0.0224	0.7244 ± 0.0233	0.6904 ± 0.0220	-	-
THKP-1-80-1	25.12 ± 1.37	0.7050 ± 0.0336	0.7161 ± 0.0338	0.7212 ± 0.0343	0.7472 ± 0.0349	0.7477 ± 0.0353	-	-
THKP-1-80-1	25.14 ± 0.40	0.7627 ± 0.0220	0.7734 ± 0.0218	0.7964 ± 0.0228	0.7691 ± 0.0219	0.7358 ± 0.0210	-	-

Table A.4. Measured Specific Heat in J/gK of the TKP and THKP Pellets Found with the Pyroceram® Reference.

Pellet Label	Temperature (C)	Shot #1	Shot #2	Shot #3	Shot #4	Shot #5	Shot #6	Shot #7
IP-V-1-68-1	24.58 ± 0.26	0.6031 ± 0.0256	0.5982 ± 0.0256	0.5842 ± 0.0248	0.5869 ± 0.0250	0.6110 ± 0.0260	-	-
IP-V-1-68-2	25.16 ± 0.43	0.6421 ± 0.0245	0.6445 ± 0.0247	0.6472 ± 0.0243	0.6333 ± 0.0242	0.6270 ± 0.0242	-	-
IP-V-1-68-3	25.18 ± 0.36	0.6192 ± 0.0239	0.5913 ± 0.0229	0.5942 ± 0.0229	0.5947 ± 0.0231	0.5798 ± 0.0225	-	-
IP-V-1-71-1	24.56 ± 0.28	0.7091 ± 0.0372	0.6945 ± 0.0365	0.6785 ± 0.0357	0.6671 ± 0.0350	0.6998 ± 0.0365	-	-
IP-V-1-71-1	49.92 ± 0.18	0.7822 ± 0.0389	0.7889 ± 0.0395	0.8021 ± 0.0404	0.8081 ± 0.0407	0.7685 ± 0.0383	-	-
IP-V-1-71-1	100.02 ± 0.18	0.7587 ± 0.0366	0.7596 ± 0.0369	0.7801 ± 0.0375	0.7448 ± 0.0361	0.7375 ± 0.0352	-	-
IP-V-1-71-1	150.02 ± 0.18	0.7900 ± 0.0382	0.7888 ± 0.0377	0.7997 ± 0.0390	0.8023 ± 0.0393	0.8161 ± 0.0394	-	-
IP-V-1-71-1	199.74 ± 0.42	0.8237 ± 0.0399	0.8214 ± 0.0400	0.8053 ± 0.0395	0.8391 ± 0.0402	0.7901 ± 0.0382	-	-
IP-V-1-71-1	250.74 ± 0.30	0.9410 ± 0.0456	0.9120 ± 0.0444	0.9296 ± 0.0447	0.9331 ± 0.0453	0.8938 ± 0.0437	-	-
IP-V-1-71-2	25.18 ± 0.36	0.6595 ± 0.0239	0.6273 ± 0.0230	0.6142 ± 0.0224	0.6182 ± 0.0226	0.6329 ± 0.0230	-	-
IP-V-1-71-2	49.96 ± 0.21	0.6529 ± 0.0211	0.6372 ± 0.0205	0.6048 ± 0.0197	0.6363 ± 0.0204	0.6411 ± 0.0210	-	-
IP-V-1-71-2	100.02 ± 0.19	0.6808 ± 0.0208	0.7017 ± 0.0217	0.6874 ± 0.0212	0.6888 ± 0.0213	0.6922 ± 0.0213	-	-
IP-V-1-71-2	150.02 ± 0.19	0.7477 ± 0.0217	0.7630 ± 0.0225	0.7420 ± 0.0220	0.7267 ± 0.0220	0.7535 ± 0.0223	-	-
IP-V-1-71-2	200.26 ± 0.51	0.7421 ± 0.0224	0.7529 ± 0.0225	0.7393 ± 0.0224	0.7391 ± 0.0226	0.7366 ± 0.0220	-	-
IP-V-1-71-2	250.14 ± 0.32	0.8186 ± 0.0244	0.8037 ± 0.0243	0.8338 ± 0.0251	0.8112 ± 0.0245	0.8176 ± 0.0243	-	-
IP-V-1-71-3	25.20 ± 0.64	0.6842 ± 0.0363	0.6687 ± 0.0353	0.6635 ± 0.0348	0.6903 ± 0.0365	0.6560 ± 0.0348	-	-
IP-V-1-76-1	25.38 ± 0.19	0.5951 ± 0.0265	0.5989 ± 0.0263	0.6251 ± 0.0274	0.6224 ± 0.0273	0.6125 ± 0.0270	-	-
IP-V-1-76-2	24.82 ± 0.88	0.6190 ± 0.0265	0.6366 ± 0.0267	0.6058 ± 0.0255	0.6081 ± 0.0257	0.6056 ± 0.0256	-	-
IP-V-1-76-3	25.26 ± 0.28	0.6051 ± 0.0256	0.6211 ± 0.0264	0.5978 ± 0.0250	0.5896 ± 0.0251	0.6021 ± 0.0254	-	-
IP-V-1-79-1	25.04 ± 0.57	0.6518 ± 0.0237	0.6308 ± 0.0227	0.6356 ± 0.0228	0.6677 ± 0.0243	0.6477 ± 0.0234	-	-
IP-V-1-79-2	24.84 ± 0.80	0.6424 ± 0.0274	0.6441 ± 0.0276	0.6465 ± 0.0270	0.6335 ± 0.0270	0.6297 ± 0.0266	-	-
IP-V-1-79-3	25.26 ± 0.28	0.6087 ± 0.0322	0.5991 ± 0.0328	0.6023 ± 0.0330	0.6088 ± 0.0334	0.5984 ± 0.0330	-	-
IP-A-1-71-1	24.76 ± 0.35	0.5799 ± 0.0281	0.6015 ± 0.0289	0.6093 ± 0.0288	0.6156 ± 0.0293	0.6143 ± 0.0297	0.6082 ± 0.0290	0.6042 ± 0.0288
IP-A-3-71-1	24.90 ± 0.30	0.8127 ± 0.0584	0.7848 ± 0.0543	0.7480 ± 0.0548	0.6951 ± 0.0505	0.7072 ± 0.0471	-	-
IP-A-3-71-2	25.12 ± 0.36	0.8763 ± 0.0636	0.9128 ± 0.0820	0.8004 ± 0.0657	0.8588 ± 0.0631	0.7866 ± 0.0519	-	-
IP-A-3-71-3	25.08 ± 1.30	0.7448 ± 0.3164	0.8471 ± 0.0627	0.8272 ± 0.0544	0.7215 ± 0.0450	0.7273 ± 0.0482	-	-
OP-1-80-1	25.08 ± 0.48	0.5383 ± 0.0225	0.5407 ± 0.0225	0.5326 ± 0.0222	0.5341 ± 0.0223	0.5239 ± 0.0221	-	-
OP-1-80-2	25.38 ± 0.39	0.5359 ± 0.0235	0.5345 ± 0.0233	0.5122 ± 0.0227	0.5173 ± 0.0231	0.5351 ± 0.0235	-	-
OP-1-80-3	25.30 ± 0.41	0.5314 ± 0.0304	0.5248 ± 0.0302	0.5436 ± 0.0310	0.5180 ± 0.0300	0.5389 ± 0.0308	-	-
THKP-1-80-1	24.88 ± 0.26	0.5911 ± 0.0222	0.5905 ± 0.0221	0.5722 ± 0.0215	0.5923 ± 0.0223	0.5646 ± 0.0211	-	-
THKP-1-80-2	25.12 ± 1.37	0.5765 ± 0.0297	0.5855 ± 0.0299	0.5897 ± 0.0304	0.6110 ± 0.0309	0.6114 ± 0.0313	-	-
THKP-1-80-3	25.14 ± 0.40	0.6236 ± 0.0217	0.6324 ± 0.0217	0.6511 ± 0.0226	0.6289 ± 0.0218	0.6016 ± 0.0208	-	-

Table A.5. Comparisons of the Thermal Diffusivity in mm^2/s Found with Each Analysis Program for Each TKP and THKP Formulation.

Pellet Label	Energetic Material	MATLAB® Thermal Diffusivity	Proteus® Thermal Diffusivity	Percentage Difference
IP-V-1-68-1	TKP-IP (Ventron)	0.3076 ± 0.0024	0.2988 ± 0.0013	-2.95
IP-V-1-68-2	TKP-IP (Ventron)	0.3011 ± 0.0020	0.2888 ± 0.0015	-4.26
IP-V-1-68-3	TKP-IP (Ventron)	0.3015 ± 0.0031	0.2934 ± 0.0008	-2.75
IP-V-1-71-1	TKP-IP (Ventron)	0.3041 ± 0.0019	0.2964 ± 0.0016	-2.60
IP-V-1-71-2	TKP-IP (Ventron)	0.2932 ± 0.0040	0.2854 ± 0.0014	-2.75
IP-V-1-71-3	TKP-IP (Ventron)	0.3019 ± 0.0027	0.2964 ± 0.0016	-1.86
IP-V-1-76-1	TKP-IP (Ventron)	0.3753 ± 0.0054	0.3658 ± 0.0012	-2.61
IP-V-1-76-2	TKP-IP (Ventron)	0.3729 ± 0.0047	0.3624 ± 0.0020	-2.90
IP-V-1-76-3	TKP-IP (Ventron)	0.3660 ± 0.0042	0.3652 ± 0.0030	-0.23
IP-V-1-79-1	TKP-IP (Ventron)	0.4312 ± 0.0031	0.4212 ± 0.0023	-2.38
IP-V-1-79-2	TKP-IP (Ventron)	0.4494 ± 0.0056	0.4378 ± 0.0024	-2.65
IP-V-1-79-3	TKP-IP (Ventron)	0.4485 ± 0.0047	0.4408 ± 0.0023	-1.74
IP-A-1-71-1	TKP-IP (ATK) 1mm	0.2457 ± 0.0019	0.2420 ± 0.0009	-1.54
IP-A-3-71-1	TKP-IP (ATK) 3mm	0.2239 ± 0.0042	0.2248 ± 0.0026	0.41
IP-A-3-71-2	TKP-IP (ATK) 3mm	0.2151 ± 0.0066	0.2076 ± 0.0047	-3.63
IP-A-3-71-3	TKP-IP (ATK) 3mm	0.2074 ± 0.0113	0.2036 ± 0.0089	-1.86
OP-1-80-1	TKP-OP	0.3050 ± 0.0021	0.2964 ± 0.0014	-2.90
OP-1-80-2	TKP-OP	0.3290 ± 0.0045	0.3228 ± 0.0015	-1.93
OP-1-80-3	TKP-OP	0.3369 ± 0.0040	0.3314 ± 0.0018	-1.65
THKP-1-80-1	THKP	0.2964 ± 0.0040	0.2926 ± 0.0019	-1.29
THKP-1-80-2	THKP	0.3048 ± 0.0037	0.3042 ± 0.0018	-0.20
THKP-1-80-3	THKP	0.3159 ± 0.0025	0.3062 ± 0.0012	-3.16

Table A.6. Comparisons of the Specific Heat in J/gK Found with Each Analysis Program for Each TKP and THKP Formulation Using the Pocographite Reference.

Pellet Label	Energetic Material	MATLAB® Specific Heat	Proteus® Specific Heat	Percentage Difference
IP-V-1-68-1	TKP-IP (Ventron)	0.7297 ± 0.0243	0.7364 ± 0.0206	0.91
IP-V-1-68-2	TKP-IP (Ventron)	0.7813 ± 0.0205	0.7718 ± 0.0206	-1.23
IP-V-1-68-3	TKP-IP (Ventron)	0.7287 ± 0.0276	0.7362 ± 0.0177	1.02
IP-V-1-71-1	TKP-IP (Ventron)	0.8436 ± 0.0364	0.8540 ± 0.0354	1.22
IP-V-1-71-2	TKP-IP (Ventron)	0.7710 ± 0.0297	0.7804 ± 0.0371	1.21
IP-V-1-71-3	TKP-IP (Ventron)	0.8225 ± 0.0334	0.8454 ± 0.0346	2.71
IP-V-1-76-1	TKP-IP (Ventron)	0.7470 ± 0.0274	0.7586 ± 0.0130	1.53
IP-V-1-76-2	TKP-IP (Ventron)	0.7521 ± 0.0265	0.7610 ± 0.0190	1.16
IP-V-1-76-3	TKP-IP (Ventron)	0.7376 ± 0.0245	0.7520 ± 0.0285	1.91
IP-V-1-79-1	TKP-IP (Ventron)	0.7909 ± 0.0262	0.8066 ± 0.0375	1.94
IP-V-1-79-2	TKP-IP (Ventron)	0.7793 ± 0.0194	0.7922 ± 0.0379	1.63
IP-V-1-79-3	TKP-IP (Ventron)	0.7380 ± 0.0223	0.7602 ± 0.0127	2.91
IP-A-1-71-1	TKP-IP (ATK) 1mm	0.7388 ± 0.0302	0.7606 ± 0.0214	2.86
IP-A-3-71-1	TKP-IP (ATK) 3mm	0.8804 ± 0.0787	0.8500 ± 0.1087	-3.58
IP-A-3-71-2	TKP-IP (ATK) 3mm	0.9948 ± 0.0883	0.8774 ± 0.0884	-13.38
IP-A-3-71-3	TKP-IP (ATK) 3mm	0.9086 ± 0.1390	0.8256 ± 0.1194	-10.05
OP-1-80-1	TKP-OP	0.6530 ± 0.0177	0.6683 ± 0.0146	1.63
OP-1-80-2	TKP-OP	0.6445 ± 0.0235	0.6612 ± 0.0120	2.52
OP-1-80-3	TKP-OP	0.6498 ± 0.0268	0.6690 ± 0.0180	2.87
THKP-1-80-1	THKP	0.7120 ± 0.0240	0.7380 ± 0.0212	3.53
THKP-1-80-2	THKP	0.7274 ± 0.0322	0.7666 ± 0.0233	5.11
THKP-1-80-3	THKP	0.7675 ± 0.0289	0.7736 ± 0.0301	0.79

Table A.7. Comparisons of the Specific Heat in J/gK Found with Each Analysis Program for Each TKP and THKP Formulation Using the Pyroceram® Reference.

Pellet Label	Energetic Material	MATLAB® Specific Heat	Proteus® Specific Heat	Percentage Difference
IP-V-1-68-1	TKP-IP (Ventron)	0.5967 ± 0.0211	0.5926 ± 0.0168	-0.69
IP-V-1-68-2	TKP-IP (Ventron)	0.6388 ± 0.0183	0.6210 ± 0.0164	-2.87
IP-V-1-68-3	TKP-IP (Ventron)	0.5958 ± 0.0229	0.5922 ± 0.0141	-0.61
IP-V-1-71-1	TKP-IP (Ventron)	0.6898 ± 0.0310	0.6874 ± 0.0282	-0.34
IP-V-1-71-2	TKP-IP (Ventron)	0.6304 ± 0.0259	0.6276 ± 0.0301	-0.45
IP-V-1-71-3	TKP-IP (Ventron)	0.6725 ± 0.0285	0.6780 ± 0.0274	-0.81
IP-V-1-76-1	TKP-IP (Ventron)	0.6108 ± 0.0239	0.6100 ± 0.0101	-0.13
IP-V-1-76-2	TKP-IP (Ventron)	0.6150 ± 0.0232	0.6126 ± 0.0150	-0.39
IP-V-1-76-3	TKP-IP (Ventron)	0.6031 ± 0.0216	0.6050 ± 0.0230	0.31
IP-V-1-79-1	TKP-IP (Ventron)	0.6467 ± 0.0232	0.6488 ± 0.0301	0.32
IP-V-1-79-2	TKP-IP (Ventron)	0.6372 ± 0.0174	0.6374 ± 0.0302	0.03
IP-V-1-79-3	TKP-IP (Ventron)	0.6035 ± 0.0191	0.6116 ± 0.0110	1.33
IP-A-1-71-1	TKP-IP (ATK) 1mm	0.6041 ± 0.0258	0.6120 ± 0.0168	1.29
IP-A-3-71-1	TKP-IP (ATK) 3mm	0.7496 ± 0.0676	0.7210 ± 0.0911	-3.97
IP-A-3-71-2	TKP-IP (ATK) 3mm	0.8470 ± 0.0758	0.7446 ± 0.0752	-13.75
IP-A-3-71-4	TKP-IP (ATK) 3mm	0.7736 ± 0.1185	0.7006 ± 0.1019	-10.42
OP-1-80-1	TKP-OP	0.5339 ± 0.0157	0.5326 ± 0.0138	-0.25
OP-1-80-2	TKP-OP	0.5270 ± 0.0203	0.5320 ± 0.0092	0.94
OP-1-80-3	TKP-OP	0.5313 ± 0.0227	0.5382 ± 0.0148	1.27
THKP-1-80-1	THKP	0.5821 ± 0.0210	0.5936 ± 0.0167	1.93
THKP-1-80-2	THKP	0.5948 ± 0.0274	0.6168 ± 0.0189	3.57
THKP-1-80-3	THKP	0.6275 ± 0.0253	0.6226 ± 0.0238	-0.79

Appendix B

Verification of Random Walk Algorithm

As discussed in Section 6, the current implementation of the random walk algorithm is sensitive to values of Δx_i. To verify the convergence of our simulations, we plot the mean squared displacement as well as the scaling coefficient α for decreasing values of Δx_i in Figure B.1. For the two smallest pressures tested (p = 4e-6 and p = 4e-7), we obtain adequate convergence for $\Delta x_i = 0.0005$ and 0.0002, respectively. For higher pressures, convergence is readily achieved with even larger values of Δx_i (data not shown). The data discussed so far have been based on simulations that used a Δx_i value of 0.001 for $p \geq 0.0008$; $\Delta x_i = 0.0005$ for 4e-6 $\leq p <$ 0.0008; and $\Delta x_i = 0.0002$ for p = 4e-7.

In order to verify that finite size effects of the jammed particle packs are not significant, we plot the MSD and scaling coefficient α for several jammed configurations that contain approximately 10,000 particles (10× more than the systems discussed so far). As seen from Figure B.2, there are no effects on diffusion characteristics due to system size.

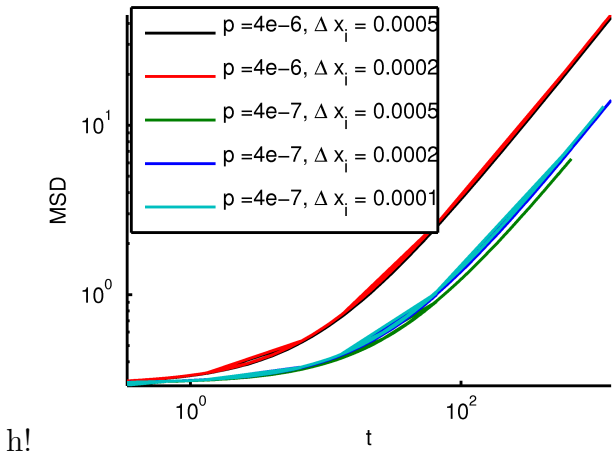

h!

(a) Mean squared displacement.

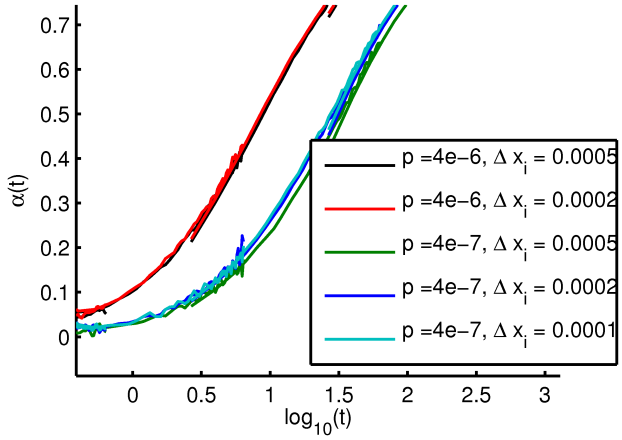

(b) Scaling exponent α (MSD $\sim t^{\alpha}$)

Figure B.1. Convergence of simulation results as a function of Δx_i. Both plots are magnified to show relevant regions.

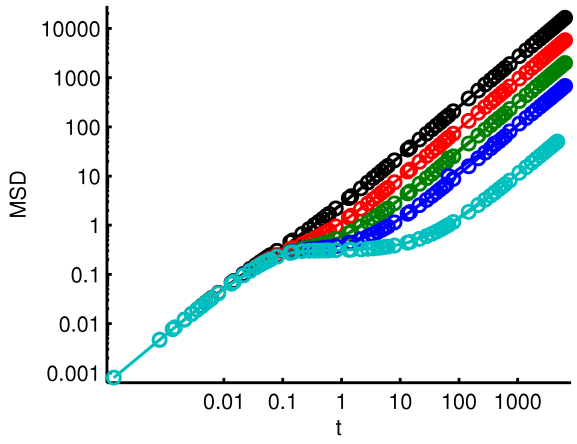

h!

(a) Mean squared displacement.

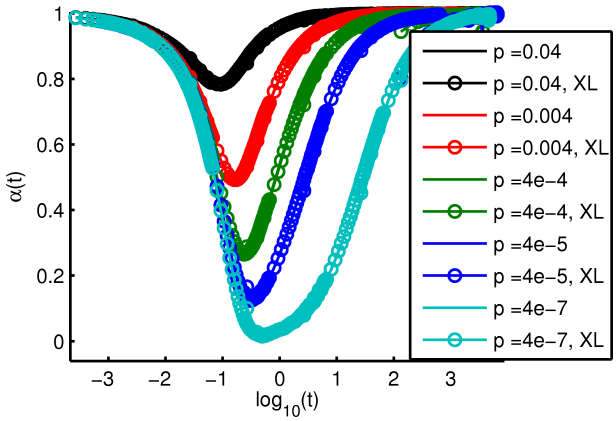

(b) Scaling exponent α (MSD $\sim t^{\alpha}$)

Figure B.2. Effects of system size on MSD(t) and $\alpha(t)$ at several pressures. The legend entries labelled 'XL' correspond to the systems containing ten times more particles than the systems discussed so far.

DISTRIBUTION:

1	MS 0899	Technical Library, 9536 (electronic copy)
1	MS 0359	D. Chavez, LDRD Office, 1911

Sandia National Laboratories